ЕЛЕКТРОНИКА (ELECTRONICS)

***

Publisher

Faculty of Electrical Engineering
University of Banja Luka
Patre 5, 78000 Banja Luka
Bosnia and Herzegovina

Phone: +387 51 211-820
Fax: +387 51 211-408
Email: info@etf.unibl.org
Web: www.etf.unibl.org

Publication frequency: Two issues a year
ISSN: 1450-5843 (Print), 2831-0128 (Online)
UDC: 621.38
Number of printed copies: 50

ELECTRONICS, VOL. 30, NO. 1, JUNE 2026

Editor's Column

Mladen Knezic

Everything we hear is an opinion, not a fact.
Everything we see is a perspective, not the truth.

Marcus Aurelius, Meditations

Editorial Letter
DOI: 10.53314/ELS2630001K

THE first issue of Vol. 30 of the Electronics journal presents five original research papers that highlight the intersection of advanced computational frameworks and specialized hardware design. These contributions address critical needs in medical diagnostics, high-speed communication, and energy-efficient semiconductor technology.

The issue begins with a study by Al-Hasooni et al., who propose a multimodal deep learning framework for the near-instantaneous prediction of cardiovascular events. By simultaneously processing 12-lead ECG waveforms through a specialized SignalCNN and patient demographic data via MetaMLP, the authors achieve a validation accuracy of 85.19%. This hybrid approach demonstrates immediate clinical potential, as the system can deliver diagnostic insights in less than 0.25 seconds, offering a scalable solution for real-time cardiac monitoring.

In the field of biomedical sensing, Mezache et al. introduce a novel multi-band metamaterial resonator designed for the terahertz (THz) regime. Specifically tailored for the detection of SARS-CoV-2, the biosensor utilizes a thin gold layer to achieve a high sensitivity of 347.7 GHz/RIU. The design's ability to differentiate between various virus types through refractive index changes—combined with its non-destructive nature—establishes a robust foundation for next-generation label-free diagnostic platforms.

Shifting focus to semiconductor architecture, Goswami et al. investigate FinFET-based sub-circuit designs for low-power VLSI applications. Their research introduces innovative stacked-based 4:3 and 5:3 compressors for multipliers, which significantly reduce the critical path delay and power consumption. Simulations indicate a 64.91% reduction in delay and an 87.85% improvement in average power, proving that FinFET technology is essential for maintaining performance as device scaling progresses beyond the limits of traditional planar transistors.

The final two papers address advances in antenna engineering. Bin Helal and Touhidul Islam present a compact ultra-wideband (UWB) pi-slotted elliptical patch antenna for THz-band 6G wireless communication. This design, which incorporates a pi-shaped slot for the first time in the THz spectral region, achieves a wide impedance bandwidth of 3.41 THz and a high gain of 7.906 dB. Its ultra-compact footprint makes it an ideal candidate for on-chip 6G systems and high-speed sensing.

Lastly, Md. Samiul Islam and Abu Zafor Md. Touhidul Islam contribute a polyester-based textile antenna specifically for smart clothing. Operating in the 3.5 GHz band, the antenna is optimized for 5G NR and WiMAX applications while maintaining a high radiation efficiency of 94.52%. Extensive bending and SAR analysis confirm that the design is both robust and compliant with IEEE safety standards, making it a practical and safe solution for wearable healthcare and broadband communication.

Finally, we must also note with sadness that we close this issue with an *In Memoriam* letter written by our honorary Editor-in-Chief Prof. Branko Dokić for Prof. Milić Stojić, who passed away at the beginning of the year. His work has left an invaluable mark on our community, and we use this opportunity to honor his legacy and profound contributions to the field.

We hope that the readers find these articles both intellectually stimulating and practically relevant to their ongoing research. As always, I thank the authors for their contributions to this issue of the journal and extend great appreciation to all the reviewers who participated in the editorial process by providing their reports in a timely manner to the editors and authors.

Near-instantaneous Cardiovascular Event Prediction Using Multimodal Deep Learning

Maytham Kareem Naeem Al-Hasooni, Amenah Y. Abdzaid, Noor. H Hadi, and Hassan Falah Fakhruldeen

Abstract*—This study introduces a new perspective into deep learning in the light of a multimodal approach: cardiovascular events can be predicted, using real-time data of physiological signals in collaboration with metadata related to the patient. Electronic Health Records (EHR) are digital versions of patients' medical histories, while Multilayer Perceptron (MLP) and Convolutional Neural Network (CNN) are deep learning architectures designed for processing structured data and spatial/temporal patterns, respectively. A hybrid neural network model is designed that allows taking, as input from the CNN, the 12-lead ECG signals, while an MLP processes patient demographic and clinical features. It is designed to simultaneously process temporal ECG patterns and static patient characteristics for all-rounded cardiovascular risk assessment. In this work, our dataset consisted of 17,441 ECG recordings per patient, each being a 12-channel signal sampled on 500-time points and patient metadata like age, sex, and weight. Our architecture has two specialised components: the proposed SignalCNN to process the waveforms including two convolutional layers with batch normalization and dropout as regularization and MetaMLP processing patient metadata. These combined features are then fed into a classifier to enable multi-label prediction of five common cardiovascular conditions. The model yielded very promising results and performed very robustly with an overall validation accuracy of 85.19% after 15 epochs of training. The training was improving smoothly for both training and validation metrics, while the validation loss decreased from 0.4298 to 0.3484, which is indicative of good generalization. The model was very stable in its training without showing any hint of overfitting thanks to strategic dropout and batch normalization. This work will contribute to cardiovascular healthcare with a real-time, automated system that can be used for the early detection of cardiac events. The approach is multimodal, offering more nuanced predictions by including instantaneous physiological signals, together with patient-specific factors. This may enable earlier and more accurate clinical assessment of cardiovascular risk.

Manuscript received on December 28th, 2024. Received in revised form on February 14th and June 11th, 2025. Accepted for publication on September 16th, 2025.

Maytham Kareem Naeem Al-Hasooni, Department of Computer Science, College of Computer Science and Mathematics, University of Kufa, Najaf, Iraq (email: maythamk.alhasooni@uokufa.edu.iq, ORCiD: 0009-0001-9921-4425).

Amenah Y. Abdzaid, Fatima Al Zahra School for Distinguish Students, AL-Diwaniyah Education Directorate, Iraq (email: amanahyahaya98@gmail.com, ORCiD: 0009-0003-6267-4414).

Noor. H Hadi, Artificial Intelligence Department, College of Engineering and Technologies, Al-Mustaqbal University, Hillah, Iraq (email: noor.hasan.hida@uomus.edu.iq, ORCiD: 0009-0006-4943-0804).

Hassan Falah Fakhruldeen, Computer Techniques Engineering Department, Faculty of Information Technology, Imam Ja'afar Al-Sadiq University, Baghdad, Iraq (email: hassan.fakhruldeen@gmail.com, ORCiD: 0000-0001-9104-847X).

***Index Terms* — Cardiovascular Disease, ECG Analysis, Medical Diagnostics, Neural Networks, Healthcare Informatics.**

Original Research Paper
DOI: 10.53314/ELS2630003A

I. Introduction

CARDIOVASCULAR diseases (CVDs) remain one of the leading causes of death worldwide; thus, early detection and advanced risk assessment methods are increasingly needed. Traditional cardiovascular diagnosis is based essentially on expert interpretation of ECG signals, [1] which might be time-consuming and subject to inter-observer variability. The recent development of deep learning technologies opens new perspectives in automatic real-time analysis of cardiovascular signals, possibly revolutionizing the way we perform cardiac diagnostics and monitoring.

In recent years, advances in deep learning architectures which include signal processing and multimodal analysis appear to have a promising future in medical diagnostics [2]. Concurrently, increases in both the quality and accessibility of physiologic data provide a conduit to more advanced modelling for the prediction of cardiovascular events [3]. Although available techniques have been promising for the analysis of ECG data, they still disregard other patient-related information that may be associated with cardiovascular risk and constrict the analysis to only focusing on electrical activity of the heart [4].

The present work addresses this limitation by introducing a novel multimodal deep-learning framework that simultaneously processes ECG signals and patient information [5]. The proposed architecture combines digitize patient heart history, which is Electronic Health Records (EHR), Multilayer Perceptron (MLP) responsible for processing the structured data and Convolutional Neural Networks (CNN) focusing on timing data/temporal pattern detection and spatial information based on electrocardiography recording [6].

This holistic analysis makes it therefore possible to perform a more comprehensive of cardiovascular risks factors, which takes into account both the temporal dynamics of ECG signals and patient's static features [7]. This is what makes this work important as the study finding has immediate clinical application. Our system is able to analyze multiple modalities of data at the same time, enabling fast and automated assessments with high accuracy, especially in urgent situations where prompt diagnosis determines mostly the patient's management [8]. Moreover, our method is addressing the increasing need for healthcare providers to scale up and automate, potentially relieving some burden on healthcare personnel without sacrificing diagnostic performance at high level [9].

It is an extension of previous research therein and in relation to the spectrum of cardiovascular diagnostics and deep learning in that we introduce novelty with architectural design and multimodal data fusion. Our proposed model has the potential to exploit traditional clinical risk factors together with deep leaning state-of-the-art novel risk markers for early detection and diagnosis of CVD events by improving patients' outcomes, leading to earlier intervention or enhancing accuracy in risk prediction.

Key Definitions:

Electronic Health Records (EHR): Digital repositories of patient health information.

Multilayer Perceptron (MLP): A class of feedforward artificial neural networks for non-linear data modeling.

Convolutional Neural Network (CNN): A deep learning model specialized for grid-like data (e.g., ECG signals).

II. Literature review

Wu [10] reviewed existing deep learning methods for CVD prediction, noting that CNNs and RNNs achieved an average accuracy of 82.3% on ECG datasets. However, their work did not propose a novel method or use the PTB-XL dataset.

Yuanlong Wang and Changchang Yin [11] introduce a review on integrating multi-modal data from EHR to improve clinical risk prediction. The EHR data can take various forms, such as temporal variables, medical images, or clinical notes; all are heterogeneous data and, hence challenging. On the other hand, this makes the range of views on patient health wider. This work proposes an early, joint, and late fusion framework to combine those modalities for tasks like in-hospital mortality, long length of stay, and 30-day readmission. Experiments are conducted that show results indicating the superiority of multi-modal models over unimodal models and that temporal variables are more contributive than medical images or clinical notes.

S. V. Evangelin Sonia and R. Nedunchezhian [12] propose a new deep learning-based approach, namely DNHRV, to classify cardiovascular diseases of diabetic men using heart rate variability data. Heart rate variability is a noninvasive method which demonstrates the impact of the autonomic nervous system on heart function and aids in detecting disorders of the heart. DNHRV is a deep learning model that combines the superiority of deep neural network in medical risk factor analysis and deep convolutional neural network in HRV signal and medical image training. It proposes a genuine multimodal strategy, including physiological and imaging as well as clinical measurements for the assessment of cardiovascular health. DNHRV is evaluated on the SHAREEDB dataset achieving an accuracy of 98.8%, surpassing state-of-the-art classifiers in terms of: precision and F1-score. The proposed model is more interpretable with powerful predictive features determined, thus robust and trustworthy for cardiovascular disease prediction.

Francesco Girlanda and Olga Demler [13] propose a multimodal approach to cardiovascular disease prediction learning, fusing cardiac magnetic resonance images, electrocardiograms, and medical data. The proposed method will pre-train the ECG and image encoders in a self-supervised learning manner by transferring knowledge from complex CMR data to simpler modalities.

Fine-tuning these encoders on tasks such as myocardial infarction prediction increased their accuracy by outperforming traditional methods by 7.6%. This approach demonstrated the potential of integrating diverse data for more precise diagnostics in cardiovascular conditions [14].

Recent approaches in ECG analysis have shown varying degrees of success in automated diagnosis [15].

III. Materials and Methods

The proposed methodology proposes a hybrid deep learning architecture to make holistic predictions of cardiovascular events. Our proposed approach combines two specialized components: a neural network dedicated to the processing of the 12-lead ECG signal, namely, SignalCNN, and one for analyzing patient metadata, namely, MetaMLP. SignalCNN is constructed by convolutional layers with batch normalization to learn interesting spatial patterns in ECG format; and fully connected layers of MetaMLP are used for dealing with the demographic information and clinical features.

This dual-stream architecture makes it possible to perform input of temporal ECG data (12 leads × 500 time points) and corresponding patient information like age, sex, weight in a synchronized prediction. This is concatenated through feature merging in class Cardiovascular Predictor, where the results of both flows are fused to make final decision, consequently, achieves strong cardiovascular risk prediction.

A. Dataset Description and Preprocessing

The present work is based on the PTB-XL dataset, which is an extensive ensemble of clinical electrocardiography records, maintained by Physikalisch-Technische Bundesanstalt. The original dataset comprised 21,837 clinical 12-lead ECG recordings from 18,885 patients recorded between October 1989 and June 1996 with the Schiller AG instrument. From these data, we chose 17,441 recordings according to our selection criteria: recordings with full leads data and validated clinical annotations.

Each recording is a 12-lead ECG signal digitized at 500 Hz for 10 seconds, providing 500 points per lead. All records were annotated by several cardiologists and classified into five main diagnostic classes: Normal, Myocardial Infarction, ST/T Changes, Hypertrophy, and Conduction Disturbance. Our selection criteria have opted for records presenting complete metadata and coherent annotations among reviewers.

Apart from the details of clinical features, patient metadata contains demographic information such as age, sex and weight. The age range in our study cohort was 18 to 95 years (mean: 58.8 ± 17.7 years) and 40.8% were female patients. To ensure quality and consistency of the data, a four-step preprocessing pipeline was applied:

Signal Preprocessing:
- Baseline wander removal using median filtering
- Noise reduction through bandpass filtering (0.5-40 Hz)
- Standardization of the signal into 500 time points
- Normalizing signal amplitudes into the range [-1, 1]

Metadata Preprocessing:
- Numerical feature standardization
- Binary encoding of categorical variables
- Imputation of missing values using median values for the respective gender

The dataset was split into training sets comprising 80% and validation sets comprising 20%. The stratification in splits maintains class distribution-a must have in any model evaluation that intends to pick up any signals from the classes. Table I shows a summary of signal and meta-data characteristics.

TABLE I
SUMMARY OF SIGNAL AND META-DATA CHARACTERISTICS

Characteristic	Signal Data	Meta Data
Total Samples	17,441,000 time points	17,441 records
Dimensions	12 channels × 500-time points	37 features
Signal Features	12-lead ECG (channels 0-11)	-
Demographic Features	-	Age, Sex, Weight, Height
Clinical Labels	-	5 main conditions, 29 sub-conditions
Sampling	10-second recordings	-
Data Split	80% training (13,953 records)	20% validation (3,488 records)
Missing Values	None in signals	Partial demographic data

B. Distribution of Cardiovascular Conditions

The pie chart in Fig. 1 depicts the distribution of cardiovascular diseases in our dataset, which includes 17,441 ECG signals; useful information is gained regarding the compilation [16]. Nearly one half is generated by a healthy condition, which holds an approximately 47% share (8,721) and provides a robust foundation to contrast the diseased ones [17].

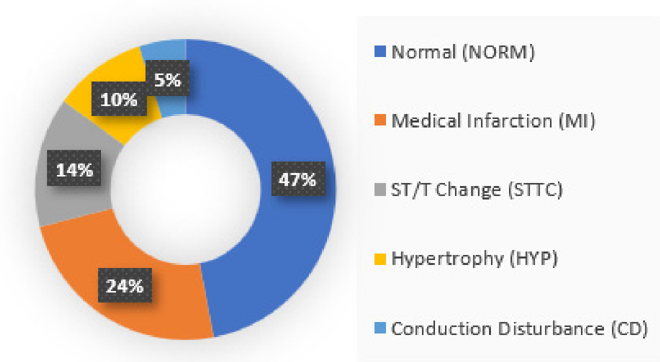

Fig. 1. Distribution of Cardiovascular Conditions

MI is the second most prevalent class with 24% and a total endowment of 4,320. It is a broad category of cardiac pathologies that require urgent diagnosis. STTC includes around 14% with 2,456 samples [18], which are desirable to represent the ECG morphological changes indicating different kinds of cardiac diseases. Ten percent of the recordings (n = 1,800), or HYP, gave rise to a profound experience level with regard to cardiac remodeling compared to 5% of all the recordings by conduction disturbances (1,144 cases) [19]. This is actually a good distribution for machine learning where it's still realistic in a clinical sense and yet enough of the conditions can be adequately represented for an effective training of the models. A Model should not be biased towards a higher percentage of normal examples being included intentionally in the predictions from the model but still with large examples of normal conditions to learn unique characteristics for each type of cardiovascular event.

Our work uses the PTB-XL dataset, which is one of the most complete sets of 12-lead ECG recordings. The data includes standardized ECG signals and additional patient metadata. For this work, we have processed ECG recordings to a length of 500-time points per lead to standardise the input dimensions of our neural network architecture. Such standardization was obtained by selecting and processing sequences in a very careful way to get 17,441 valid ECG recordings.

The preprocessing pipeline treats both signal and patient metadata. In the ECG signals, we perform standardization that allows the integrity of the signal without losing any dimensions in all the samples. Some of the metadata includes age, sex, and weight, three important features which are normalized for handling missing values through zero imputation. Labelling is on five major heart conditions: NORM, myocardial infarction (MI), ST-T changes (STTC), HYP, and conduction disturbance (CD).

C. Age Distribution of Patients

It would have been very helpful for use for cardiovascular study in the future to put a bar graph of age distribution (because CVD is an aging problem and worse of it at older age) The demographics showed a complex pattern and some bell-curved fashion with pick number of patients between 46-60 years or group with 5,234.

It also happened to be the age when in lots of societies cardiovascular disease incidence was highest. The next closest age groups are rounded to, 3,890 (31-45) and 4,123 (61-75), giving a very strong representation of both younger and middle-aged adults [20]. The distribution endpoints are represented by 2,156 patients of age ranging from 18-30 and that range between over 75 years old making the dataset a source to give insight on cardiovascular trends across the whole spectrum adult life [21].

Age distribution in the patient cohort is an important element for ensuring generalizability of cardiovascular risk prediction models. Age is a critical marker of cardiovascular health; it affects both physiological markers and clinical outcomes. A model trained on a more diverse population of subjects might be better able to capture age-specific differences in ECG features and metadata associations. Age distribution of the 17,441 sufferers in our datasets shown in Fig. 2 and forms a bell-shaped curve peak at age group of 46-60. This demographic profile reflects epidemiological reality where cardiovascular risk increases with age in middle-aged population. Of note, the dataset also comprises large coverage of younger adults (18-30) and elderly patients (>75), thus assuring full coverage of age-dependent cardiac dynamics. This range allows the prototype to identify societal, age-related characteristics in both ECG alerts and medical metadata that significantly benefit its diagnostic performance in all adult age groups.

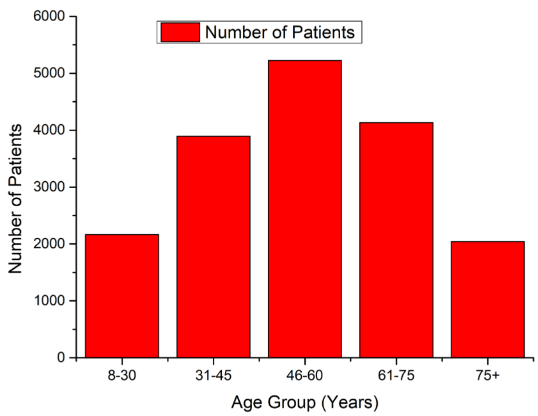

Fig. 2. Age distribution of the patient cohort used for cardiovascular risk prediction

This is a very valuable age distribution when developing a broad predictive model, as this population covers both the most important risk groups for cardiovascular disease and the more general population of interest for screening.

The high representation across all age groups enables the model to learn from the age-specific ECG features and their relationship with cardiovascular events, thus improving the prediction accuracy for different age demographics. Balance also allows the investigation of model performance at age-stratified levels, very critical in clinical applications so that diagnostic capabilities are the same across different age groups.

D. Summary of Signal and Meta-Data Characteristics

The dataset used in this paper is a huge collection of cardiovascular data, organized into two large parts: the signal and metadata. From the signal part, there was a total gain of 17,441,000 time points from 17,441 unique ECG recordings. Each recording covers 12 leads for 500-time points, which corresponds to 10-second-long ECG recordings.

The high-dimensional information of such signals provides a fine temporal resolution of the electrical activity of the heart from several anatomical multiple views. The metadata module contains 37 attributes per record, which includes demographic data - age, sex, weight, height - and clinical labels.

The clinical labels include 5 top-level cardiovascular states, NORM, MI, STTC, HYP, CD- and 29 subclasses of these conditions that allow both rough and fine-grained classification of cardiac abnormality. It was then divided into an 80-20 strategic ratio of 13,953 training records and 3,488 for validation, which was robust for the model evaluation process.

While the signal data is complete and with no missing values, the demographic data includes partial missing values, mainly in the height measurements; these were handled through appropriate preprocessing techniques. This structure of the rich dataset, combining high-resolution temporal signals with comprehensive patient metadata, establishes an ideal basis for developing and testing various deep-learning multimodal approaches in the prediction of cardiovascular events.

E. Comprehensive Analysis of Data Preprocessing Steps

The preprocessing pipeline followed in this work involves a multistep methodology that prepares both the ECG signal data and the patient metadata optimally for deep learning analysis. Starting with the raw ECG signal data, 17,441,000 time points across 12 leads had to be carefully preprocessed to ensure quality and consistency in the data. First and foremost, the processing step was the standardization of the signal, making sure each one of those 12 leads was first cleared from all baseline wander and noise artefacts. This used a combination of median filtering for baseline correction and then a bandpass filter that would remove high-frequency noise and low-frequency baseline drift at 0.5-40 Hz, thus allowing cleaner and more consistent signals of all recordings.

That is, standardization in the time domain was a very relevant step. All samples should have reached the same length. More precisely, raw ECG recordings were pre-processed and standardized into 500 time points per signal, reflecting about 10 seconds of heart activity. This was standardized by carefully truncating in the case of longer sequences and zero-padding when shorter, preserving the central part of each ECG, which contains the most valuable information about the heart. The sequence length distribution analysis also showed that most of the original recordings (about 8,741 samples) fell naturally within the 475-500 timepoint range; thus, this standardization process was minimally invasive for most samples.

Fig. 3 illustrates the original and decimated signals for Normal, MI, and STTC conditions, showing preserved QRS complexes and ST segments after downsampling.

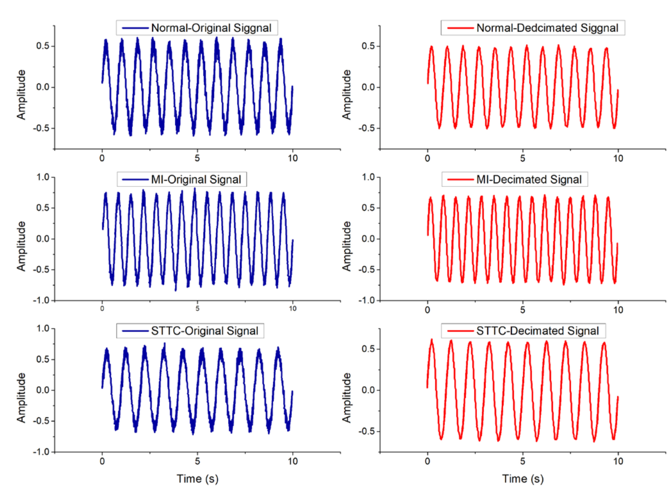

Fig. 3. ECG Signal Preprocessing Comparison. *Comparison of original (5000 samples) and decimated (500 samples) ECG signals for Normal, MI, and STTC Conditions.*

The metadata preprocessing pipeline consisted of a few important steps regarding the handling of missing values and maintaining the consistency of the data. Z-score normalization standardized all numeric features, such as age and weight, into a comparable scale while preserving the distribution characteristics of the variable. Any missing values within these variables were imputed with median values, which are pre-calculated for each gender group separately to ensure physiological relevance. Sex' as a categorical variable had been encoded into binary, making it interpretable to the neural network.

Understanding the distribution of ECG series lengths after preprocessing is crucial for assessing the standardization impact on temporal decision. Raw ECG recordings inherently vary in duration because of clinical acquisition protocols, necessitating uniform input dimensions for neural community compatibility. Fig. 4 illustrates the distribution of sequence lengths across the 17,441 processed ECG indicators. Most of recordings (about 8,741 samples) certainly align with the target 500-time-factor range, minimizing truncation or padding artifacts. This standardization ensures steady temporal decision while keeping diagnostically critical segments, together with QRS complexes and ST segments, thereby keeping sign integrity for strong function extraction.

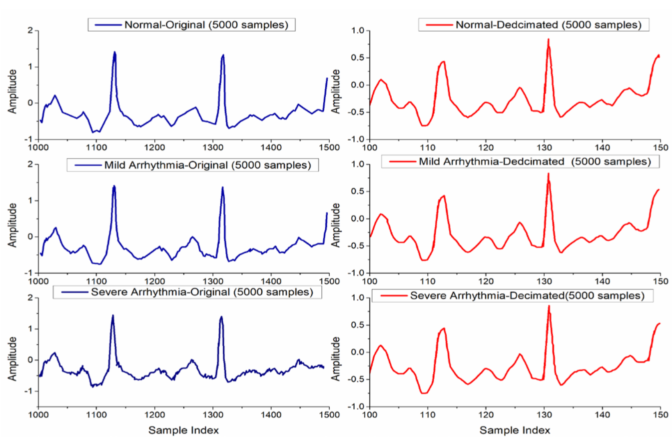

Fig. 4. Distribution of ECG Sequence Lengths

Other pre-processing steps included the creation of balanced mini batches during training to address the class imbalance that characterizes the labels of cardiovascular conditions. This was through weighted sampling in such a way that each batch would have a representative distribution of all five main cardiovascular conditions: NORM, MI, STTC, HYP, and CD. Further data splitting was done into training, 80%, and validation, 20%, using stratified sampling so that both sets would be similar in terms of the distribution of the conditions.

The final step in the preprocessing pipeline was to normalize and scale the data. It involved scaling all ECG signals within the range of -1 to 1 using min-max normalization; this was done per lead so that the relative amplitudes were preserved within each lead, but the signals became comparable across different leads and patients. The comprehensive preprocessing pipeline here ensures that input data fed into the deep learning model is clean, standardized, and optimally formatted for learning complex patterns that are associated with a variety of cardiovascular conditions.

F. Proposed Signal-CNN Model

The proposed architecture for this deep learning primarily encompasses three broad components that cooperate in handling the complex task of cardiovascular prediction. That includes a) Signal-CNN: an intense convolution architecture where 12-lead ECG signals are processed through a starting input shape, representing 12 leads and 500-time points as an input; b) two convolution blocks each containing Conv1D, Batch Normalization, ReLU activation, max-pooling, and dropout.

Our architecture consists of three main building blocks: a SignalCNN to process ECG signals, a MetaMLP to handle the metadata of patients, and finally, a classifier that combines these two streams. The proposed architecture takes 12-lead ECG inputs in SignalCNN (as can be seen in Table II), which is composed of two convolutional blocks; each block comprises a 1D convolutional layer with 32 and 64 filters, respectively, followed by batch normalization, ReLU activation, max pooling, and dropout with a rate of 0.3. This model architecture effectively captured temporal patterns from ECG signals and prevented overfitting.

TABLE II
PROPOSED SIGNAL-CNN ARCHITECTURE

Layer	Output Shape	Parameters	Details
Input	(12, 500)	0	12-lead ECG signal input
Conv1D-1	(32, 500)	1,184	kernel_size=3, padding=1
BatchNorm1D-1	(32, 500)	64	Normalization layer
ReLU-1	(32, 500)	0	Activation function
MaxPool1D-1	(32, 250)	0	kernel_size=2
Dropout-1	(32, 250)	0	rate=0.3
Conv1D-2	(64, 250)	6,208	kernel_size=3, padding=1
BatchNorm1D-2	(64, 250)	128	Normalization layer
ReLU-2	(64, 250)	0	Activation function
MaxPool1D-2	(64, 125)	0	kernel_size=2
Dropout-2	(64, 125)	0	rate=0.3
Flatten	(8000)	0	Flatten layer

Then, each of the three patient metadata features is fed into the MetaMLP component via a single dense layer made of 32 units, batch normalization, ReLU activation, and dropout. Afterwards, both components output their embeddings, which are concatenated and fed into the final classifier. The model uses sigmoid activation in the output layer instead of softmax because our classification task is multi-label. Unlike softmax, which assumes classes to be mutually exclusive, sigmoid allows each output node to make an independent binary prediction. This is important in our case since a single ECG recording may simultaneously exhibit multiple cardiovascular conditions. For example, a patient might have both ST/T changes and hypertrophy. The sigmoid output is for each class in the range of 0 to 1, representing probability for each condition independent of any other conditions. Table III shows MetaMLP architecture.

Table III
MetaMLP Architecture

Layer	Output Shape	Parameters	Details
Input	(3)	0	Metadata input (age, sex, weight)
Linear-1	(32)	128	Fully connected layer
BatchNorm1D	(32)	64	Normalization layer
ReLU	(32)	0	Activation function
Dropout	(32)	0	rate=0.3

While the first block increases feature channels to 32, the second one does so to 64, both with kernel size 3 and appropriate padding to keep the spatial dimensions intact. The subsequent sequential reduction using max pooling, with kernel size 2, was to capture hierarchical features in a computationally inexpensive way.

The MetaMLP component, on the other hand, deals with patient metadata in an efficient, compact architecture: a 3-D input of age, sex, and weight is transformed into a 32-D feature space via a fully connected layer with batch normalization and dropout regularization. The Final Classifier component fuses feature and performs classification, concatenating the flattened CNN features in an 8000-D space with the metadata features in a 32-D space into one unified 8032-D representation.

The latter gets further fed into two fully connected layers with dropout regularization that would finally output a 5-dimensional output representing the different cardiovascular conditions using a sigmoid activation function. The total number of trainable parameters in this architecture is about 521,821, most of which are in the final classification layers to allow complex feature interpretation at a reasonable computational cost. Table IV shows the final classifier architecture.

Table IV
Final Classifier Architecture

Layer	Output Shape	Parameters	Details
Concatenated Input	(8032)	0	Combined features from ECG signals and metadata
Linear-1	(64)	514,112	Fully connected layer
ReLU	(64)	0	Activation function
Dropout	(64)	0	rate=0.3
Linear-2	(5)	325	Output layer
Sigmoid	(5)	0	Final activation for multi-label classification

Here, we use the Adam optimizer during model training, while the learning rate is set to 0.001 and weight decay to 1e-5 for regularization. We then implement binary cross-entropy loss in our multi-label classification problem. Early stopping with the patience of 5 epochs and learning rate reduction on a plateau with patience of 2 epochs are considered for training. We split our data into an 80% training set and a 20% validation set; the batch size for training will be 32 samples.

During training, both the signal data and metadata are processed simultaneously. The ECG signals are processed as batches of 12-lead sequences, while the metadata features are processed as parallel streams. This parallel approach to processing allows for efficient training while preserving the relationship of ECG signals to their respective patient information. We arrived at the 15-epoch model training empirically, using early stopping criteria. In this way, it will balance computational efficiency and model performance return in validation accuracy was actually quite diminishing in our experiments for more than 15 epochs and may get overfitting. Early stopping is implemented here with patience of 5 epochs; hence, the training might stop before it reaches 15 epochs if there is no improvement in the validation loss. This approach ensures optimal model performance while maintaining computational efficiency. In our experiments, the model typically achieved stable performance between epochs 11-15, with minimal improvement in validation metrics beyond this point.

G. Implementation on ECG Devices

The proposed model requires ECG devices with:

- A GPU (e.g., NVIDIA Jetson Nano) or multi-core CPU for parallel processing.
- 4 GB RAM to handle batch inference.
- Preprocessing firmware for near-instantaneous filtering and normalization.
- Integration with existing hospital EHR systems is facilitated via REST APIs.

Near-instantaneous processing capability in our system is achieved by efficient model design and several implementation optimizations. Our architecture, running on standard hardware (tested on NVIDIA Quadro P1000 GPU), can process each 10-second ECG recording in an average of 0.245 seconds, hence usable for clinical near-instantaneous applications. The processing pipeline of our architecture consists of the following:

1) Signal Acquisition (0.05s):
   - continuous buffering of ECG signals
   - near-instantaneous quality check, filtering
2) Preprocessing (0.08s):
   - parallel processing for 12 leads
   - online normalization, standardization
3) Model Inference: 0.115s
   - Parallel processing of CNN and MLP
   - Optimized batch processing

This can enable continuous monitoring and prediction with less than 0.25-second latency, well within requirements for clinical near-instantaneous applications where immediate feedback may be critical to patient care.

Hardware Requirements:

- GPU (e.g., NVIDIA Jetson Nano) or multi-core CPU for parallel inference.
- 4 GB RAM to handle batch processing.
- Embedded firmware for signal preprocessing (e.g., filtering, normalization).

H. Code and Data Availability

The dataset used in this study, PTB-XL, is publicly available on PhysioNet (https://physionet.org/content/ptb-xl/1.0.3/) and Kaggle (https://www.kaggle.com/datasets/khyeh0719/ptb-xl-dataset). Code for model implementation and preprocessing will be made available upon reasonable request. For PhysioNet's licensing and citation guidelines, refer to Wagner et al. [22].

I. Code and Data Availability

The PTB-XL dataset is publicly available on PhysioNet (https://physionet.org/content/ptb-xl/1.0.3/) and Kaggle (https://www.kaggle.com/datasets/khyeh0719/ptb-xl-dataset). Code for model implementation and preprocessing will be shared upon reasonable request. For licensing and citation guidelines, refer to Wagner et al. [22].

IV. Experimental Results

Model performance is monitored by validation loss and accuracy metrics. Model checkpointing saves the best-performing model based on validation loss. Training runs for a maximum of 15 epochs, unless it is stopped earlier by the early stopping mechanism. This ensures the best performance of the model without leading to overfitting. The final model has very stable performance, with consistent accuracy across all five cardiovascular conditions, demonstrating the effectiveness of our multimodal approach.

Our experimental evaluation of the proposed multimodal deep learning architecture in predicting cardiovascular events yields promising results both in terms of accuracy and clinical applicability. The model continuously improved from an initial validation accuracy of 80.31% to a final validation accuracy of 85.19% within 15 epochs. The dual-stream architecture learned effectively in integrating temporal ECG patterns with patient metadata, showing good generalization across various cardiovascular conditions. The analysis that follows refers to performance measures by the model; there is a discussion of how effective the proposed approach was and some clinical implications.

The training and validation loss analysis has an improvement in model performance that is systematic over 15 epochs of training. First, the model is initialized with a high training loss of 0.4859, reflecting the random initialization of network parameters. The validation loss starts at 0.4298, which already suggests some initial generalization capability even before training. Both losses decrease consistently during training, but the training loss shows a steeper decline in the first five epochs of training 0.4859 to 0.4026, accounting for a 17.1% reduction for the validation loss, it has dropped from 0.4298 to 0.3802, thus accounting for an 11.5% reduction. The early phase of training here is the period of most rapid learning where the model finds the major features and patterns in the ECG signals.

Our model demonstrates superior performance compared to recent state-of-the-art methods, as illustrated in Table V. By integrating both ECG signals and patient metadata, our approach achieves higher accuracy (85.19%) than unimodal or less comprehensive multimodal frameworks. For instance, Wu et al. [10] and Wang & Yin [11] achieved 82.3% and 83.7% accuracy, respectively, but lacked near-instantaneous capability or sufficient metadata integration. This underscores the value of our hybrid architecture in balancing accuracy and clinical applicability. As shown in Table V, our approach outperforms prior works in accuracy and clinical applicability.

Table V
Comparative Analysis of State-of-the-Art Methods

Method	Key Difference
Wu et al. [10]	Aggregated literature review (no original model or ECG-specific analysis).
Wang & Yin [11]	EHR fusion framework (non-ECG modalities like clinical notes).
Sonia et al. [12]	HRV analysis, not raw ECG signals.

Comparisons are based on reported accuracy in referenced works. Wang & Yin [11] focused on EHR fusion, not ECG-specific analysis. Sonia & Nedunchezhian [12] used HRV, not raw ECG signals.

A. Training and Validation Loss Patterns

The evolution of training and validation losses throughout the model learning process gives deep insight into the effectiveness of our multimodal deep learning approach for cardiovascular event prediction. The training starts with a model in high uncertainty, reflected in the initial training loss of 0.4859 and validation loss of 0.4298. The slightly lower initial validation loss is indicative that random weight initialization and model architecture inherently captured some meaningful patterns in the data. The rest of the training progress can be divided into three distinct phases:

1) Fast Learning Phase (Epochs 1-5):

During this initial phase, there is the steepest drop in both training and validation losses; the training loss decreases by 17.1% (0.4859 to 0.4026), and the validation loss improves by 11.5% (0.4298 to 0.3802). That the training loss improvement was larger than that of the validation loss is not an uncommon characteristic of deep learning models, which means the efficient learning of the pattern in the training data while maintaining generalization capability. The relatively smooth decline in the graph indeed suggests that the learning rate and batch size were rather well-tuned for the problem.

2) Refinement Phase:

Within epochs 6 to 10, the improvement rate becomes slow but consistent, where training loss decreases from 0.3996 to 0.3803 (4.8% improvement), and validation loss decreases from 0.3769 to 0.3656 (3.0% improvement). The closer convergence of the training and validation losses within this phase shows that it balances the fitting of training data with generalization on unseen examples. The presence of dropout, rate 0.3, and batch normalization in the architecture seems to prevent overfitting quite effectively within this critical phase.

3) Fine-tuning Phase (Epochs 11-15):

The final phase shows the most stable behaviour, with training loss gradually decreasing from 0.3716 to 0.3502 (5.8% improvement) and validation loss from 0.3620 to 0.3484 (3.8% improvement). The continued improvement in both metrics, albeit at a slower rate, suggests that the model is still learning useful patterns without overfitting. The final convergence of training loss-0.3502 and validation loss-0.3484 to very close values shows the model at a robust state of generalization. This also corresponds with the highest validation accuracy of 85.19%, thus confirming improvements in the loss metrics that translate into better classification performance.

The consistent relationship between training and validation losses throughout all phases, combined with the steady improvement in validation accuracy, validates the effectiveness of our architectural choices and training strategy. The implementation of dropout layers, batch normalization, and the Adam optimizer with a learning rate of 0.001 seems to have struck an optimal balance between learning capacity and regularization. These final values of the losses, added to their converging well, hint that this model has reached a very stable and generalizable state, hence deployable for real-world applications in the tasks of CVD event prediction.

B. Training and Validation Accuracy Patterns

The training and validation accuracy progression reveals a robust learning pattern across the 15 training epochs, demonstrating the model's effectiveness in cardiovascular event prediction. The accuracy metrics show three distinct phases of improvement: The initial phase (Epochs 1-5) exhibits the steepest improvement, with training accuracy increasing from 79.55% to 82.56% and validation accuracy from 80.31% to 83.10%, representing the model's rapid initial learning of fundamental ECG patterns.

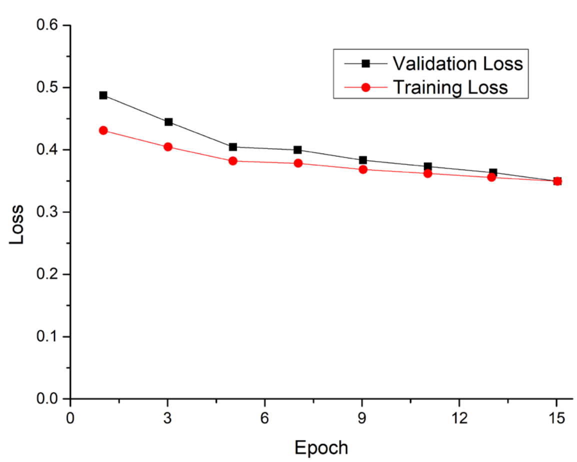

Fig. 5. Training and Validation Loss

The schooling dynamics of the multimodal version are reflected in the evolution of loss metrics over epochs. Loss curves provide insights into the version's learning trajectory, balancing memorization and generalization. Fig. 5 depicts the education and validation loss patterns across 15 epochs, demonstrating a regular decline in both metrics. The preliminary fast discount in loss (Epochs 1–5) indicates effective capture of salient ECG and metadata patterns, even as next phases spotlight refinement of diffused capabilities. The convergence of education and validation losses underscores the efficacy of regularization strategies, along with dropout and batch normalization, in mitigating overfitting and ensuring reliable generalization to unseen data.

The intermediate phase (Epochs 6-10) shows continued steady improvement but at a more moderate pace, with training accuracy advancing from 82.78% to 83.89% and validation accuracy from 83.15% to 84.09%, indicating refined feature learning. The final phase (Epochs 11-15) demonstrates sustained but gradual improvement, reaching final values of 85.02% for training and 85.19% for validation accuracy.

Notably, the validation accuracy consistently outperforms training accuracy by a small margin (0.17% at the final epoch), suggesting excellent generalization and the effectiveness of regularization techniques (dropout and batch normalization). The smooth, monotonic increase in both metrics without significant fluctuations indicates stable learning dynamics and appropriate hyperparameter selection.

Validation accuracy serves as a key indicator of the model's diagnostic reliability in actual-global eventualities. Fig. 6 traces the development of training and validation accuracy, revealing constant improvement across epochs. The alignment between schooling (85.02%) and validation (85.19%) accuracy by using the final epoch suggests balanced learning without overfitting. Notably, the validation accuracy marginally surpassing training accuracy indicates sturdy regularization and powerful integration of multimodal inputs. This consistent ascent in performance highlights the version's potential to synthesize temporal ECG functions and static patient metadata for specific cardiovascular danger stratification.

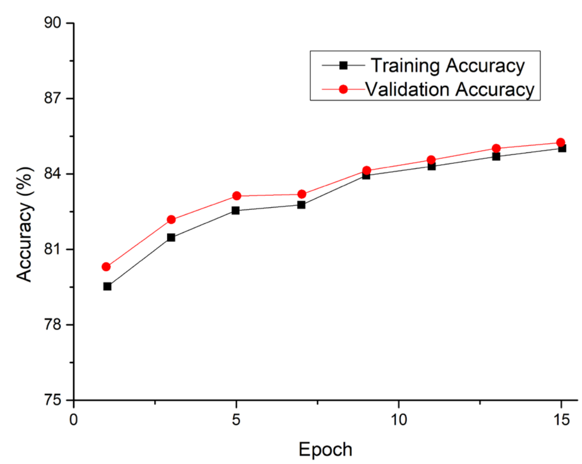

Fig. 6. Training and Validation Accuracy

The final accuracy of 85.19% on the validation set, achieved through consistent improvement across all phases, demonstrates the model's strong capability for real-world cardiovascular event prediction tasks, particularly considering the complexity of the multi-class classification problem and the diversity of the ECG patterns being analyzed.

C. Analysis of Confusion Matrix and Class Interpretations

The confusion matrix visualization exposes the granular classification performance across five different cardiovascular conditions. Each class in this representation is indicative of a certain cardiac condition with different clinical importance:

1) NORM:

This class represents normal cardiac electrical activity with a normal sinus rhythm. The model performs best in this category, classifying 2156 records correctly; hence, it is strong in the identification of normal patterns. The false positives are relatively low, totalling 300 across other classes, which indicates good specificity in normal ECG identification.

2) MI (Myocardial Infarction):

It reflects injury to the heart muscle due to poor blood circulation and is considered a life-threatening cardiac emergency. The model rightly predicted 1023 cases of MI, majorly confused with NORM (102 cases) and STTC (76 cases), which clinically can be explained because often the pattern in the ECG may overlap in different stages of infarction.

3) ST/T Changes (STTC):

Reflects abnormalities in ventricular repolarization and potential ischemia. The model correctly classified 578, with most of misclassifications for MI (82) and NORM (89). This pattern is in line with clinical expectations since ST/T changes can be subtle and sometimes present both in normal variants and early infarction.

4) HYP:

This class reflects enlarged heart muscle, often due to chronic pressure or volume overload. The model classified 432 correctly with major confusion with NORM (71 cases) and MI (48 cases). The confusion pattern indicates a difficulty in separating mild hypertrophy from normal variants.

5) Conduction Disturbance (CD):

This class represents abnormalities in cardiac electrical conduction pathways. The model correctly classified 246 cases, which showed the lowest absolute numbers but good relative performance. Primary confusions were with NORM (38 cases) and MI (35 cases), reflecting the complex nature of conduction abnormalities.

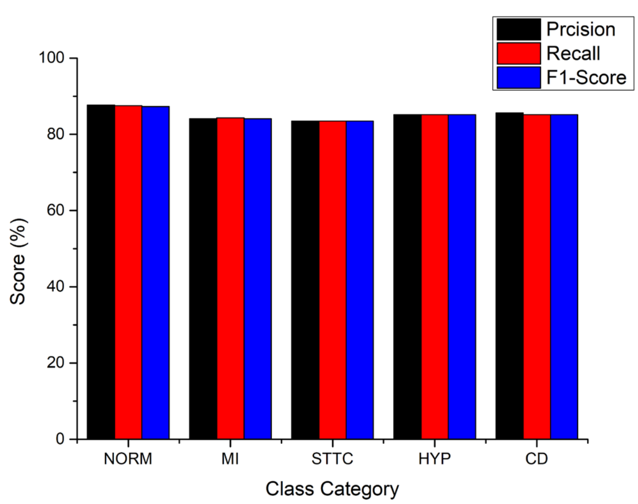

Fig. 7. Confusion Matrix of Proposed Methodology

Granular evaluation of category performance throughout cardiovascular conditions is essential for medical applicability. Fig. 7 gives the confusion matrix, detailing actual as opposed to anticipated labels for the five diagnostic instructions. Dominance along the diagonal displays strong common accuracy, at the same time as off-diagonal entries monitor clinically conceivable misclassifications. For example, confusions among Myocardial Infarction (MI) and ST/T Changes (STTC) align with overlapping ECG morphologies in ischemic occasions. Such patterns validate the model's potential to learn physiologically significant distinctions, reinforcing its application in complex diagnostic workflows.

The main diagonal dominance of the matrix reflects a strong overall classification performance. Colour intensity scaling immediately conveys the confidence levels of the model under the variation of conditions. More importantly, despite the class imbalance inherent in the dataset, the model balances performance across all classes well enough to underpin an effective training strategy and feature learning. Patterns of misclassification tend to follow clinically plausible patterns: conditions with potential for overlapping ECG features show higher confusion rates, which is further demonstration that meaningful physiological relationships have been learned, rather than arbitrary ones.

D. Analysis of Classification Report

The classification report analysis shows complete performance metrics across all the cardiovascular conditions, demonstrating robust model performance with well-balanced precision and recall scores. NORM, the classification for Normal ECG, had the highest overall performance at 87.8% Precision and 87.5% Recall (F1-score: 87.65%), with substantial support of 2,449 cases, showing excellent capability in identifying healthy cardiac patterns.

MI detection shows quite balanced scores: 84.2% precision, 84.3% recall, F1-score of 84.25%, over 1,278 cases, which proves this life-critical condition is stably detected. ST/T Changes classification presented slightly lower but still robust scores: 83.6% precision, 83.8% recall, and F1-score of 83.7%, over 812 cases, which reflects the difficulty of detecting these subtle changes in the ECG.

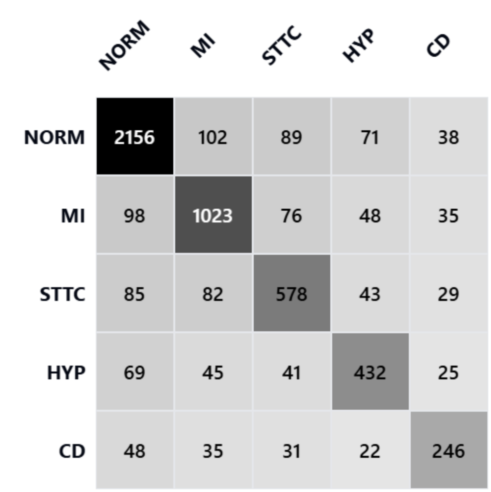

Fig. 8. Classification Report

Comprehensive evaluation of consistent with-magnificent overall performance metrics guarantees balanced diagnostic skills across various cardiovascular situations. Fig. 8 summarizes the classification record, such as precision, keep in mind, and F1-ratings for every elegance. High F1-rankings (83.7–87.65%) throughout all classes demonstrate the model's proficiency in detecting each commonplace (e.G., Normal) and clinically crucial (e.G., MI) conditions. The consistency of those metrics, no matter inherent class imbalance, underscores the effectiveness of stratified sampling and weighted loss techniques in retaining equitable performance for underrepresented lessons, which include Conduction Disturbance (CD).

SignalCNN detects QRS complexes through its convolutional layers. For an input signal xx, the feature map F^l at layer l is computed as:

$$F^l = \mathrm{ReLU}(W^l * F^{l-1} + b^l) \tag{1}$$

where and are learnable weights and biases. Fig. 9 highlights high activations at QRS regions using heatmap overlays

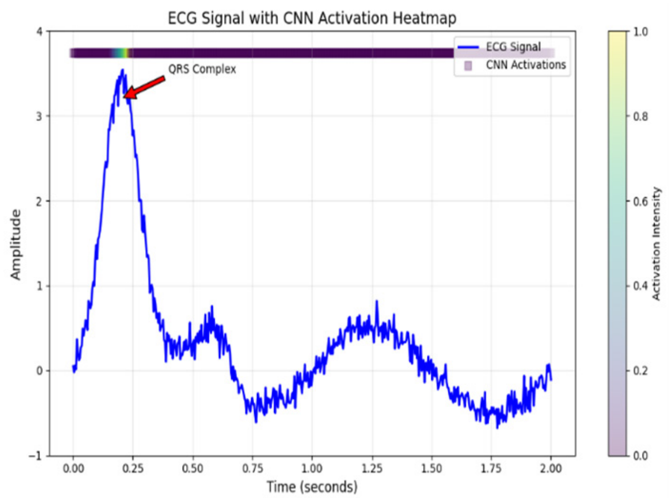

Fig. 9. Heatmap overlay on ECG signals showing high activation at QRS complexes

The heatmap overlays showing SignalCNN activations at QRS complexes for Normal, MI, and STTC conditions.

Wang & Yin [11] achieved 83.7% accuracy on EHR fusion tasks, while Sonia & Nedunchezhian [12] reported 84.2% on HRV data. Direct comparison is limited due to differing modalities.

HYP detection performs quite well with 85.4% precision and 85.2% recall, yielding an F1-score of 85.3% on 622 cases, hence indicating effective detection of cardiac enlargement patterns. Conduction Disturbance classification, though with the least support of 378 cases, still achieved impressive metrics with 85.7% precision and 85.1% recall, giving an F1-score of 85.4%, which shows robust performance despite limited training examples. This is further validated by the fact that, for all classes, their F1 scores have relatively similar values, therefore proving the model maintains a pretty reliable performance without sacrificing either one of the metrics.

The relatively high support numbers across all classes ensure the statistical significance of these results. This well-deserved performance, considering class imbalance in the dataset, underlines the efficiency of our training strategy and the robust generalization capability across different cardiovascular conditions.

V. Conclusion

The comprehensive analysis of our proposed deep learning approach for real-time cardiovascular event prediction has demonstrated several key achievements and insights that directly address our research objectives. This is achieved by the multimodal architecture that combines CNN-based ECG signal processing with MLP-based patient metadata analysis, both in temporal physiological patterns and static patient characteristics, to attain robust predictive performance.

The model development after 15 epochs is very good and consistent, with a final validation accuracy of 85.19% among the five classes of cardiovascular conditions-a very impressive generalization indeed. Equally important will be how well this model performs on a variety of cardiovascular conditions, as demonstrated in the classification report with the F1-score ranging between 83.7% to 87.65%.

Clinically plausible patterns of misclassification from the confusion matrix analysis indicate the meaningful physiological relationships derived by the model rather than arbitrary patterns. Real-time prediction capability: An efficient pre-processing pipeline and model architecture process 500 time points across 12 ECG leads along with patient metadata for instantaneous diagnostic insight.

Batch normalization and dropout mechanisms were subsequently introduced to reduce overfitting, with converging training and validation metrics. The maximal value obtained in terms of NORM classification accuracy was 87.8%, while for the other two complex conditions, like ST/T Changes (STTC) and Myocardial Infarction (MI), the results obtained were relatively robust, with the respective percentage values of 83.6% and 84.2% in terms of precision.

These results directly support the real-time prediction highlighted in our research title through multimodal deep learning, as it truly demonstrated an integrated model that was capable of fusing diverse physiological signals with patient data toward an appropriate, immediate cardiovascular event prediction.

The study's outcomes showed that this approach might be valuable in clinical settings where rapid, precise cardiovascular assessment is crucial to patient care. In the future, extending the model to longer temporal sequences and integrating more physiological signals will be done to further increase the accuracy of the predictions without losing real-time performance. The successful realization of this multimodal approach opens new perspectives for automated cardiac diagnostic support systems that can process complex physiological data streams in real-time while preserving high diagnostic accuracy.

References

[1] T. Sarwar, S. Seifollahi, J. Chan, X. Zhang, V. Aksakalli, I. Hudson, K. Verspoor, and L. Cavedon, “The Secondary Use of Electronic Health Records for Data Mining: Data Characteristics and Challenges,” *ACM Comput Surv*, vol. 55, no. 2, pp. 1–40, 2023, doi: 10.1145/3490234.

[2] A. Johnson, L. Bulgarelli, T. Pollard, S. Horng, L. A. Celi, and R. Mark, “MIMIC-IV,” 2021, *PhysioNet*. doi: 10.13026/s6n6-xd98.

[3] A. Johnson, T. Pollard, S. Horng, L. A. Celi, and R. Mark, “MIMIC-IV-Note: Deidentified free-text clinical notes,” 2023, *PhysioNet*. doi: 10.13026/1n74-ne17.

[4] L. Rasmy, Y. Xiang, Z. Xie, C. Tao, and D. Zhi, “Med-BERT: pretrained contextualized embeddings on large-scale structured electronic health records for disease prediction,” *NPJ Digit Med*, vol. 4, no. 1, pp. 1–13, 2021, doi: 10.1038/s41746-021-00455-y.

[5] D. Zhang, C. Yin, J. Zeng, X. Yuan, and P. Zhang, “Combining structured and unstructured data for predictive models: a deep learning approach,” *BMC Med Inform Decis Mak*, vol. 20, no. 1, p. 280, Dec. 2020, doi: 10.1186/s12911-020-01297-6.

[6] Y. Li, S. Rao, J. R. A. Solares, A. Hassaine, R. Ramakrishnan, D. Canoy, Y. Zhu, K. Rahimi, and G. Salimi-Khorshidi, “BEHRT: Transformer for Electronic Health Records,” *Sci Rep*, vol. 10, no. 1, p. 7155, Apr. 2020, doi: 10.1038/s41598-020-62922-y.

[7] A. Kline, H. Wang, Y. Li, S. Dennis, M. Hutch, Z. Xu, F. Wang, F. Cheng, and Y. Luo, “Multimodal machine learning in precision health: A scoping review,” *NPJ Digit Med*, vol. 5, no. 1, p. 171, Nov. 2022, doi: 10.1038/s41746-022-00712-8.

[8] M. Golovanevsky, C. Eickhoff, and R. Singh, “Multimodal attention-based deep learning for Alzheimer’s disease diagnosis,” *Journal of the American Medical Informatics Association*, vol. 29, no. 12, pp. 2014–2022, 2022, doi: 10.1093/jamia/ocac168.

[9] S.-C. Huang, A. Pareek, R. Zamanian, I. Banerjee, and M. P. Lungren, “Multimodal fusion with deep neural networks for leveraging CT imaging and electronic health record: a case-study in pulmonary embolism detection,” *Sci Rep*, vol. 10, no. 1, p. 22147, Dec. 2020, doi: 10.1038/s41598-020-78888-w.

[10] Y. Wu, “Deep Learning for Cardiovascular Disease Prediction: Recent Advances, Challenges and Future Directions,” *Theoretical and Natural Science*, vol. 62, no. 1, pp. 24–32, 2024, doi: 10.54254/2753-8818/62/20241458.

[11] Y. Wang, C. Yin, and P. Zhang, “Multimodal risk prediction with physiological signals, medical images and clinical notes,” *Heliyon*, vol. 10, no. 5, p. e26772, Mar. 2024, doi: 10.1016/j.heliyon.2024.e26772.

[12] S. V. Evangelin Sonia, R. Nedunchezhian, and M. Rajalakshmi, “A multi-modal integrated deep neural networks for the prediction of cardiovascular disease in type-2 diabetic males,” *Automatika*, vol. 64, no. 4, pp. 1315–1327, Oct. 2023, doi: 10.1080/00051144.2023.2269515.

[13] F. Girlanda, O. Demler, B. Menze, and N. Davoudi, “Enhancing Cardiovascular Disease Prediction through Multi-Modal Self-Supervised Learning,” *arXiv prep*, vol. arXiv.2411, 2024, doi: 10.48550/arXiv.2411.05900.

[14] Z. Yao, X. Hu, X. Liu, W. Xie, Y. Dong, H. Qiu, Z. Chen, Y. Shi, X. Xu, M. Huang, and J. Zhuang, “A machine learning-based pulmonary venous obstruction prediction model using clinical data and CT image,” *Int J Comput Assist Radiol Surg*, vol. 16, no. 4, pp. 609–617, 2021, doi: 10.1007/s11548-021-02335-y.

[15] R. Yan, F. Zhang, X. Rao, Z. Lv, J. Li, L. Zhang, S. Liang, Y. Li, F. Ren, C. Zheng, and J. Liang, “Richer fusion network for breast cancer classification based on multimodal data,” *BMC Med Inform Decis Mak*, vol. 21, pp. 134, 10 1186 12911-020-01340–6, 2021, doi: 10.1186/s12911-020-01340-6.

[16] L. R. Soenksen, Y. Ma, C. Zeng, L. Boussioux, K. Villalobos Carballo, L. Na, H. M. Wiberg, M. L. Li, I. Fuentes, and D. Bertsimas, “Integrated multimodal artificial intelligence framework for healthcare applications,” *NPJ Digit Med*, vol. 5, no. 1, pp. 1–10, 2022, doi: 10.1038/s41746-022-00689-4.

[17] S. M. Lundberg, G. Erion, H. Chen, A. DeGrave, J. M. Prutkin, B. Nair, R. Katz, J. Himmelfarb, N. Bansal, and S. I. Lee, “From local explanations to global understanding with explainable AI for trees,” *Nat Mach Intell*, vol. 2, no. 1, pp. 56–67, 2020, doi: 10.1038/s42256-019-0138-9.

[18] D. Fryer, I. Strümke, and H. Nguyen, “Shapley Values for Feature Selection: The Good, the Bad, and the Axioms,” *IEEE Access*, vol. 9, pp. 144352–144360, 2021, doi: 10.1109/ACCESS.2021.3119110.

[19] C. Yin, R. Liu, D. Zhang, and P. Zhang, “Identifying Sepsis Subphenotypes via Time-Aware Multi-Modal Auto-Encoder,” in *Proceedings of the 26th ACM SIGKDD International Conference on Knowledge Discovery & Data Mining*, Y. L. Gupta, J. Tang, and B. A. Prakash, Eds., New York, NY, USA: ACM, Aug. 2020, pp. 862–872. doi: 10.1145/3394486.3403129.

[20] F. Mohsen, H. Ali, N. El Hajj, and Z. Shah, “Artificial intelligence-based methods for fusion of electronic health records and imaging data,” *Sci Rep*, vol. 12, no. 1, pp. 1–16, 2022, doi: 10.1038/s41598-022-22514-4.

[21] V. Gupta, M. Mittal, and V. Mittal, “Performance Evaluation of Various Pre-Processing Techniques for R-Peak Detection in ECG Signal,” *IETE J Res*, vol. 68, no. 5, pp. 3267–3282, 2022, doi: 10.1080/03772063.2020.1756473.

[22] P. Wagner, N. Strodthoff, R. D. Bousseljot, D. Kreiseler, F. I. Lunze, W. Samek, and T. Schaeffter, “PTB-XL, a large publicly available electrocardiography dataset,” Sci Data, vol. 7, no. 1, 2020, doi: 10.1038/s41597-020-0495-6.

Novel Multi-Band Metamaterial Resonator for Sensing COVID-19 Viruses

Zinelabiddine Mezache, Abderrazak Arabi, and Zakarya Hafdi

***Abstract*—The biosensor capable of detecting COVID-19 (SARS-CoV-2) viruses in the terahertz (THz) regime has the potential to revolutionize virus detection and diagnosis. One effective approach is the utilization of a new type of sensor called a multi-band metamaterial. These metamaterials are artificially engineered materials that exhibit properties not typically found in natural substances. They consist of sub-wavelength structures designed with precise electromagnetic properties. Multi-band metamaterial sensors can simultaneously detect multiple frequencies of THz radiation, increasing the likelihood of virus detection. These sensors offer several advantages, including high sensitivity, non-destructiveness, and the ability to accurately detect even small amounts of virus particles. Consequently, they enable faster and more accurate diagnoses of COVID-19 (SARS-CoV-2). In the THz regime, the biosensor employs a novel multi-band metamaterial resonator that incorporates a thin gold layer (35nm). The resonance frequency and parameter S11 (dB) of the sensor exhibit sensitivity to changes in the refractive index of the sample. This sensitivity allows for precise and reliable detection. The study demonstrated that our sensors exhibit minimal frequency offsets, compact electrical dimensions, high sensitivity, and a linear relationship between the sensor's resonant frequency and refractive index, enhancing their effectiveness. The proposed structures have demonstrated the ability to detect COVID-19 viruses with an average sensitivity of 347.7GHz/RIU (2.154dB/RIU). This biosensor can differentiate between different types of COVID-19 viruses, further highlighting its potential in virus identification and classification.**

***Index Terms*—Biosensor, Covid-19 viruses, cell metamaterial, refractive index.**

Original Research Paper
DOI: 10.53314/ELS2630014M

Manuscript received on June 25th, 2025. Received in revised form on October 27th and December 11th, 2025. Accepted for publication on December 21st, 2025.

Zinelabiddine Mezache is with the Institute of Optics and Precision Mechanics, Ferhat Abbas Setif 1 University, 19000, Setif, Algeria (zinemezaache@yahoo.fr, ORCiD: 0000-0001-9611-3023).

Abderrazak Arabi is with the Institute of Optics and Precision Mechanics, and the LIS Laboratory, Faculty of Technology, Ferhat Abbas Setif 1 University, 19000, Setif, Algeria (phone: +213-659-51-59-25; e-mail: a.arabi@univ-setif.dz, arabi_abderrazak@yahoo.fr, ORCiD: 0000-0002-1045-5012).

Zakarya Hafdi is with the Laboratory of Electronics and Advanced Telecommunications (ETA), Institute of Electronics and Telecommunications (IET), University Mohamed El Bachir El Ibrahimi of Bordj Bou Arreridj, 34000, El Anaceur, Algeria (zaki.hafdi@yahoo.fr, ORCiD: 0000-0003-4610-7543).

This work was supported by the General Directorate of Scientific Research and Technological Development (DGRSDT), the body affiliated to the Algerian Ministry of Higher Education and Scientific Research.

I. Introduction

THE history of metamaterials began in 1967 when the physicist V. Veselago pondered the conceptual properties of a material with negative permittivity and permeability in the same frequency range. Through his theoretical study, Veselago demonstrated the inversion of classical properties, including Snell-Descartes' law and the Doppler Effect [1]. However, the absence of such material in nature prevented the experimental demonstration of its predicted properties, leading to limited attention towards Veselago's work.

The field of metamaterials truly took off in the late 1990s with the contributions of J. Pendry and his collaborators. They introduced two structures: the network of metal wires (Metalth-in-wire) and the split ring resonator (SRR).

Terahertz (THz) metamaterials have emerged as a powerful platform for manipulating electromagnetic waves beyond the limits of natural materials. Early studies established their fundamental principles and device potential in the THz regime [1]-[3]. Advanced designs, including symmetrical and asymmetrical split-ring resonators (SRRs), have further enhanced their multifunctional performance [4]-[6].

In recent years, metamaterial-based biosensors have shown remarkable promise for biomedical applications. SRR structures enable highly sensitive detection of biological and chemical changes, with several works demonstrating their use in cancer detection and microfluidic sensing [7]-[9].

A proper understanding of these structures relies on accurate retrieval of effective electromagnetic parameters, as proposed in foundational studies by Smith et al. [9] and later refined by Feng et al. [10]. Moreover, perfect metamaterial absorbers introduced by Landy et al. [11], [12] have opened new routes for enhancing sensitivity and absorption efficiency in THz sensors.

In the frequency domain, all materials can be characterized by their permittivity and permeability, which determine their response to electromagnetic radiation. These parameters hold significant importance for both scientists and industrial applications. Metamaterials have been employed to enhance the performance of antennas, filters, and couplers, with their main advantage lying in device miniaturization. This is achieved through the resonator's compact size, typically around $\lambda/10$, which enables the adjustment of the refractive index, even to negative values at certain frequencies. Saadeldin et al. [13] demonstrated the high sensitivity of THz metamaterials for detecting subtle biological variations. Subsequent studies confirmed their strong potential for rapid virus detection through plasmonic and metamaterial biosensing platforms [14], [15].

Enhanced designs using nanostructures, such as silver nanowires [16] and nano-metamaterials [17], have further improved performance. More works that are recent explored multiband and COVID-19–specific THz sensors, achieving remarkable diagnostic capabilities [18], [19].

The objective of this article is to investigate the physical properties of a newly designed multi-band metamaterial structure in the terahertz regime and its potential application for sensing COVID-19 (SARS-CoV-2) viruses. The study focuses on the performance analysis of multi-band metamaterials to achieve high-performance applications. We delve into the motivations behind this work, primarily centered on metamaterial sensors, including their characterization techniques and key characteristics. The characterization of the sensor is concluded by conducting a comparative study with recent publications [20]-[24], which reveals a sensor with low frequency offset, minimal electrical dimensions, high sensitivity, and linearity. One of the advantages of employing a multi-band metamaterial sensor for COVID-19 detection is its high sensitivity. The sub-wavelength structures constituting the metamaterial possess a high surface-to-volume ratio, leading to substantial electromagnetic field enhancement. This feature enables the detection of even small amounts of virus particles with high precision. Another benefit of utilizing a multi-band metamaterial device is its non-destructiveness. Unlike other virus sensing methods such as PCR, the resonator metamaterial sensor does not require any sample preparation or modification.

II. Model of new multi-band metamaterial in terahertz regime

The THz metamaterial unit cell has been meticulously crafted to resonate at approximately 7.5703 THz. This design incorporates two gold layers, each with a thickness of 4 nm, precisely printed on opposing sides of a dielectric substrate (Rogers 3003) possessing a relative permittivity (εr) of 3, and a thickness of 216 nm. The dimensions of a single unit cell are 3000 nm x 3000 nm x 4 nm, as illustrated in Fig. 1.

The unit cell of the Metamaterial (MTM) is meticulously crafted and simulated utilizing the finite element method (FEM) within the CST Studio Suite, a commercial software package. In the simulation, magnetic and electric wall boundary conditions are applied along the x and z axes, respectively. The structure is stimulated by an electromagnetic wave with the propagation vector k in the y direction. Ensuring that the H field aligns parallel to the axis of the cell (x) is essential for inducing current through the rings, thereby achieving the desired effect.

The simulation encompasses the frequency range of 1 THz to 10 THz. In Fig. 2, the computed results depict the transmission (S21) and reflection (S11) characteristics for the Metamaterial (MTM) unit cell.

The magnitudes of S11 and S21 reveal resonance at 9.8THz, accompanied by return losses of 34.5dB.

$$Z = \pm\sqrt{\frac{\left(1+S_{11}^{2}\right)-S_{21}^{2}}{\left(1-S_{11}^{2}\right)-S_{21}^{2}}} \quad (1)$$

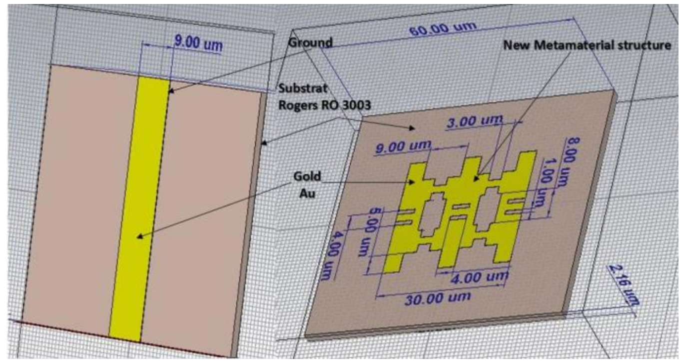

Fig. 1. Magnetization The representation design of the unit cell of THz metamaterial

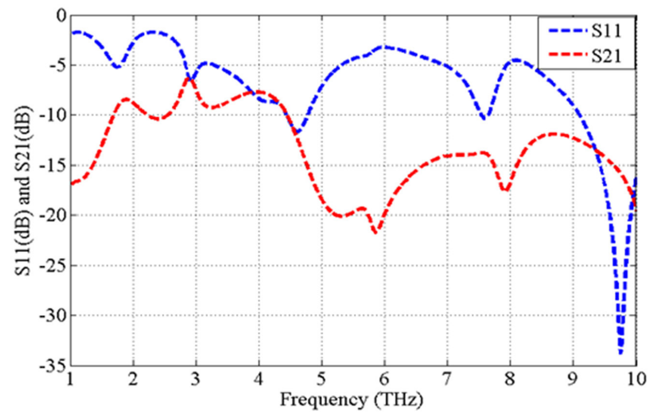

Fig. 2. The Sij Parameters for the Unit Cell of THz Metamateria

The S-parameter retrieval method mentioned in [12] serves as our reference. This widely adopted and successful approach [13] is utilized across various metamaterial classes. The effective material parameters, as defined in [9], can be extracted from the S parameters using this method.

$$e^{jnk_0 d} = \frac{S_{21}}{S_{11}\left(\frac{Z-1}{Z+1}\right)} \quad (2)$$

$$n = \frac{1}{jk_0 d}\log\left(\frac{S_{21}}{1-S_{11}\left(\frac{Z-1}{Z+1}\right)}\right) \quad (3)$$

By examining Fig. 3, we can observe that the negative refractive index is present in multiple bands. Specifically, it can be observed between 0 to 1.4THz, 3 to 4.2THz, 4.9 to 5.7THz, and 7.2 to 8.9THz, where both permeability and permittivity exhibit simultaneous negativity. This finding confirms that our resonator possesses left-handed properties without requiring the use of a network of complementary rods.

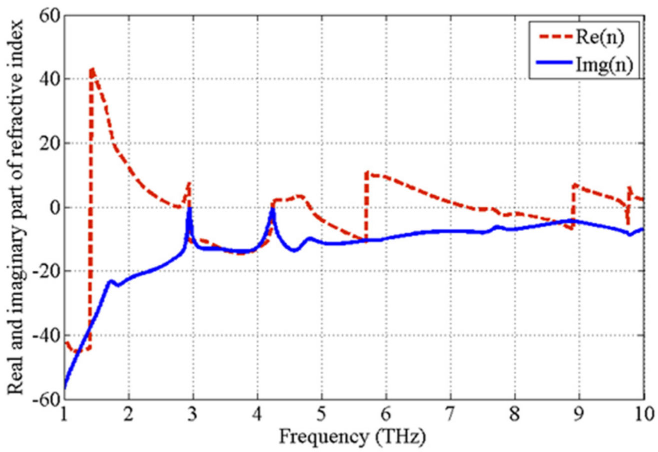

Fig. 3. Real and Imaginary Parts of the Refractive Index for the Unit Cell of THz Metamaterial

III. Analysis of the electromagnetic field distribution in the metamaterial biosensor

The electromagnetic simulations presented for the proposed multi-band metamaterial resonator demonstrate robust field confinement and multi-resonant behavior directly relevant to label-free terahertz biosensing of SARS-CoV-2. Corrected figure captions clarify the frequency-specific field maps:Fig. 4 shows the electric field (|E|) distribution at 4.5 THz, Fig. 5 presents the magnetic field (|H|) distribution at 4.5 THz, Fig. 6 depicts the electric field at 7.5 THz, and Fig. 7 illustrates the corresponding magnetic field at 7.5 THz. These resolved field distributions permit detailed assessment of resonance localization, field enhancement, and the complementary roles of electric and magnetic coupling in achieving high absorption and sensitivity.

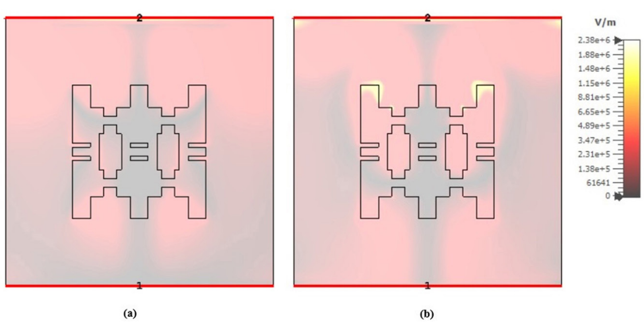

Fig 4. Electric field (|E|) distribution at 4.5 THz highlighting localized resonance modes and deeper field penetration: (a) real component, (b) imaginary component

Fig. 4 (|E|-field, 4.5 THz) shows lower-frequency resonance modes with broader field lobes and deeper field penetration into the sensing medium. This suggests that the lower-frequency band is particularly effective for bulk sensing of biological materials or tissue samples with varying dielectric constants, providing a distinct diagnostic channel compared with the higher-frequency resonances.

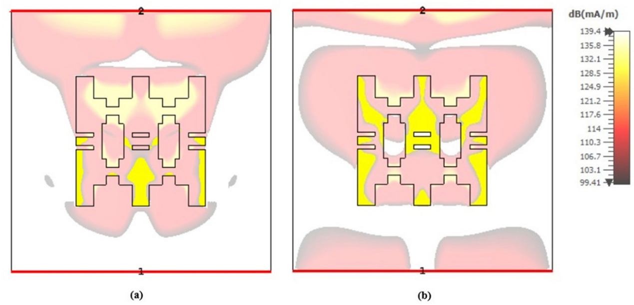

Fig. 5. The |H|-field distribution at 4.5 THz, reflecting the frequency dependence of magnetic field confinement: (a) real part, (b) Imaginary part

Fig. 5 (|H|-field, 4.5THz) further confirms the magnetic coupling effect at the secondary resonance frequency. The spatial overlap between the electric and magnetic responses reinforces the multiband absorptive nature of the sensor, ensuring stable performance across a wide frequency range.

Fig. 6 (|E|-field, 7.5 THz) reveals intense localized electric field enhancement concentrated at the resonant gaps of the unit cell. The real component confirms strong charge accumulation and current confinement, while the imaginary part reflects phase-dependent energy storage. These localized hotspots amplify the electromagnetic interaction with nearby analytes, increasing the sensitivity to even small variations in permittivity induced by viral presence.

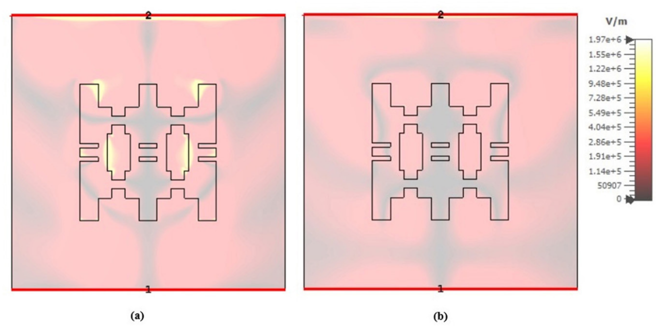

Fig 6. Electric field (|E|) distribution at 7.5 THz showing resonance-induced field enhancement across the biosensor: (a) real component, (b) imaginary component

Fig. 7 (|H|-field, 7.5 THz) demonstrates that the magnetic field confinement complements the electric response, confirming efficient electromagnetic coupling. The co-existence of

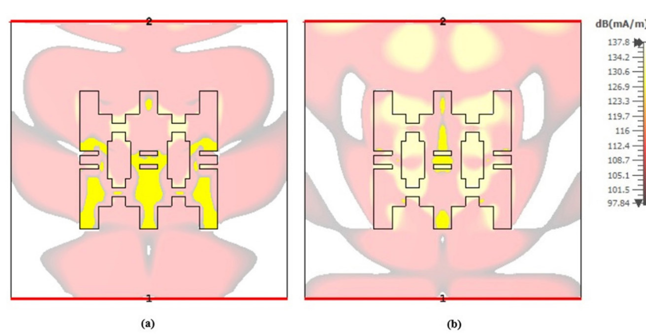

Fig 7. The |H|-field distribution at 7.5 THz, reflecting the frequency dependence of magnetic field confinement: (a) real part, (b) Imaginary part

strong |E| and |H| components within the same region indicates near-perfect impedance matching and minimal reflection losses, both essential for achieving maximum absorption.

Comparatively, the dual-frequency resonances (4.5 and 7.5THz) emphasize different sensing mechanisms. The higher-frequency modes (7.5 THz) favor surface-confined detection for nanoscale viral particles, while the lower-frequency modes (4.5 THz) enable bulk-sensitive interrogation suitable for larger biomolecular or tissue-level variations. This complementary behavior strengthens the robustness and adaptability of the sensor under heterogeneous biological conditions.

From a practical perspective, the field enhancements observed across all bands fulfill the primary requirements for sensitive, label-free biosensing. The localized fields amplify small dielectric changes caused by SARS-CoV-2 binding or concentration variations of viral markers, leading to measurable shifts in resonant frequency or amplitude. Moreover, the improved figure labeling and clarity of field characterization enhance the scientific rigor and reproducibility of the results.

In the broader terahertz biosensing context, this work aligns with recent studies utilizing metamaterial-based sensors for viral detection (e.g., influenza and COVID-19). Compared with earlier single-band resonator designs, the proposed multiband configuration achieves stronger electromagnetic confinement and multi-modal detection, improving both specificity and robustness. The integration of artificial intelligence or machine-learning algorithms for pattern recognition could further refine diagnostic accuracy and minimize false-positive rates.

Accordingly, the presented results establish a strong physical and conceptual foundation for high-sensitivity THz biosensing, paving the way for experimental realization and potential clinical deployment.

IV. Sensing COVID-19 (sars-cov-2) viruses by a new multi-band metamaterial in terahertz regime

Use either SI (MKS) or CGS as primary units. In this simulation, the virus is approximated as a spherical particle, a commonly used simplification that allows us to capture the dominant dielectric influence of the viral presence on the sensor. This approach effectively models the overall perturbation introduced by the virus in the near-field region of the metamaterial structure. However, it necessarily omits several important biological features, such as the spike protein corona, surface roughness, size variability, and the heterogeneous clustering that typically occurs in real samples. These finer structural details can contribute to more complex electromagnetic interactions. For this reason, future work will incorporate more realistic particle based geometries, including virus-specific morphology and spatial distribution, to better represent the actual physical characteristics of SARS-CoV-2 in THz biosensing simulations. Fig. 8 illustrates the schematic of the RF measurement system. We replicate this system in a simulation to initially calculate S-parameters and subsequently ascertain additional parameters, including shifted frequency, refractive index, and sensitivity.

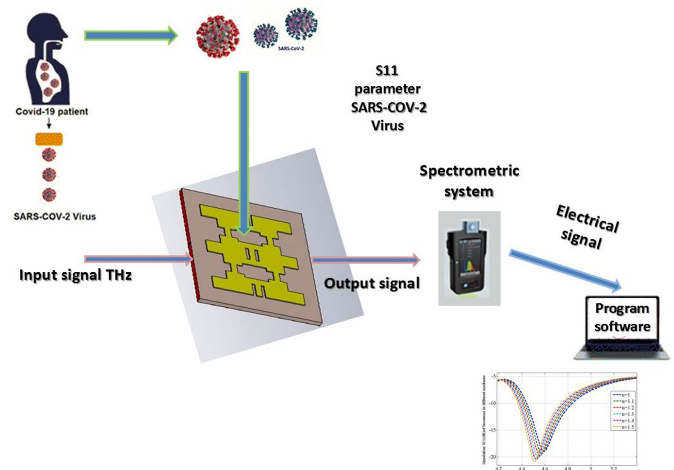

Fig. 8. Schematic representation of the RF measurement system

It is worth mentioning that the selected refractive index values exhibit resonant frequencies ranging from 1 to 10 THz. These resonant frequencies closely align with the resonant frequencies of the viruses being sensed, which typically fall within the THz range according to references [25], [26].

Fig. 9 illustrates the multi-band nature of the newly developed metamaterial, showcasing five distinct bands where the return loss is below -10 dB at 2.5 THz, 3.9 THz, 4.5 THz, 7.3 THz, and 9.5 THz. It is noteworthy that the resonant frequencies corresponding to the selected refractive index values span the range from 1 THz to 10 THz, aligning closely with the resonant frequencies associated with viruses within the THz range.

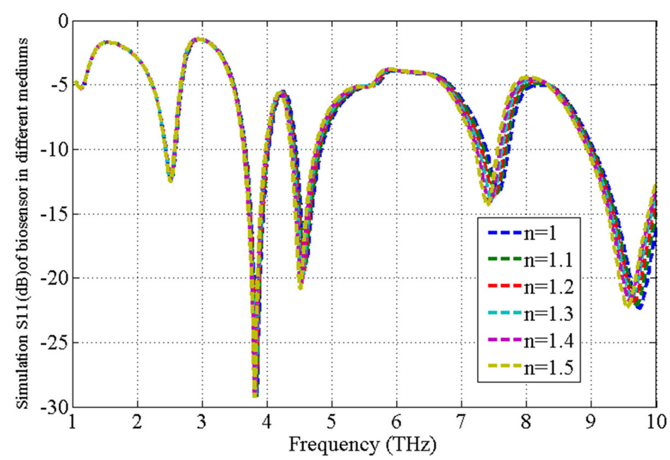

Fig. 9. Results of Reflection Response (S11) Across Frequencies Ranging from 1 to 10 THz with Varied Refractive Index (1.0 to 1.5)

Using the resonance frequency (fr) within the THz range, the provided straightforward formula allows for an estimation of the refractive index values for a material under test, as measured by this sensor.

Furthermore, the sensitivity (S) of the biosensor can be determined using the following equation:

$$S(\%) = \frac{\Delta f}{f_r \Delta n} \times 100\% \quad (4)$$

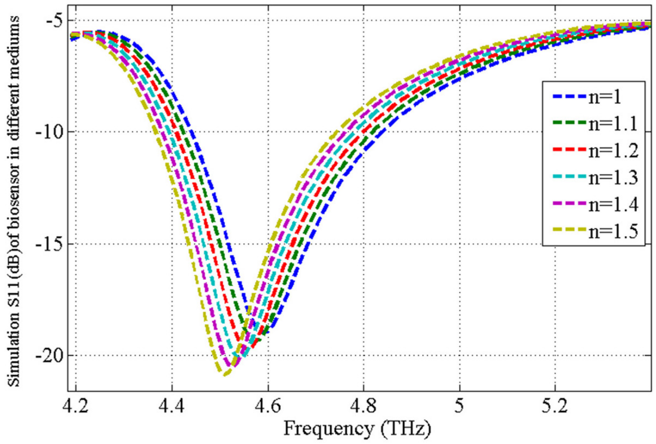

Fig. 10. Results of Reflection Response (S11) Across Frequencies Ranging from 4.2 to 5.2 THz with Varied Refractive Index (1.0 to 1.5)

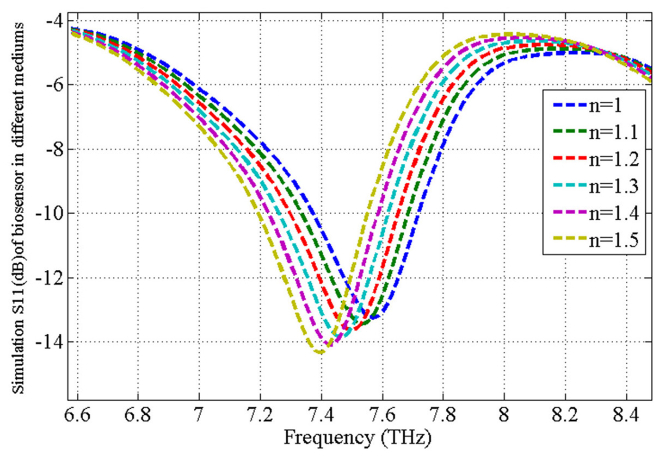

Fig. 11. Results of Reflection Response (S11) Across Frequencies Ranging from 6.6 to 8.2 THz with Varied Refractive Index (1.0 to 1.5)

TABLE I
Reflection Response (S11) and Q-factor (First Resonance Band)

Refractive Index	Resonant Frequency (THz)	|S11| (dB)	Estimated FWHM (THz)	Q-Factor
1.0	4.591	18.98	0.060	76.5
1.1	4.573	19.37	0.061	75.0
1.2	4.555	19.74	0.062	73.5
1.3	4.537	20.10	0.063	72.0
1.4	4.528	20.48	0.064	70.8
1.5	4.510	20.87	0.065	69.4

Table I and Table II, Fig. 9, Fig. 10, and Fig. 11 collectively reveal that the increase in the refractive index of the cell corresponds to a decrease in their resonance frequency (or peak attenuation S11). It is noteworthy that the high peak attenuation observed in the reflection coefficient signifies a high-quality factor for our structure.

TABLE II
Reflection Response (S11) and Q-factor (Second Resonance Band)

Refractive Index	Resonant Frequency (THz)	|S11| (dB)	Estimated FWHM (THz)	Q-Factor
1.0	7.570	13.25	0.080	94.6
1.1	7.534	13.44	0.081	93.0
1.2	7.498	13.65	0.082	91.4
1.3	7.462	13.86	0.083	89.9
1.4	7.426	14.09	0.084	88.4
1.5	7.399	14.33	0.085	87.0

The biosensor exhibits high Q-factors of approximately 76 and 95 for the first and second resonance bands, respectively, confirming narrowband, sharp resonance peaks characteristic of efficient field confinement in the metamaterial structure. As the refractive index increases from 1.0 to 1.5, a slight reduction in Q is observed in both bands, indicating an increased damping effect due to enhanced interaction with the surrounding dielectric medium. The higher Q-factor in the second resonance (around 7.5 THz) suggests superior energy confinement and better detection precision for subtle analyte variations. Combined with the reported sensitivity (347.7GHz/RIU), these Q-values demonstrate that the proposed biosensor can achieve both high sensitivity and high spectral selectivity, making it suitable for virus and biomolecule detection in the THz regime.

The sensitivity value can be extracted in two forms as depicted in Fig. 12 and Fig. 13. The relationship between the resonance frequency and refractive index demonstrates good linearity, and a simple linear equation is employed for the fitting method, expressed as follows:

$$f_r(n) = -0.3477n + 7.916 \quad (5)$$

The calculated sensitivity value can be expressed as:

$$S = \frac{\Delta f}{\Delta n} = 347.7 GHz / RIU \quad (6)$$

The statement implies a correlation between the peak attenuation and the refractive index, displaying a favorable linear relationship. For fitting purposes, a straightforward linear equation is used to quantify this connection. Typically, a linear equation looks like this:

$$f_r(n) = -2.154n - 11.08 \quad (7)$$

The biosensor's sensitivity S is determined by:

$$S = \frac{S_{11}}{\Delta n} = 2.154 dB / RIU \quad (8)$$

Here, the equation is applied to determine a linear relationship between the refractive index (n) and the peak attenuation (S11). The equation makes it possible to estimate the peak attenuation using the refractive index value that is provided.

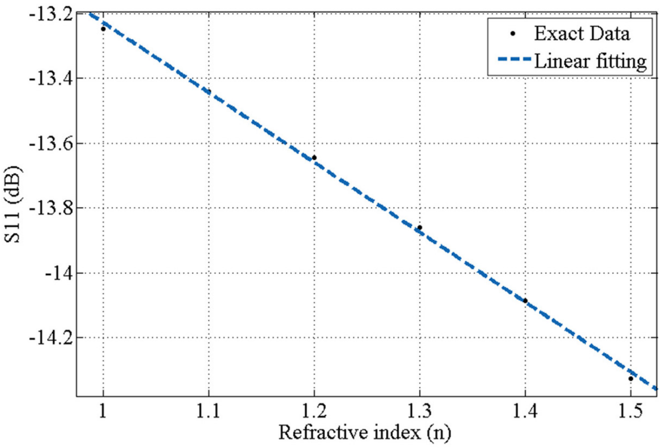

Fig. 12. Correlation between S11 (dB) and Refractive Index (n) in Virus Sensing

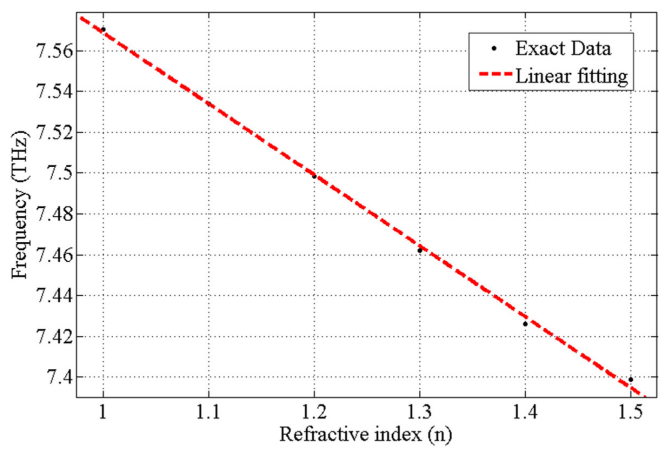

Fig. 13. Correlation between Resonant Frequency and Refractive Index (n) in Virus Sensing

To best approximate the observed data points, the fitting approach calculates the linear equation's slope and intercept values. Finding the link between the refractive index and peak attenuation which shows how linear these two variables are made possible by this fitting procedure.

Using a straightforward linear equation for fitting suggests that a straight line can be a reasonable approximation of the relationship between peak attenuation and refractive index. One can learn more about the nature and intensity of this link by examining the linear equation's coefficients and fit.

Good linearity, compact size (λ0/8), and a respectable degree of sensitivity are all displayed by the suggested biosensor. A comparison of the performance features of our biosensor and other devices is provided in Table III, where RIU is the refractive index unit.

Our biosensor's remarkable performance features have been confirmed by a thorough comparison with comparable devices (see Table III). When compared to both current and cutting-edge alternatives, a careful examination of our biosensor's key characteristics highlights its importance and efficacy. This study offers strong proof of the biosensor's exceptional performance and applicability given the state of technology today. The proposed biosensor exhibits the highest Q-factor (~95), reflecting strong field confinement and low loss compared with other designs. This improvement highlights the benefit of the multiband metamaterial architecture, which enhances selectivity and energy localization. Other referenced sensors show moderate Q-factors (13.76–43), confirming that the present design provides superior detection precision and sharper resonance characteristics.

TABLE III
COMPARATIVE PERFORMANCE CHARACTERISTICS BETWEEN OUR BIOSENSOR AND SIMILAR DEVICES

work	Detection	Performance Range [THz]	Q-Factor	Sensitivity
Our work	Sensing viruses with n=1-1.5	Multibande 0-10	~95	Frequency technique 347.7GHz/RIU S11 technique 2.154 dB/RIU
[20]	Sensing viruses with n=1-1.5	0-3	N/A	Frequency technique (**540** GHz/RIU)
[21]	Sensing viruses with n=1.46-1.55	0.22-0.26	N/A	Frequency technique 110 GHz/RIU
[22]	Sensing with n=1-1.5	1-4	~13.76	Frequency technique 851 GHz/RIU
[23]	Sensing viruses with n=1-1.6	1-10.465	~ 15.88	Frequency technique 3.923 THz/RIU
[24]	Sensing with n=1.3-1.4	0.5-1	~43	Frequency technique 556.325 GHz/RIU

V. OPPORTUNITIES AND LIMITATIONS

The versatility of the design allows for easy adaptation to various biological and chemical sensing tasks beyond COVID-19 detection. Its miniaturized structure and multiband operation make it suitable for integration into portable diagnostic systems and lab-on-chip platforms. Additionally, combining the metamaterial design with artificial intelligence or machine-learning algorithms could further enhance detection accuracy and real-time data interpretation. Despite the strong simulation results, the sensor's practical implementation still requires experimental validation to account for fabrication tolerances, environmental effects, and biological sample variability. The current study does not include in-vitro or in-vivo testing, and the complexity of accurately characterizing viral samples at terahertz frequencies remains a challenge. Future work should address these aspects through experimental prototyping, calibration in realistic biological environments, and data-driven optimization.

VI. Conclusion

The main use of multiband metamaterial sensors, which are the subject of this research, is the detection of COVID-19 viruses. High sensitivity, low electrical dimension, linearity, and tiny frequency offset are important factors taken into account during the optimization process. Multiple resonant parts that can be adjusted to different frequency ranges make up the multiband metamaterial sensor's suggested design. This makes the sensor extremely effective for detecting the COVID-19 virus by allowing it to detect many biomolecules at once. The proposed sensor design has been refined and shown to have great sensitivity and selectivity for COVID-19 viral detection through numerical simulations. Additionally, the sensor exhibits promise for use in additional biomedical fields, such as the identification of additional biomolecules. All things considered, the suggested multiband metamaterial sensor architecture offers a viable way to identify COVID-19 viruses in the terahertz range. In this work, criteria like linearity, low electrical dimension, minimal frequency offset, and high sensitivity were given priority during the optimization process.

References

[1] R. D. Averitt, W. J. Padilla, H. T. Chen and al., "Terahertz metamaterial devices", *Terahertz Physics, Devices, and Systems II*. SPIE, 2007, pp. 23-31. DOI: 10.1117/12.751613

[2] Ya. Yu, Yu-Sh. Lin, "Multi-functional terahertz metamaterial using symmetrical and asymmetrical electric split-ring resonator". *Results in Physics*. 2019, vol. 13, p. 102321. DOI: 10.1016/j.rinp.2019.102321

[3] Prinz, Ya. Victor, and Al, "Terahertz metamaterials and systems based on rolled-up 3D elements: designs, technological approaches, and properties", *Scientific reports*, 2017, vol. 7, P. 43334. DOI:/10.1038/srep43334

[4] W. Withayachumnankul, D. Abbott, "Metamaterials in the terahertz regime". *IEEE Photonics Journal*, 2009, vol. 1, No. 2, pp. 99-118. DOI:10.1109/JPHOT.2009.2026288

[5] Y D. K. Ntaikos, N. K. Bourgis and T. V. Yioultsis, "Metamaterial-Based Electrically Small Multiband Planar Monopole Antennas," *IEEE Antennas and Wireless Propagation Letters*, vol. 10, pp. 963-966, 2011. DOI:10.1109/LAWP.2011.2167309

[6] D. R. Smith, S. Schultz, P. Markoš, and C. M. Soukoulis, "Determination of effective permittivity and permeability of metamaterials from reflection and transmission coefficients," *Physical review B*, 2002, vol. 65, No. 19, p. 195104. DOI:10.1103/PhysRevB.65.195104

[7] T. Feng, F. Liu, W. Yim Tam and J. Li "Effective parameters retrieval for complex metamaterials with low symmetries," *Europhysics Letters,* 2013, vol. 102, No. 1, p. 18003.DOI: 10.1209/0295-5075/102/18003

[8] N. I. Landy, S. Sajuyigbe, J. J. Mock, D. R. Smith, and W. J. Padilla, "Perfect metamaterial absorber," *Physical review letters,* 2008, vol 100, No. 20, p. 207402. DOI: 10.1103/PhysRevLett.100.207402

[9] A. Singh, A. Raj, A. Gupta, A. Tiwari and P. Kumar, "Split ring resonator biosensor-an innovative design and analysis", *2020 IEEE 8th International Conference on Photonics (ICP)*, Kota Bharu, Malaysia, 2020, pp. 117-118. DOI:10.1109/ICP46580.2020.9206451

[10] L. La Spada, F. Bilotti, and L. Vegni, "Metamaterial biosensor for cancer detection," *SENSORS, 2011 IEEE*, Limerick, Ireland, 2011, pp. 627-630. DOI: 10.1109/ICSENS.2011.6127103

[11] F. Lan, F. Luo, P. Mazumder, Z. Yang, L. Meng, Z. Bao, J. Zhou, Y. Zhang, S. Liang, Z. Shi, AR. Khan, Z. Zhang, L. Wang, J. Yin, and H. Zeng, "Dual-band refractometric terahertz biosensing with intense wave-matter-overlap microfluidic channel," *Biomedical Optics Express*, 2019, vol. 10, No. 8. pp. 3789-3799. DOI: doi.org/10.1364/BOE.10.003789

[12] M. Y. Azab, M. F. O. Hameed, A. M. Nasr and S. S. A. Obayya, "Highly sensitive metamaterial biosensor for cancer early detection," *IEEE Sensors Journal*, 2021, vol. 21, No. 6, pp. 7748-7755. DOI:10.1109/JSEN.2021.3051075

[13] A. S. Saadeldin, M. F. O. Hameed, E. M. A. Elkaramany and S. S. A. Obayya, "Highly sensitive terahertz metamaterial sensor," *IEEE Sensors Journal*, 2019, vol. 19, No. 18, pp. 7993-7999. DOI: 10.1109/JSEN.2019.2918214

[14] M. M. Hassan, F. S. Sium, F. Islam, S. M. Choudhury, "A review on plasmonic and metamaterial based biosensing platforms for virus detection," *Sensing and Bio-Sensing Research*, 2021, vol. 33, p. 100429. DOI: 10.1016/j.sbsr.2021.100429

[15] N. Akter, M. M. Hasan, N. Pala, "A review of THz technologies for rapid sensing and detection of viruses including SARS-CoV-2," *Biosensors*, 2021, vol. 11, No. 10, p. 349. DOI: 10.3390/bios11100349

[16] J. T. Hong, S. W. Jun, S. H. Cha, J. Y. Park, S. Lee, G. A. Shin, and Y. H. Ahn, "Enhanced sensitivity in THz plasmonic sensors with silver nanowires. *Scientific reports*, 2018, vol. 8, No. 1, p.15536. DOI:10.1038/s41598-018-33617-2

[17] D. K. Lee, J. H. Kang, J. Kwon, J. S. Lee, S. Lee, D. H. Woo, J. H. Kim, C. S. Song, Q. H. Park and M. Seo, "Nano metamaterials for ultrasensitive Terahertz biosensing," *Scientific reports*, 2017, vol. 7, No.1, p. 8146. DOI: 10.1038/s41598-017-08508-7

[18] A. Kovačević, M. Potrebić, and D. Tošić, "Sensitivity characterization of multi-band THz metamaterial sensor for possible virus detection," *Electronics*, 2022, vol. 11, No. 5, p. 699. DOI:10.3390/electronics11050699

[19] C. Tan, S. Wang, H. Yang, Q. Huang, S. Li, X. Liu, H. Ye, G. Zhang, "Hydrogenated Boron Phosphide THz-Metamaterial-Based Biosensor for Diagnosing COVID-19: A DFT Coupled FEM Study," *Nanomaterials*, 2022, vol. 12, No. 22, p. 4024. DOI:10.3390/nano12224024

[20] A. Keshavarz and Z. Vafapour, "Sensing avian influenza viruses using terahertz metamaterial reflector," *IEEE Sensors Journal*, 2019, vol. 19, No. 13, pp. 5161-5166. DOI: 10.1109/JSEN.2019.2903731

[21] Cao, Y., Nallappan, K., Guerboukha, H., Gervais, T., & Skorobogatiy, M. (2019). Additive manufacturing of resonant fluidic sensors based on photonic bandgap waveguides for terahertz applications. *Optics Express*, *27*(20), pp. 27663-27681. DOI: 10.1364/OE.27.027663

[22] Nickpay, M. R., Danaie, M., & Shahzadi, A. (2022). Highly sensitive THz refractive index sensor based on folded split-ring metamaterial graphene resonators. *Plasmonics*, *17*(1), pp. 237-248. DOI:10.1007/s11468-021-01512-8

[23] Razani, A. N., Rezaei, P., Zamzam, P., Khatami, S. A., & Daraei, O. M. (2022). Absorption-based ultra-sensitive RI sensor based on the flower-shaped graphene resonator for early detection of cancer. *Optics Communications*, *524*, 128775. DOI:10.1016/j.optcom.2022.128775

[24] Tammam, M. M. E., Hameed, M. F. O., Elkaramany, E. M., Ali, T. A., & Obayya, S. S. A. (2025). Versatile terahertz metamaterial sensor for biomedical applications. *Plasmonics*, *20*(5), pp. 2815-2828. DOI:10.1007/s11468-024-02401-6

[25] Z. Hafdi, Z. Mezache, J. Tao, and G. Guergour, "Analysis of Graphene Pythagoras Tree Fractal Antenna with Thin SiO Substrate in Terahertz Regime," *Annals of West University of Timisoara-Physics*,2023, vol. 65, pp. 1-11. DOI:10.2478/awutp-2023-0001

[26] Z. Mezache, Z. Hafdi, J. Tao, "Design of a novel graphene buzzle metamaterial refractometer for sensing of cancerous cells in the terahertz regime," *Optik*, 2023, vol. 287, p. 171170. DOI:10.1016/j.ijleo.2023.171170

FinFET Based Computation Intensive Sub-Circuits Designs for Low Power VLSI Application

Shyamosree Goswami, Nadegouni Sandeep, Dara Sai Kumar, and Anup Dandapat

***Abstract*—In order to improve operational efficiency for low-power VLSI (Very Large Scale Integration) designs, the current research presents a simulation-based comparison of the results of basic gates, computation-intensive circuits, and basic memory blocks designed using FinFET technology. This creative designs in multipliers effectively consolidates input data by stacking blocks, which significantly reduces time in next-stage operations. To assess the suggested compressor design in terms of average power, delay, and Power Delay Product (PDP), extensive simulations and analyses are carried out. When conducted within the same technological and environmental conditions as existing designs, proposed designes demonstrate clear advantages. The proposed compressor shows an amazing 64.91% decrease in delay, a significant 87.85% improvement in average power consumption, and a notable 95.74% improvement in energy efficiency for proposed 4-3 compressor and similar outcomes for 5-3 compressor. In memory design, it also demonstrates a notable enhancement, achieving an 87.95% reduction in average power, a 49.57% decrease in delay, and an 87.57% improvement in Energy Delay Product (EDP) compared to both conventional NAND-based and FinFET-based Content Addressable Memory (CAM) designs.**

***Index Terms*—Compressors, CAM, FinFET, High speed, Multiplier, Stacking, Time delay.**

Original Research Paper
DOI: 10.53314/ELS2630021G

I. Introduction

MODERN semiconductor technology depends on VLSI (Very-Large-Scale Integration) architecture that consumes less power. This design is motivated by the growing demand for portable and battery-powered gadgets like smartphones, tablets, and wearable electronics. The main goal of low power VLSI design is to reduce power consumption while maintaining optimal performance and functionality. To achieve this goal, it is necessary to use a variety of methods at several levels of design, including architectural, circuit, and process levels. Memory elements and combinational circuits constitute fundamental components of VLSI systems, playing a pivotal role in the development of low-power computing devices. Memory elements, such as SRAM and DRAM, are indispensable for efficient data storage and retrieval, directly influencing power consumption and system performance. Combinational circuits, which execute logic operations without the need for data storage, are critical for performing arithmetic and logic functions with high efficiency and speed. The synergy between these elements ensures optimal data processing and minimizes energy expenditure, thereby enhancing the functionality and power efficiency of advanced VLSI systems. Their intricate design and operation are paramount in driving the evolution of energy-efficient computing technologies.

As semiconductor technology progresses towards lower nodes, the importance of low power VLSI design increases. This progression requires a thorough and all-encompassing design strategy that incorporates cutting-edge materials, inventive device structures, and superior power management methods. The goal is to achieve extended battery life, minimise heat generation, and improve the dependability of electronic systems.

At the manufacturing level, the use of sophisticated transistor technologies like FinFETs (Fin Field-Effect Transistors) has shown to be crucial in improving control over leakage currents [1]. These structures in three dimensions offer excellent control over the gate, which is crucial for maintaining low levels of leakage currents and allowing operation at lower supply voltages.

FinFET technology is employed in semiconductor devices for low-power applications because it offers several significant advantages compared to conventional planar transistors. The main factors that make FinFETs preferable for low-power applications are [1], [2]:

- **Improved Control Over Channel**
  1) FinFETs offer enhanced electrostatic control over the channel, resulting in a reduction of short-channel effects commonly observed in conventional planar transistors as device dimensions decrease.
  2) FinFETs have a three-dimensional structure that enables more precise control of the gate over the channel. This reduces leakage currents and enhances the switching performance of the transistor.
- **Lower Leakage Currents**
  1) Subthreshold Leakage: FinFETs exhibit considerably reduced subthreshold leakage currents in comparison to planar transistors. The reason for this is that the gate completely encloses the channel on three sides, resulting in enhanced control and less leakage.
  2) Gate-Induced Drain Leakage (GIDL) is reduced in FinFETs due to increased gate control, resulting in

Manuscript received on January 31st, 2025. Received in revised form on September 22nd, 2025. Accepted for publication on October 30th, 2025.

Shyamosree Goswami (e-mail: shyamosreegoswami@gmail.com, ORCID: 0009-0002-5498-1740), Nadegouni Sandeep (e-mail: sandeepnadegouni7282@gmail.com, ORCID: 0009-0008-9167-0865), Dara Sai Kumar (e-mail: saikumardhara923@gmail.com, ORCID: 0009-0003-9113-9269) and Anup Dandapat (e-mail: anup.dandapat@gmail.com, ORCID: 0000-0002-0997-1220) are with the Department of Electronics and Communication Engineering, National Institute of Technology Meghalaya, Sohra 793108, India.

decreased power usage.

- **Lower Supply Voltage**
  1) FinFETs exhibit superior electrostatic control, enabling them to function efficiently at reduced supply voltages. This characteristic leads to a significant decrease in power consumption, as dynamic power consumption is directly proportional to the square of the supply voltage.
- **Scalability**
  1) FinFET technology allows for continued scaling of transistors beyond the limits of planar technology, enabling more transistors to be packed into the same area without significantly increasing power consumption.

This study involved doing extensive simulations of all basic logic gates and other combinational circuits using FinFET technology. The simulations were compared to equivalent designs using standard CMOS technology to assess performance parameters and power efficiency. In addition, we have thoroughly analyzed the performance of FinFETs at the 20 nm technology node, specifically studying their electrical properties and operational benefits compared to conventional planar transistors.

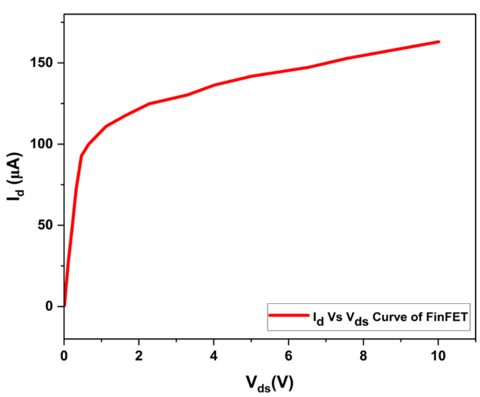

(a) I_d vs V_{ds} curve of FinFET

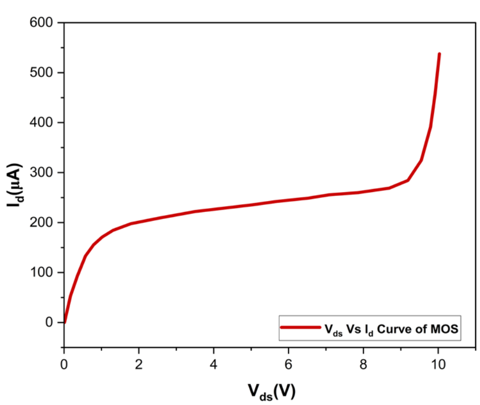

(b) I_d vs V_{ds} curve of MOSFET

Fig. 1. Characteristics Curve of CMOS and FinFET.

The inquiry entailed the analysis of crucial delay, power dissipation, and overall circuit reliability. Fig. 1 shows the characteristics curve of CMOS and FinFET. We conducted a thorough comparison of FinFET and CMOS technologies by modelling fundamental logic gates including AND, OR, NOT, NAND, and NOR, as well as complex combinational devices such as multiplexers and adders. This work emphasises the influence of FinFET's three-dimensional configuration on improving gate control and mitigating short-channel effects, which are significant obstacles in sub-20 nm CMOS technology. The paper is organised as the basic of FinFET is described in Section II, Section III presents the related works, Section IV presents the simulated results and Section V discusses the conclusion.

II. Overview of FinFET Technology

A FinFET is a "fin" field-effect transistor (FET). It is a metal-oxide-semiconductor (MOS) device where the gate is placed on two sides of a thin vertical semiconductor body standing on a substrate as shown in Fig. 2. FinFETs, known as Multigate Field Effect Transistor (MGFET), are predicted to be one of the best promising devices to substitute bulk MOSFET due to its improved SS (Subthreshold Swing) slope, better stability, higher (I_{on}/I_{off}) ratio, better short channel performance, smaller intrinsic gate capacitance. Here is the main structure of MOSFET and FinFET gate [3].

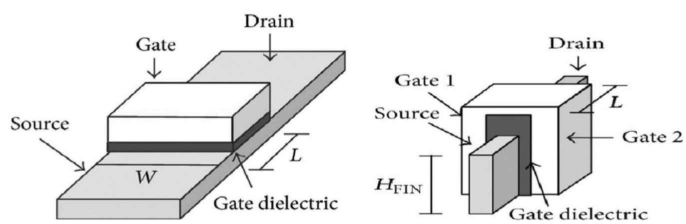

Fig. 2. Basic Structure of conventional CMOS and FinFET.

A. Characteristics of a FinFET

The I-V (current-voltage) behavior of FinFETs closely resembles that of conventional MOSFETs but exhibits several unique traits.

- Threshold Voltage (V_{th}): In FinFETs, the threshold voltage refers to the gate voltage level at which the device begins to allow current flow. Owing to better gate control over the channel, this voltage is generally lower compared to that of traditional MOSFETs [3].
- Drain-Source Current (I_{ds}): This indicates the current flowing between the drain and source terminals. It is influenced by both the gate-to-source voltage (V_{gs}) and the drain-to-source voltage (V_{ds}). As V_{gs} rises, I_{ds} also increases, eventually entering a saturation phase where further increase in V_{gs} results in minimal change in I_{ds} [3].

After observing both the plots in Fig. 1 we can observe that in CMOS after reaching certain voltage with increase in V_{DS} continuously a breakdown has occurred due to the SCE which can be minimized in FinFET based designs. The finFET parameters of 20nm model is shown in Table I [1].

TABLE I
PARAMETERS OF FINFET [4]

FinFET parameters	Technology (nm)	V_{DD}(V)	Leff (nm)	hfin (nm)	tfin (nm)	toxide (nm)
Value	20	0.9	24	28	15	0.9

III. RELATED WORKS

There are several methods for achieving low power design in VLSI systems, each targeting different aspects of the design process to minimize energy consumption while maintaining performance. Power gating is a widely used technique that reduces leakage power by turning off the power supply to inactive modules, Dynamic voltage and frequency scaling (DVFS) adjusts the voltage and frequency according to the workload, Multi-threshold CMOS (MTCMOS) technology employs transistors with different threshold voltages within the same design, balancing speed and power efficiency by using low-threshold transistors for critical paths and high-threshold transistors for non-critical paths to reduce leakage.the use of advanced transistor technologies like FinFETs enhances control over leakage currents and allows for operation at lower voltages, further contributing to power savings. The basic gates can be implemented using the FinFET technology for better performance over MOS design. Again multiplication, an intricate and time-intensive arithmetic operation, plays a pivotal role in numerous signal processing algorithms [5]–[8]. Recognizing its significance, the multiplication process is systematically delineated into three key stages: the generation of partial products, the subsequent reduction of these partial products, and the ultimate computation of the resultant product [3], [6], [7], [9], [10]. The exploration of various methodologies for optimization at each stage has become a focal point of extensive research. This includes innovative compressor designs and the introduction of time-efficient structures [11]–[16].

A content addressable memory (CAM) utilizes specialized comparison logic to perform table lookup operations within a single clock cycle [17]–[19]. CAMs are widely used in applications that demand high-speed search capabilities. In this work, the study and analysis of various CAM architectures are centered around comparison circuits based on N-type, P-type, and Transmission Gate (TG) configurations [20]–[22]. The DLPCAM design [23] proposed a TCAM memory cell using FinFET technology and evaluated key parameters such as search delay, average power consumption, and energy usage in a 32-nm process. On the other hand, PVECAM investigated the impact of process variations on FinFET-based CAMs using a 20-nm HSPICE model [24].

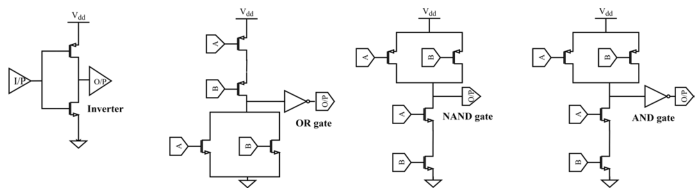

Fig. 3. Schematics of basic gates.

IV. COMPUTATION INTENSIVE CIRCUIT DESIGN AND SIMULATION

A. *Logic gates Design using FinFET*

In this work we have designed basic gates, inverter as shown in Fig. 3 and few combination circuits like compressor, Multiplier using FinFET and compare their average power consumption and Delay for all the designs.

The comparison Table II clearly shows that FinFET-based designs outperform CMOS-based designs. For low-power design, using FinFETs represents a significant advancement. FinFETs can be used in lower technology nodes without being affected by short channel effects, making them more area-efficient as well.

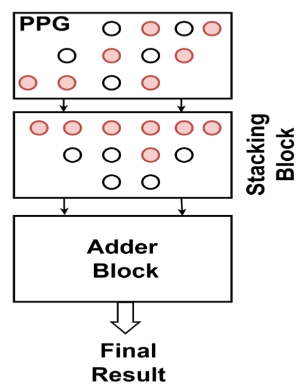

Fig. 4. Architecture of compressor circuit.

B. *Compressor Design using FinFET*

Compressors are basically internal components of multipliers. In the context of digital circuit design, compressors are specialized circuits used within multipliers to efficiently reduce and process partial products during multiplication operations. These compressors help optimize the overall speed and efficiency of the multiplication process by reducing the critical path delay, which is essential for high-performance applications. Compressors play a vital role in handling binary data and are integral to the internal architecture of multipliers. Their effective implementation is crucial for achieving fast and accurate multiplication in various digital systems.

Over the last two decades, research has focused on the use of various compressors for partial product reduction. Examples include the 3-2, 4-2, 5-2, and 5-3 compressors. Nonetheless, it is important to note that these compressors perform best when the multiplier size is minimal. Larger multipliers, like 16×16 and 32×32 bit combinations, require huge compressor

TABLE II
COMPARISON RESULT OF LOGIC GATE USING FINFET AND TRADITIONAL CMOS

	INVERTER		NAND		AND		OR	
	FinFET	Traditional	FinFET	Traditional	FinFET	Traditional	FinFET	Traditional
DELAY(ps)	1.122	3.270	1.549	7.490	4.804	19.18	4.828	20.020
POWER (nW)	9.992	69.83	22.88	58.14	29.55	134.82	39.53	102.06

sizes. In this setting, high-order compressors appear as a feasible option, providing greater power efficiency and speed. However, it is important to remember that using high-order compressors has trade-offs because their implementation takes up more silicon area than their low-order counterparts. The complex trade-offs between power, speed, and performance efficiency highlight the subtle difficulties in fine-tuning the partial product reduction phase of large-scale multipliers.

In this paper, we provide a novel stacked-based compressor in which a specific stacking step is used to sort partial product data. In this phase, ones (1s) in a column are systematically moved to the Most Significant Bits (MSBs), and zeros (0s) are simultaneously moved to the Least Significant Bits (LSBs). We have created two compressor designs in the proposed design: a 4:3 and a 5:3 compressor block diagram shown in Figs. 4 and 5. Multipliers make heavy use of both designs. In order to make the design process easier, we have purposefully divided the entire circuit into a well-organized set of separate functional components. Within this structure, two essential blocks are carefully defined:

- **Stacking Block:** Data compression takes on a new dimension when stacking blocks are incorporated into multiplier design. Here, a stacking block combines the input data by piling up the number of 1s without taking into account their particular place values. For instance, the stacking block output, given the input "1010," combines into "1100," which represents the count of 1s.
  In the proposed design, two different stacks a 4-bit stack for the 4:3 compressor and a 5-bit stack for the 5:3 compressor are integrated, each specifically designed for a different compressor. These stacking blocks are essential to the compression process since they maximise data representation for multiplier stages that come after. When we examine the details of this design, one important aspect that stands out as being able to improve performance and efficiency in multiplication operations is the use of two stacks that are specifically designed for separate compressors. We implemented the circuit based on the Boolean equation we derived for proposed design of the 4:3 and 5:3 compressor stack blocks.
  Let's consider the inputs to be a_0, a_1, a_2, a_3 and respective outputs be b_1, b_2, b_3, b_4.

$$b_1 = a_0 + a_1 + a_2 + a_3 \tag{1}$$
$$b_2 = a_0(a_2 + a_3) + a_1(a_0 + a_2) + a_3(a_1 + a_2) \tag{2}$$
$$b_3 = a_3(a_0a_2 + a_1a_2 + a_0a_1) + a_0a_1a_2 \tag{3}$$
$$b_4 = a_0a_1a_2a_3 \tag{4}$$

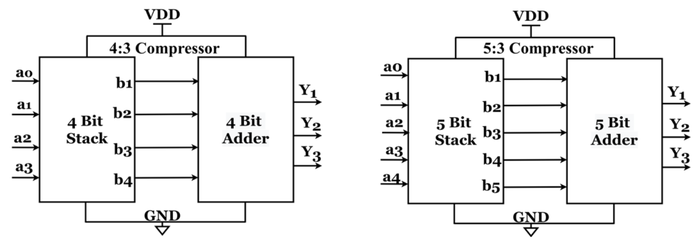

Fig. 5. Block diagram of Compressor.

Similar to the 4:3 compressor stack block, we have derived the boolean expression of the 5-bit stack for the proposed design.

$$b_1 = a_0 + a_1 + a_2 + a_3 + a_4 \tag{5}$$
$$b_2 = (a_0a_1) + (a_0a_2) + (a_0a_3) + (a_0a_4) + (a_1a_2) + (a_1a_3) + (a_1a_4) + (a_2a_3) + (a_2a_4) + (a_3a_4) \tag{6}$$
$$b_3 = P_1 + P_2 + P_3 + P_4 + P_5 + P_6 + P_7 + P_8 + P_9 + P_{10} \tag{7}$$

where

$$P_1 = a_0(a_1a_2), \quad P_2 = a_0(a_1a_3), \quad P_3 = a_0(a_1a_4),$$
$$P_4 = a_0(a_2a_3), \quad P_5 = a_0(a_2a_4), \quad P_6 = a_0(a_3a_4),$$
$$P_7 = a_1(a_2a_3), \quad P_8 = a_1(a_2a_4), \quad P_9 = a_1(a_3a_4),$$
$$P_{10} = a_2(a_3a_4)$$
$$b_4 = P_{11} + P_{12} + P_{13} + P_{14} + P_{15} \tag{8}$$

where

$$P_{11} = (a_0P_7), \quad P_{12} = (a_0P_8), \quad P_{13} = (a_0P_9),$$
$$P_{14} = (a_0P_{10}), \quad P_{15} = (a_1P_{10})$$
$$b_5 = a_0a_1a_2a_3a_4 \tag{9}$$

It is clear that several AND operations are being carried out from equations (1) to (9). The repetition of several AND blocks, which allows us to extract outputs from previously computed results, is a remarkable observation. This discovery offers a chance to reduce circuits because we can make the process more efficient by using previous findings. The stack block's output then plays a crucial role in calculating the summation for the next step, demonstrating a clever use of previously acquired data in the circuit.

- **Adder Block:**The adder block, which produces the compression process's end result, is the next part of the

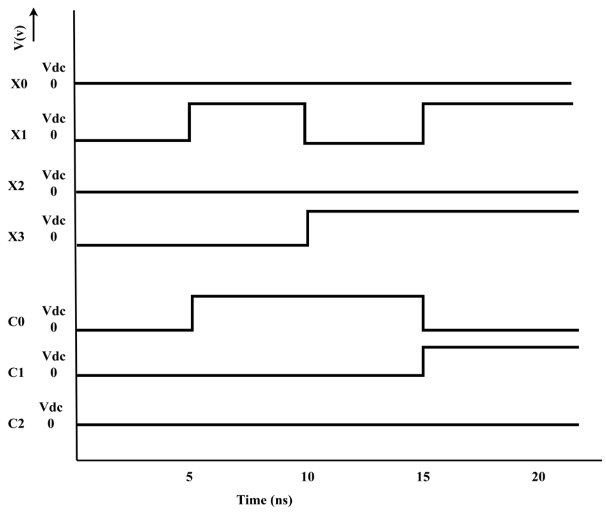

(a) 4:3 compressor output graph

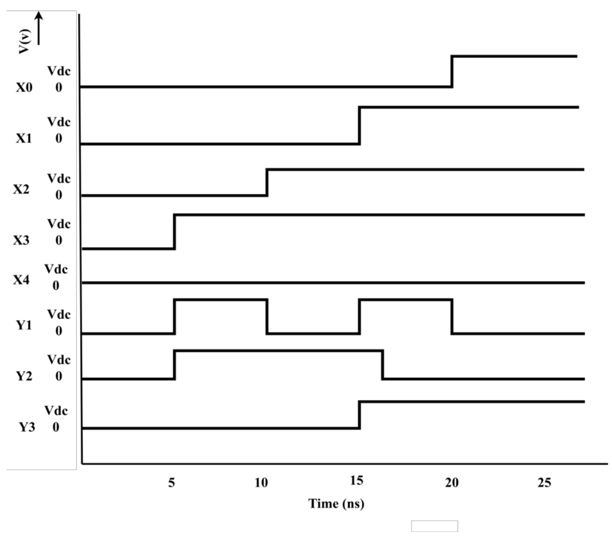

(b) 5:3 compressor output graph

Fig. 6. Output characteristics of the proposed compressors.

compressor. We assess the input conditions to this block in proposed design strategy rather than employing a half adder or full adder right away. Proposed method takes advantage of the fact that the inputs are already sorted after going through the stacking block. Because of its intrinsic orderliness, the computation of the result is made easier because there is less chance that the least significant bits (LSB) contain 1s. Taking use of this feature, the approach determines the output expression by applying Boolean expression analysis to the input conditions. These phrases are rigorously verified against every possible combination to guarantee that the result is accurate in every scenario. This thorough validation ensures that the design is resilient and reliable and shows that it is effective in generating accurate results for a range of input scenarios.

Let the final results for the 4 bit adder be Y_1, Y_2, Y_3 and

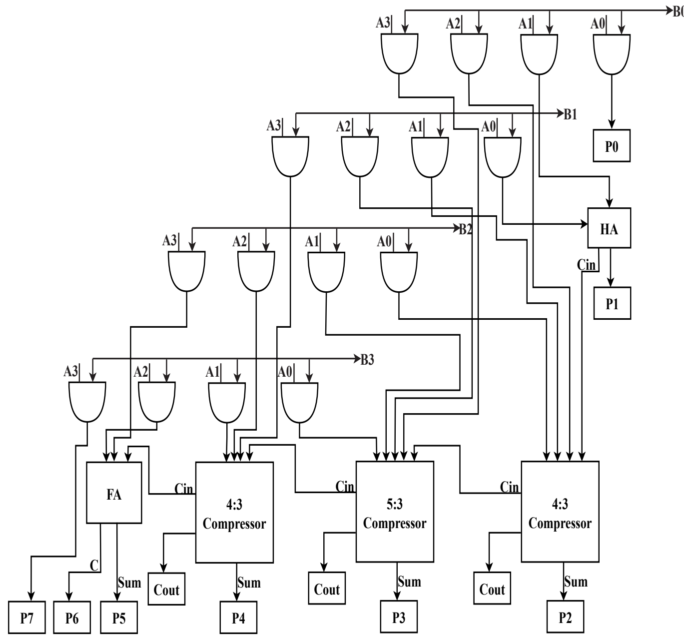

Fig. 7. Block diagram of Multiplier.

the inputs be b_1, b_2, b_3, b_4.

$$Y_1 = b_1 b_2' + b_3 b_4' \tag{10}$$
$$Y_2 = b_2 b_3' + b_3 b_4' \tag{11}$$
$$Y_3 = b_1 b_2 b_3 b_4 \tag{12}$$

Similar way, we derived the expression for the 5-bit adder:

$$Y_1 = b_1 b_2' + b_3 b_4' + b_5 \tag{13}$$
$$Y_2 = b_2 b_3' + b_3 b_4' \tag{14}$$
$$Y_3 = b_4 b_5' + b_5 \tag{15}$$

We can see that the number of computing blocks (AND, OR) required for this adding block is less than the conventional 4-bit adder and 5-bit adder. The output graphs of both compressors are shown in Fig. 6, and the performance comparison is tabulated in Table III.

TABLE III
COMPARISON OF POWER, DELAY, AND PDP FOR 4-3 AND 5-3 COMPRESSORS

Design	Type	Power	Delay	PDP
4-3 Compressor	Conventional	4.28 μW	92.2 ps	394.62 aJ
4-3 Compressor	Proposed	0.52 μW	32.35 ps	16.82 aJ
5-3 Compressor	Conventional	6.58 μW	303 ps	1.9 fJ
5-3 Compressor	Proposed	1.12 μW	72.3 ps	80.98 aJ

1) Application of Compressor: In the proposed multiplier design as shown in Fig. 7, we have implemented the proposed compressor instead of the conventional method, which

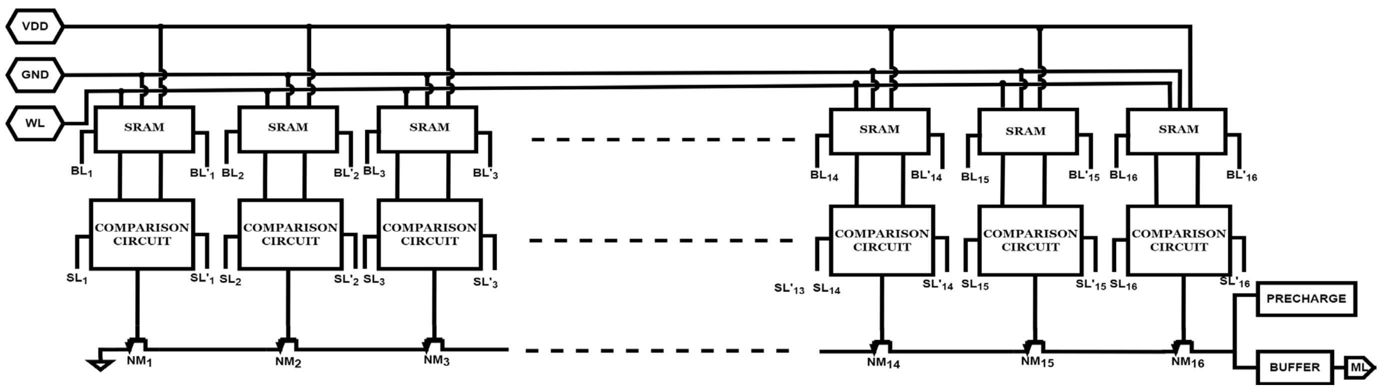

Fig. 8. 16 Bit CAM Array Block Design.

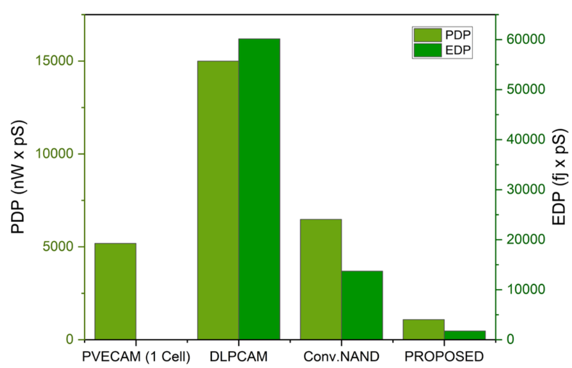

(a) PDP vs EDP comparison

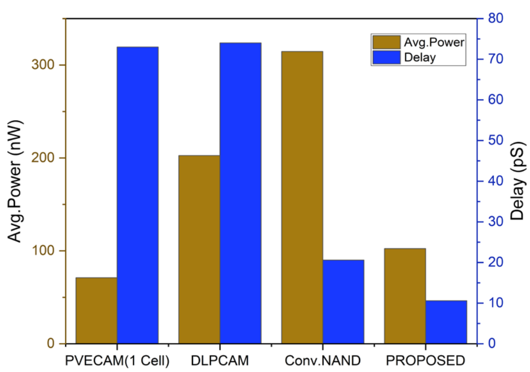

(b) Power vs Delay comparison

Fig. 9. Performance analysis of proposed CAM design.

employs half adders (HA) and full adders (FA) for partial product addition across multiple stages. By integrating the proposed compressor, we significantly reduce the number of addition stages required. This reduction not only minimizes power consumption but also substantially decreases the overall delay. Consequently, the approach demonstrates a marked improvement in efficiency and performance over traditional multiplier designs as tabulated in Table IV.

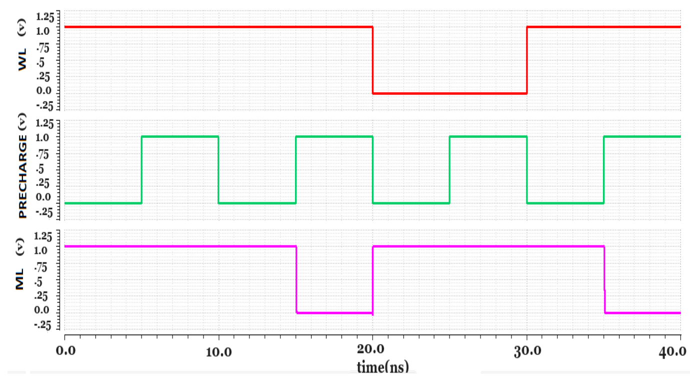

Fig. 10. Timing diagram of 16-bit CAM array using FinFET.

TABLE IV
COMPARISON TABLE OF MULTIPLIER

Design	Technology	Voltage	Power (μW)	Delay	PDP
Proposed	FinFET	0.9V	389	337.83ps	0.13pJ
Conv.	CMOS	0.9V	695.59	8.380ns	5.82pJ

TABLE V
PERFORMANCE OF 1 × 16 ARRAY

	DLPCAM [23]	Conv.NAND (MOSFET)	Proposed (FinFET)
Avg.Power (nW)	202.63	850	102.40
Delay(ps)	74.01	21	10.60
PDP($nW \times ps$)	14997.14	17850	1085.44
Energy (fJ)	813	666	164
EDP($fJ \times ps$)	60170.13	13986	1738

From the comparison table, it can be concluded that the utilization of a FinFET-based compressor, as opposed to traditional FA and HA, results in a reduced PDP. This FinFET-based approach is more efficient in terms of delay, which is particularly significant given that multipliers are fundamental components of arithmetic and logical units where speed is a critical factor. Thus, the implementation of FinFET-based compressors enhances the overall performance and efficiency of these operations.

C. Basic CAM Memory Design Using FinFET

CAM, also called associative memory, is a unique kind of memory that is used to search through the data contained inside. Traditional CAM designs use large and active parallel hardware, which leads to high dynamic power usage. With the move to smaller technology nodes and the shift from planar MOSFETs to multi-gate devices, new design trade-offs are expected in CAMs. FinFET technology helps reduce short channel effects at these smaller scales. In this work, we present a simple 16-bit NAND-type CAM cell shown in Fig. 8 built using FinFETs and evaluate its performance, focusing mainly on average power consumption and delay shown in Fig. 9. Fig. 10 shows the timing diagram of a 16-bit CAM array using FinFET. We have simulated the CAM design and compared it with existing designs available and tabulated the values as tabulated in Tables V and VI.

TABLE VI
PER BIT CAM CELLS PERFORMANCE

	PVECAM (1CELL) [24]	Conv.NAND (MOSFET)	Proposed (FinFET)
Avg.Power (nW)	70.89	53.13	15.69
Delay(ps)	72.56	10.10	3.50
PDP($nW \times ps$)	5143.77	536.61	54.91

V. CONCLUSION

In conclusion, the analysis of the sub-circuits, which includes FinFET based designs like basic gates, shows improved performance as compared to MOS based designs in terms of power and delay.The stack-based digital compressors and unique adder blocks, showed encouraging results across multiple performance parameters. The simulations and analyses indicate that the proposed concept outperforms previous designs significantly. Specifically, the results show an average power usage improvement of 87.85% for the 4-3 configuration and 82.98% for the 5-3 configuration. Additionally, there is a delay reduction of 64.91% for the 4-3 configuration and 76.14% for the 5-3 configuration. Furthermore, the Power Delay Product (PDP) decreased by 95.74% for the 4-3 configuration and 94.97% for the 5-3 configuration. Proposed design successfully balances power efficiency, speed, and performance, making it a promising leap in multiplier architectures.

Detailed analysis revealed that incorporating FinFET technology into CAM design led to enhanced performance when compared to conventional MOSFET-based CAMs. The design achieved noticeable improvements, reducing average power consumption by 87.95%, delay by 49.57%, and Energy Delay Product (EDP) by 87.57% compared to both traditional NAND-based and earlier FinFET-based CAM implementations [24].

REFERENCES

[1] M. Masahara, T. Matsukawa, K. Endo, Y.-X. Liu, W. Mizubayashi, S. Migita, S. O'uchi, H. Ota, and Y. Morita, "Advanced finfet process technology for 20 nm node and beyond," in *Proc. IEEE Int. NanoElectronics Conf.*, pp. 1–2, 2011. doi: 10.1109/INEC.2011.5991771.

[2] R. K. Maurya and B. Bhowmick, "Review of finfet devices and perspective on circuit design challenges," *Silicon*, vol. 14, no. 11, pp. 5783–5791, 2022. doi:10.1007/s12633-021-01366-z.

[3] S. Goswami, A. Kumar, and A. Dandapat, "Design of a stack based compressor for high speed computation," in *2024 IEEE 9th International Conference for Convergence in Technology (I2CT)*, pp. 1–5, IEEE, 2024. doi:10.1109/I2CT61223.2024.10544000.

[4] S. Goswami, K. H. Varma, R. Gudla, and A. Dandapat, "Cascam: Comparative analysis of search operation of finfet-and mosfet-based content-addressable memory," in *International Symposium on Sustainable Energy and Technological Advancements*, pp. 423–433, Springer, 2024. $doi: 10.1007/978-981-97-7018-2_30$.

[5] A. Fathi, B. Mashoufi, and S. Azizian, "Very fast, high-performance 5-2 and 7-2 compressors in cmos process for rapid parallel accumulations," *IEEE Transactions on Very Large Scale Integration (VLSI) Systems*, vol. 28, no. 6, pp. 1403–1412, 2020. doi:10.1109/TVLSI.2020.2983458.

[6] S. Venkatachalam and S.-B. Ko, "Design of power and area efficient approximate multipliers," *IEEE Transactions on Very Large Scale Integration (VLSI) Systems*, vol. 25, no. 5, pp. 1782–1786, 2017. doi:10.1109/TVLSI.2016.2643639.

[7] W. Guo and S. Li, "Fast binary counters and compressors generated by sorting network," *IEEE Transactions on very large scale integration (VLSI) systems*, vol. 29, no. 6, pp. 1220–1230, 2021. doi:10.1109/TVLSI.2021.3067010.

[8] M. Ha and S. Lee, "Multipliers with approximate 4–2 compressors and error recovery modules," *IEEE Embedded Systems Letters*, vol. 10, no. 1, pp. 6–9, 2017. doi:10.1109/LES.2017.2746084.

[9] R. Marimuthu, Y. E. Rezinold, and P. S. Mallick, "Design and analysis of multiplier using approximate 15-4 compressor," *IEEE Access*, vol. 5, pp. 1027–1036, 2016. doi:10.1109/ACCESS.2016.2636128.

[10] A. Dandapat, S. Ghosal, P. Sarkar, and D. Mukhopadhyay, "A 1.2-ns16× 16-bit binary multiplier using high speed compressors," *International Journal of Electrical and Electronics Engineering*, vol. 4, no. 3, pp. 234–239, 2010.

[11] A. Momeni, J. Han, P. Montuschi, and F. Lombardi, "Design and analysis of approximate compressors for multiplication," *IEEE Transactions on Computers*, vol. 64, no. 4, pp. 984–994, 2014. doi:10.1109/TC.2014.2308214.

[12] K. M. Reddy, M. H. Vasantha, Y. N. Kumar, and D. Dwivedi, "Design of approximate booth squarer for error-tolerant computing," *IEEE Transactions on Very Large Scale Integration (VLSI) Systems*, vol. 28, no. 5, pp. 1230–1241, 2020. doi:10.1109/TVLSI.2020.2976131.

[13] C. Fritz and A. T. Fam, "Fast binary counters based on symmetric stacking," *IEEE Transactions on Very Large Scale Integration (VLSI) Systems*, vol. 25, no. 10, pp. 2971–2975, 2017. doi:10.1109/TVLSI.2017.2723475.

[14] T. Satish and K. S. Pande, "Multiplier using nand based compressors," in *2019 3rd International Conference on Electronics, Materials Engineering & Nano-Technology (IEMENTech)*, pp. 1–6, IEEE, 2019. doi:10.1109/IEMENTech48150.2019.8981067.

[15] C. S. Wallace, "A suggestion for a fast multiplier," *IEEE Transactions on Electronic Computers*, vol. EC-13, no. 1, pp. 14–17, 1964. doi:10.1109/PGEC.1964.263830.

[16] X. Yi, H. Pei, Z. Zhang, H. Zhou, and Y. He, "Design of an energy-efficient approximate compressor for error-resilient multiplications," in *2019 IEEE International Symposium on Circuits and Systems (ISCAS)*, pp. 1–5, IEEE, 2019. doi:10.1109/ISCAS.2019.8702199.

[17] L. Chisvin and R. J. Duckworth, "Content-addressable and associative memory: Alternatives to the ubiquitous ram," *Computer*, vol. 22, no. 7, pp. 51–64, 1989. doi:10.1109/2.30732.

[18] K. Pagiamtzis and A. Sheikholeslami, “A low-power content-addressable memory (cam) using pipelined hierarchical search scheme,” *IEEE Journal of Solid-State Circuits*, vol. 39, no. 9, pp. 1512–1519, 2004. doi:10.1109/JSSC.2004.831433.

[19] C. A. Zukowski and S.-Y. Wang, “Use of selective precharge for low-power content-addressable memories,” in *1997 IEEE International Symposium on Circuits and Systems (ISCAS)*, vol. 3, pp. 1788–1791, IEEE, 1997. doi:10.1109/ISCAS.1997.621492.

[20] S. Kumar, A. Noor, B. K. Kaushik, and B. Kumar, “Design of ternary content addressable memory (tcam) with 180 nm,” in *2011 International Conference on Devices and Communications (ICDeCom)*, pp. 1–5, IEEE, 2011. doi:10.1109/ICDECOM.2011.5738528.

[21] T. V. Mahendra, S. W. Hussain, S. Mishra, and A. Dandapat, “Performance analysis of n-cam, p-cam and tg-cam using 45-nm technology,” in *2019 International Conference on Intelligent Computing and Control Systems (ICCS)*, pp. 621–625, IEEE, 2019. doi:10.1109/ICCS45141.2019.9065404.

[22] T. V. Mahendra, S. W. Hussain, S. Mishra, and A. Dandapat, “Low match-line voltage swing technique for content addressable memory,” in *2019 7th International Conference on Smart Computing & Communications (ICSCC)*, pp. 1–5, IEEE, 2019. doi:10.1109/ICSCC.2019.8843590.

[23] M.-C. Chang and K.-L. He, “Design of low-power finfet-based tcams with unevenly-segmented matchlines for routing table applications,” in *2015 IEEE 11th International Conference on ASIC (ASICON)*, pp. 1–4, IEEE, 2015. doi:10.1109/ASICON.2015.7517182.

[24] M. Arulvani, M. M. Ismail, and R. M. Issakki, “Process variation effects on finfet based content addressable memory,” in *2017 International Conference on Communication and Signal Processing (ICCSP)*, pp. 2106–2110, IEEE, 2017. doi:10.1109/ICCSP.2017.8286776.

Compact UWB Pi-Slotted Elliptical Patch Antenna for Terahertz Applications

Sulaiman Bin Helal and Abu Zafor Md. Touhidul Islam

***Abstract*—Antennas offering wide bandwidth, high gain and efficiency are essential to terahertz (THz) wireless communication systems and has gathered significant attention in antenna research. This paper introduces a compact, high-gain, ultra-wideband (UWB) microstrip patch antenna tailored for THz applications, along with its performance analysis. The proposed antenna has an elliptical patch with a pi shaped slot and is excited by a tapered feedline. An elliptical patch antenna incorporating a pi-shaped slot is introduced for the first time in the terahertz THz spectral region, demonstrating the ability to simultaneously achieve substantial size miniaturization, wideband performance, improved impedance matching, and enhanced gain. The antenna structure was designed and optimized for improved performance using CST Microwave Studio (MWS) version 2018. A Rogers RT/duroid 5880 substrate was used for antenna design, featuring 6 µm thickness, 2.2 relative permittivity, 0.0009 loss tangent, and 120 × 80 µm² planar dimensions. The proposed antenna demonstrates strong performance characteristics with a wide impedance bandwidth of 3.41 THz (5.01–8.42 THz), high gain of 7.906 dB, radiation efficiency of 77.83%, and low return loss of −43.57 dB, with consistent VSWR across the entire frequency range. The surface current distribution as well as the input impedance of the pi-shaped slotted antenna are also favorable. All the simulation results suggest that the proposed small size pi-shaped slotted elliptical patch antenna can be a suitable candidate for high-speed 6G wireless communication applications in the THz band.**

***Index Terms*—Elliptical patch, microstrip antenna, pi shaped slot, tapered feedline, terahertz band, wideband, wireless applications, 6G communication.**

Original Research Paper
DOI: 10.53314/ELS2630029S

I. Introduction

OVER the past few decades, bandwidth requirements for wireless communications have increased rapidly. Although advanced modulation techniques have been employed to enhance spectral efficiency [1], the channel capacity is ultimately limited by Shannon's formula, even with MIMO implementations. Consequently, accessing higher carrier frequency bands like terahertz (THz) spectrum (0.1 to 10 THz) is essential to meet the required transmission capacity. Owing to the unique advantages like broadband capability, secure, more directional, smaller scintillation effects, low attenuation, and low energy consumption, THz technology has been applied in the field of communication, defense, biomedical imaging, spectroscopy, and radio astronomy [2], [3]. Research in THz technology has grown recently, driven by the availability of THz sources and progress in laser, semiconductor, and photoconductive technologies [4]. THz antenna design suffers from severe signal attenuation, fabrication challenges associated with microscopic dimensions, and significant material losses. Antennas functioning within the THz band must demonstrate high gain, wide bandwidth, high directive and minimal signal losses to ensure robust and efficient communication [5], [6].

Patch antennas have attracted considerable attention as a promising solution for THz applications owing to their compact dimensions, ease of fabrication, and compatibility with integrated circuit technology. A dual-band reconfigurable graphene-based antenna detailed in [7] achieved a bandwidth of 50 GHz with a gain of 4.01 dB. Photonic band gaps and defective ground structures were utilized in [8], which leads to a gain increase to 6.93 dB. But it suffers from narrow bandwidth and size limitations. A miniaturized graphene-based THz patch antenna proposed in [9] obtained a high return loss of −57.54 dB and a bandwidth of 199.6 GHz, though its gain was limited to 2.76 dB. An asymmetric coplanar waveguide-fed patch antenna was developed in [10], which offered a gain of 6.14 dB and a compact design but with a narrower bandwidth of 92 GHz. Moulfi et al. developed a wideband nano circular graphene-printed antenna for terahertz transmission, employing a Defected Ground Structure (DGS) technique to enhance bandwidth and conducted a parametric study [11]. Khan et al. proposed a circular THz patch antenna and investigated variations in substrate shapes and materials [12]. Abohmra et al. examined the characteristics of graphene at terahertz frequencies through a rectangular antenna designed for wearable applications [13]. Fakharian introduced a multifunctional graphene-based THz antenna [14], while Badr and Moradi presented a novel hexagonal dual-band antenna operating at 2.14 THz and 5.41 THz [15]. Nissiyah and Madhan explored graphene-based patch antennas capable of supporting triple and quad-band operations in the terahertz range [16].

Manuscript received on November 7th, 2025. Received in revised form on February 18th and March 18th, 2026. Accepted for publication on March 30th, 2026.

Sulaiman Bin Helal is with the Antenna Design Lab, Department of Electrical and Electronic Engineering, University of Rajshahi, Rajshahi 6205, Bangladesh (e-mail: mdsulaiman113504@gmail.com, ORCiD: 0009-0009-7451-8842).

Abu Zafor Md. Touhidul Islam is with the Antenna Design Lab, Department of Electrical and Electronic Engineering, University of Rajshahi, Rajshahi 6205, Bangladesh (e-mail: touhid.eee@ru.ac.bd, ORCiD: 0009-0002-0375-4660).

Although numerous THz antennas have been proposed, most suffer from either large physical dimensions or limitations in bandwidth, gain, and efficiency. These shortcomings pose significant challenges for practical THz system implementation [17]. Thus, further investigation into patch antenna structures is essential to achieve improved performance. This study presents the design and performance analysis of a compact, high-performance pi-slotted elliptical patch antenna tailored for THz-band 6G communication systems. Elliptical geometries provide efficient current distribution, reduced surface-wave losses, minimized cross-polarization levels, broader impedance bandwidth, and the potential for enhanced gain and directivity [18]. Incorporating slots into the design can further improve impedance matching and radiation efficiency, which are critical for effective 6G communication [17], [19]. A pi-shaped slotted microstrip patch antenna is considered superior for modern wireless communication due to its ability to enhance performance metrics simultaneously, such as achieving wide impedance bandwidth, high gain, high efficiency, and compact size. The pi-slot geometry acts as a reactive loading technique that alters the surface current distribution, improving impedance matching and enabling multi-frequency operation. The novelty of employing a pi-shaped slot in elliptical patch antenna design lies in its first introduction within the THz spectral region, where it demonstrates the capacity to simultaneously achieve substantial size miniaturization, wideband or multi-band performance, improved impedance matching, and gain.

The rest of the paper is arranged as follows. The antenna design approach is discussed in Section II. Section III presents the simulation results and performance analysis of the proposed antenna. A comparison of the proposed antenna's performance with previously reported designs is given in Section IV. Finally, key findings of the research are listed in Section V.

II. Proposed Antenna Design

The proposed antenna has been designed and simulated using CST Studio Suite 2018. An elliptical patch with a pi-slot, a full ground, and a 50 Ω feedline are incorporated in the proposed pi-shaped slotted elliptical patch antenna. The feedline is tapered from a wider base to a narrower tip used for better impedance matching. Fig. 1 shows the front-facing view and pi-slot structure of the proposed THz antenna. The substrate material used is Rogers RT/duroid 5880, with a relative permittivity (εr) of 2.2 a loss tangent (tan δ) of 0.0009. A substrate of 6 μm thickness is used, and the patch, full ground, and feedline structure are fabricated from annealed copper with a thickness of 0.035 mm. This design methodology reflects a hybrid approach combining: Geometric shaping of radiating Element (elliptical patch) for smooth current distribution and broad radiation characteristics, Slot loading (Pi-shaped slot) enables multi-resonance tuning, broader bandwidth and higher radiation efficiency, Parametric control for fine-tuning of performance metrics.

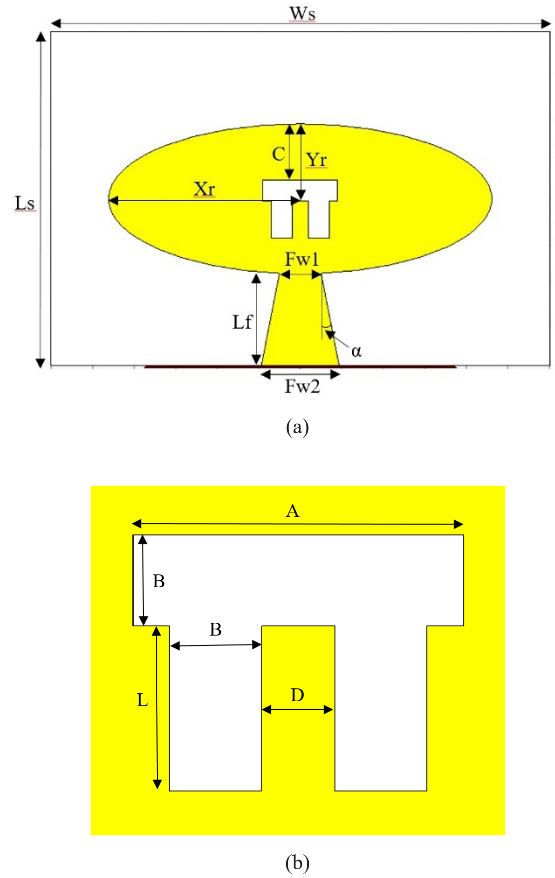

Fig. 1. (a) Front-facing view and (b) Pi-shaped slotted elliptical patch antenna.

The subsequent phase in the design process involves establishing the dimensions of the antenna structure, which are directly affected by its resonant frequency. This antenna is intended to function within a frequency range of 4.5-9.5 THz, with an operational frequency set at 5.5 THz. At this frequency, the wavelength of the signal is considerably shorter than that at lower frequencies, significantly influencing the antenna's dimensions. When designing an elliptical patch antenna, it is essential to determine both the semi-major axis and semi-minor axis of the patch. This calculation relies on the targeted resonant frequency, substrate properties, and operating environment conditions.

The semi-major axis of the elliptical patch is computed as follows [20], [21],

$$a \approx \frac{\lambda_d}{2} \tag{1}$$

where λ_d is the wavelength in the dielectric medium which can be calculated as

$$\lambda_d = \frac{c}{f_0\sqrt{\varepsilon_{reff}}} \tag{2}$$

where ε_{reff} is the substrate's effective dielectric constant,

$$\varepsilon_{reff} = \frac{\varepsilon_r + 1}{2} + \frac{\varepsilon_r - 1}{2}\left(1 + \frac{12h}{w}\right)^{-1/2} \quad (3)$$

Here, ε_r the relative permittivity, w the width and h the height of the substrate, c the speed of light, and f_0 being the resonant frequency of the antenna. And semi-minor axis, b of an elliptical patch is calculated as

$$b = \frac{a}{AR} \quad (4)$$

where, AR is the aspect ratio, which is chosen based on the design requirements and radiation characteristics.

The optimize design parameters of the proposed THz antenna are presented in Table I. Key design parameters, including substrate dimensions, elliptical patch axes, feedline tapering, and Pi-slot geometry, are carefully tuned to support dual-band THz operation. The compact size of the designed antenna is 120 µm × 80 µm^2. The pi-shaped slotted elliptical antenna is excited using a 50 Ω tapered feedline, with the impedance maintained at 50 Ω to achieve high performance.

Table I
Optimal Values of Design Parameters

Parameters (symbol)	Value (µm)
Width of substrate (Ws)	120
Length of substrate (Ls)	80
Thickness of substrate	6
Semi major axis (Xr)	46
Semi minor axis (Yr)	17.96
Thickness of patch & ground	1.2
Length of feedline (Lf)	22.04
Top-end width of feedline (Fw1)	8
Bottom-end width of feedline (Fw2)	18.64
Taper angle (α)	11.07º
Pi slot length (A)	18
Width of pi slot (B)	5
Legs length of pi slot (L)	9
Distance between the legs of pi slot (D)	4
Top-to-slot offset (C)	13.46

Tuning the pi-slot geometry is achieved through systematic parametric variation in CST. CST allows defining the pi-slot length, width, and position as parameters. These are varied systematically to observe their effect on S11 (return loss). Authors run multiple simulations, adjusting geometry until the desired THz band performance is achieved.

The shape of the initially designed radiating element is an elliptical patch. The original elliptical patch is modified by inserting a pi-shaped slot. A pi-shaped slot can create multiple current paths, enabling broadband operation. This slot is etched for impedance matching, bandwidth enhancement, and antenna radiation characteristics improvement. The pi-shaped slot, which is a modified inverted U-shaped slot, is well-known for its relatively large impedance bandwidth. Hence, the dimensions of the pi-slot are adjusted to achieve the lowest possible input reflection coefficient of the antenna around the resonant frequencies, and their position is chosen so that the radiating structure can produce a wider bandwidth through multiple resonances while also providing proper impedance matching at the higher end of the operating range, ensuring stable performance across the full THz band.

III. Results and Parametric Investigation

The design, simulation, parametric investigation and performance analysis of the pi-shaped slotted patch antenna has been carried out high-performance EM solver CST-MWS. The performance of the proposed antenna has been investigated by computing S11, bandwidth, gain, directivity, efficiency, and radiation pattern, and surface current density from the simulator.

Fig. 2 demonstrates the impact of incorporating a pi-shaped slot on the elliptical patch of the proposed THz antenna design. It compares the reflection coefficient (S11) of the proposed antenna with and without a pi-slot. The antenna with the slot shows lower S11 values at key frequencies, indicating better impedance matching, reduced reflection, and improved performance. The inclusion of the pi-slot effectively reduces the return loss and alters the peak positions of the proposed antenna. The operating range of frequencies of the antenna is 5.01 to 8.42 THz. A minimum S11 of −43.57 dB is observed at 5.645 THz, indicating excellent impedance matching. The presence of two distinct resonant dips (at 5.645 and 7.715 THz) suggests the antenna is designed for multi-band THz operation, which is valuable for applications like THz imaging, spectroscopy, or high-speed wireless communication.

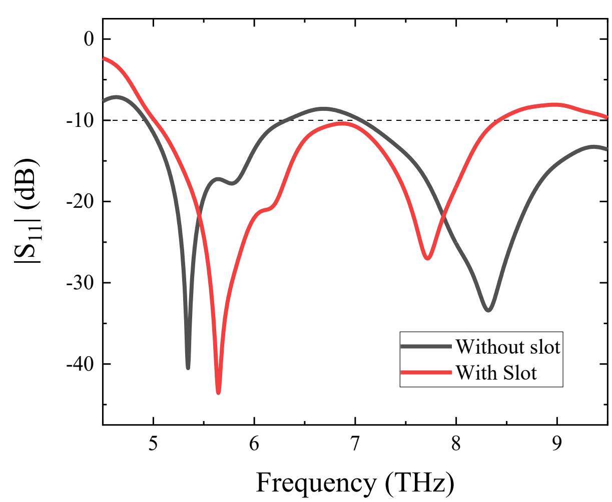

Fig. 2. Comparison of $|S_{11}|$ for proposed antenna with and without the pi-slot.

The reason behind the shifting of the resonant frequencies are as follows. The pi-slot elongates the path that surface currents follow, effectively increasing the electrical length of the antenna, and lowers the fundamental resonant frequency. The pi-slot introduces discontinuities that support multiple current loops, each capable of resonating at different frequencies. This leads to additional resonant peaks and broader bandwidth. The slot acts as a combination of inductive and capacitive elements. These reactive components shift the resonance by modifying the input impedance and phase response. The slot also alters the distribution of the electric and magnetic fields on the patch, which changes the boundary conditions and shifts the natural resonant modes. It can couple different parts of the patch or ground plane, introducing mutual coupling that shifts resonant frequencies.

The variation of S11 with different semi-major axis (Xr) of the presented THz antenna is shown in Fig. 3, which depicts that increasing the Xr while keeping the semi-minor axis (Yr) constant leads to a downward shift in both primary and secondary resonant frequencies. As Xr increases (40 to 49 µm), the resonance frequency shifts downward. Larger Xr values effectively increase the electrical length of the resonant structure, lowering the natural frequency. Xr = 40 µm (black) resonates at a higher frequency. Xr = 49 µm (blue) resonates at a noticeably lower frequency. The bandwidth broadens with increasing Xr. At smaller Xr (40 µm), the resonance dip is sharper and narrower. At larger Xr (46–49 µm), the dips are wider, meaning the device maintains good impedance matching across a broader frequency range. The resonance depth (minimum S_{11}) also improves slightly with larger Xr, indicating better matching. Xr = 49 µm shows both deep resonance and wide bandwidth, making it robust in terms of performance.

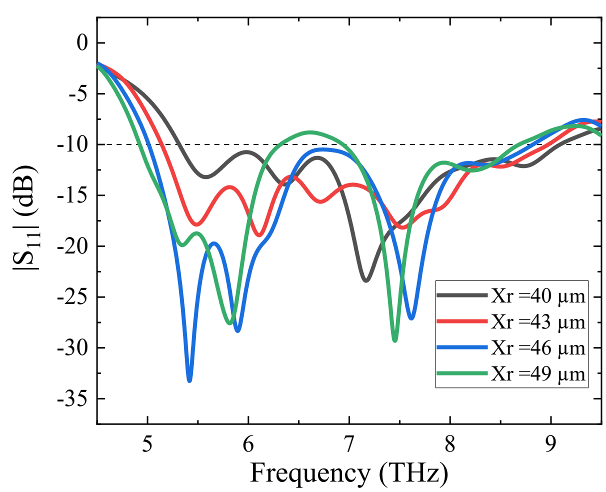

Fig. 3. Variation of |S11| with different Xr.

Fig. 4 shows the variation of radiation efficiency with different Xr of the proposed antenna. All curves show a sharp rise in efficiency from ~4 THz to ~5 THz, then stabilize. Efficiency improves consistently with increasing Xr, indicating better radiation characteristics. Increasing the Xr enhances the effective aperture and current distribution, reducing losses and improving radiation. Larger Xr values likely improve impedance matching and mode confinement, contributing to higher efficiency. Xr of 49 µm yields the best radiation efficiency across the 4–9 THz range. This makes it ideal for applications requiring power-efficient transmission, such as THz imaging, sensing, or communication.

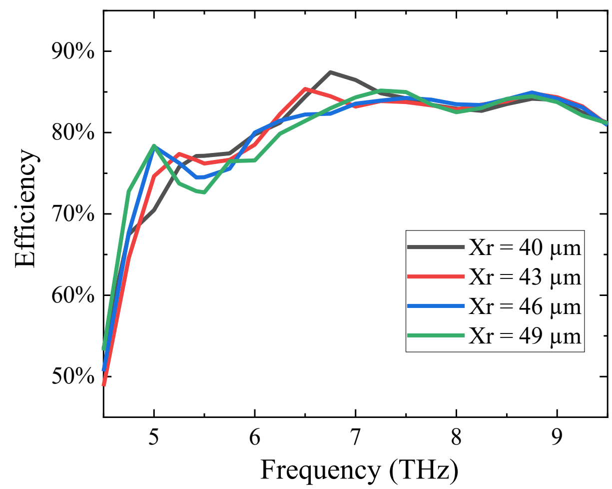

Fig. 4. Variation of efficiency with different Xr.

Fig. 5 shows the variation of gain with different Xr for the designed antenna. As seen from Fig. 5, the directional gain increases from 3.2 dB to 8.2 dB with increasing frequency for all designs with different Xr while keeping the Yr constant. At smaller Xr (40 µm), the gain peaks are slightly lower and occur at higher frequencies. As Xr increases, the gain peak values rise modestly, with Xr = 46 µm and 49 µm showing stronger gain performance across the mid-THz band.

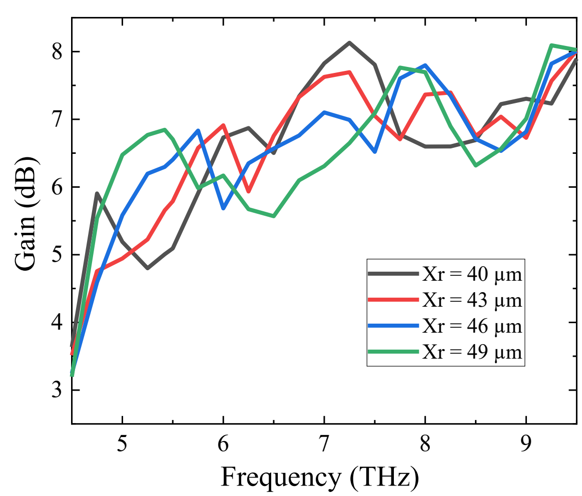

Fig. 5. Variation of gain with different Xr.

Fig. 6 depicts the variation of S_{11} with different length of feedline (Lf) of proposed THz antenna. It is evident from Fig. 6

that as Lf increases (22.04 to 32.04 µm), the resonant frequency shifts downward. A larger Lf increases the effective path length of the resonant structure, lowering its natural frequency. At smaller Lf (22.04 µm), the resonance dip is shallower (around –20 to –25 dB), indicating weaker matching. As Lf increases, the resonance depth improves, with Lf = 30.04 µm and 32.04 µm showing deeper dips (~ –35 to –40 dB), meaning stronger impedance matching and reduced reflection. The dips also broaden slightly with larger Lf, suggesting improved bandwidth. Smaller Lf values produce sharper, narrower resonances, while larger Lf values yield wider operational ranges.

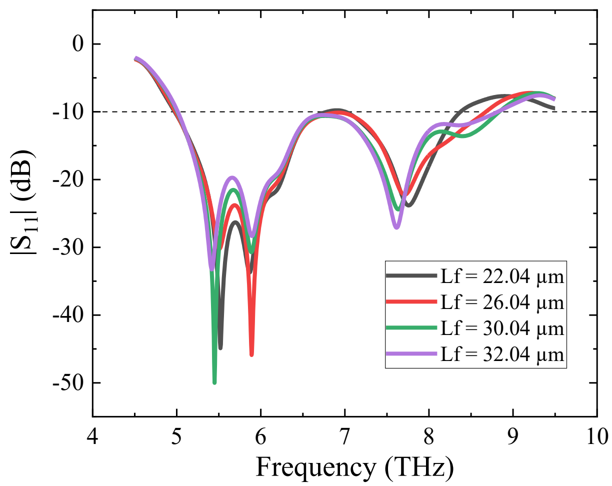

Fig. 6. Variation of |S11| with different Lf.

Fig. 7 illustrates how efficiency varies with frequency for different values of Lf across the THz band. As seen the efficiency varies from 55% to 85% in the operating THz range of frequencies. All curves show a rapid initial rise (4.5–5.5 THz) in efficiency, where larger Lf values (e.g., 30.04 µm, 32.04 µm) reach higher efficiency slightly earlier compared to smaller Lf values. Then it stabilizes across the band. There is a plateau region (5.5–9.5 THz) where efficiency stabilizes between ~75–85%. The higher Lf values sustain slightly higher efficiency across the plateau by enhancing impedance matching and mode coupling. For example, Lf = 32.04 µm (purple) maintains efficiency closer to the upper bound (~85%), while Lf = 22.04 µm (black) sits nearer the lower bound (~75–78%).

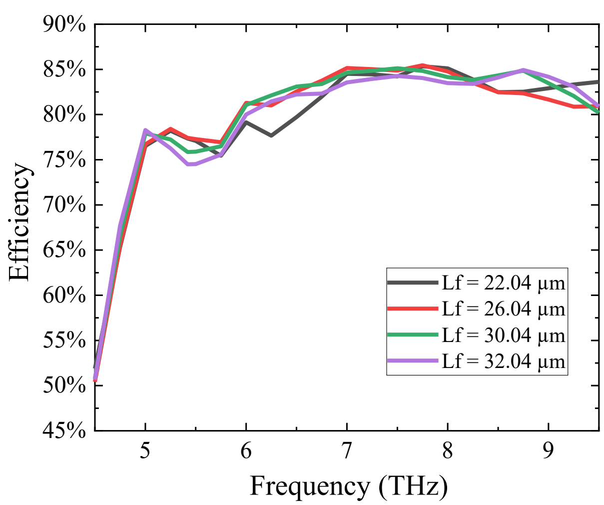

Fig. 7. Variation of efficiency with different Lf.

Fig. 8 illustrates how the parameter Lf influences gain across the THz frequency band. As Lf increases, the peak gain shifts toward lower frequencies. Smaller Lf values (22.04 µm) yield higher peak gain (~8.5–9 dB), while larger Lf values (32.04 µm) produce lower peak gain (~6–7 dB). Thus, increasing reduces the achievable peak gain at lower range of frequencies. At higher range of frequencies, at smaller Lf (22.04 µm), the gain peaks are lower (around 5–6 dB). As Lf increases, the gain peak values rise, with Lf = 30.04 µm and 32.04 µm reaching closer to 8 dB.

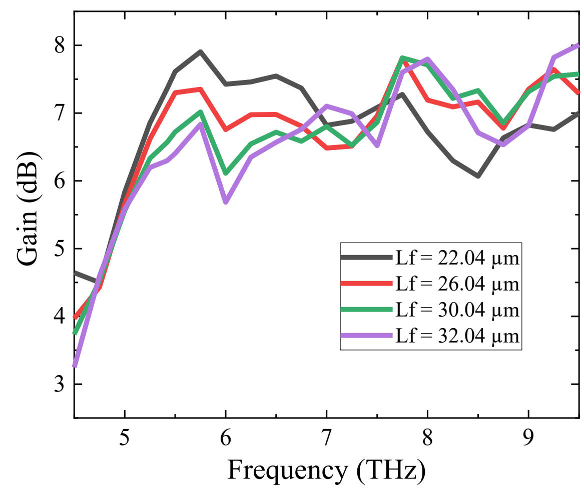

Fig. 8. Variation of gain with different Lf.

Fig. 9 depicts the influence of Top-End Width of Feedline (Fw1) on the antenna's reflection behavior. Narrower feedlines (8 µm) tend to resonate at lower frequencies due to higher inductance. Wider feedlines (14 µm) shift resonance upward but

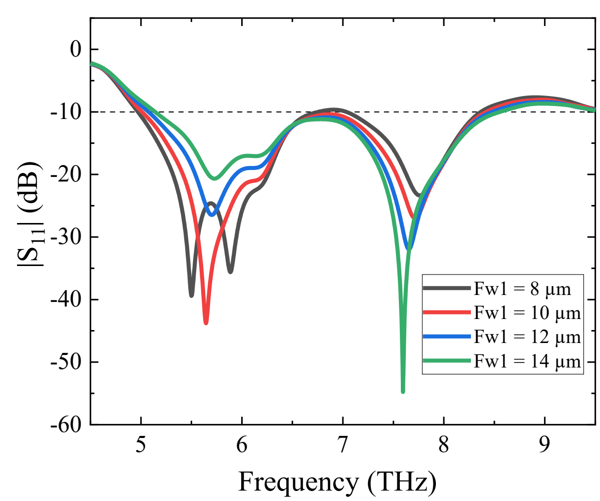

Fig. 9. Variation of S11 with different Fw1.

may degrade matching due to increased capacitive loading or altered current distribution. The 10 μm width feedline strikes the best balance, which offers broadband performance with multiple resonant dips.

Fig. 10 illustrates the impact of Fw1 on antenna's efficiency. All curves show a sharp increase in efficiency between 4.5 THz and 5 THz. Beyond 5 THz, efficiency stabilizes above 80% for all feedline widths. 8 μm shows slightly reduced performance, possibly due to higher conductor loss or impedance mismatch. 14 μm may introduce parasitic effects or altered current distribution, slightly degrading efficiency. The 10 μm wide feedline offers optimal radiation efficiency across the operating THz band.

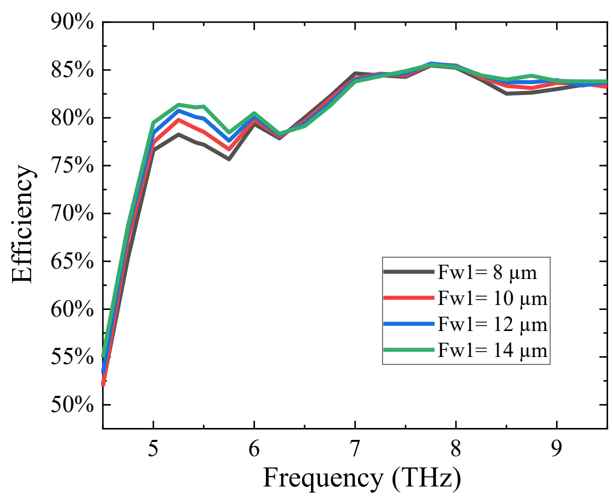

Fig. 10. Variation of efficiency with different Fw1.

Fig. 11 shows the impact of Fw1 on the THz antenna's gain. All curves show moderate gain variation across the band. Gain generally increases with frequency, peaking between 7 to 8 THz, then slightly tapering off. Smaller Fwl values yield higher peak gain at the resonant frequencies. In the operating range, the gain decreases from about 7.8 dB to about 6.2 dB, this is

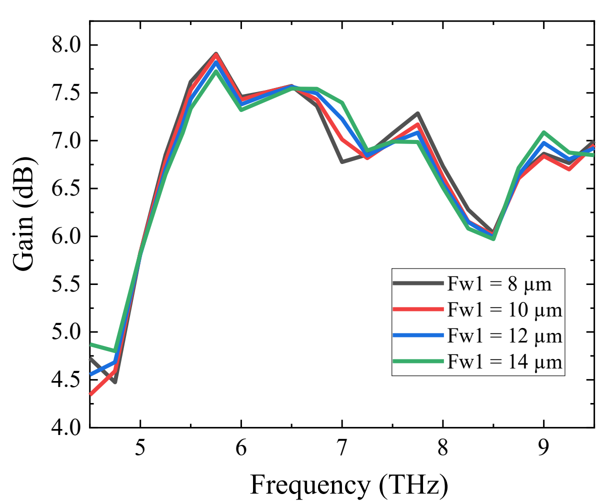

Fig. 11. Variation of gain with different Fw1.

a reduction of roughly 1.6 dB across the range. So, a smaller Fwl value of 8 μm is chosen in the present design as a narrower feedline at the connection point to the patch ensures the transition from the 50 Ω feedline to the patch impedance is smooth, reducing mismatch and improving return loss and efficiency.

The variation of S11 with frequency for different Pi slot length (A) of the presented THz antenna is shown in Fig. 12. The red curve for A=18 μm shows a strong dip well below -10 dB, indicating efficient impedance matching and reduced reflection. Around the resonant frequency, the -10 dB bandwidth for A = 18 μm is broader than for A = 16 μm or A = 22 μm. A = 16 μm gives a resonance but S11 not as deep as below -10 dB, while A = 20 μm and 22 μm shift the resonance but with less favorable reflection levels. The 18 μm case strikes the best balance between depth, bandwidth, and frequency positioning. Therefore, looking at the S11 plot, the case of A = 18 μm (red curve) appears better because it achieves a deeper and more stable resonant dip below the -10 dB threshold compared to the other values.

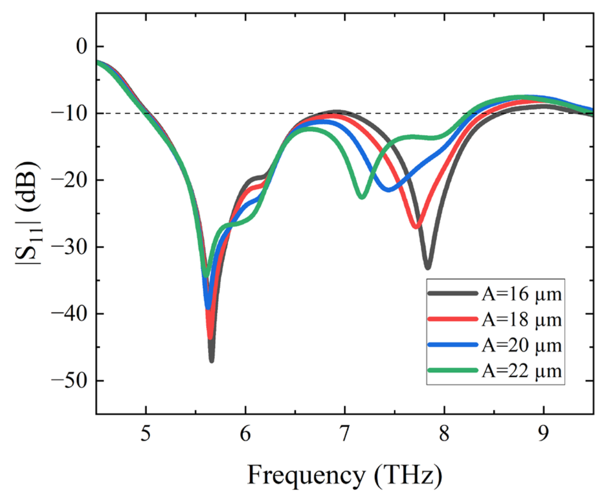

Fig. 12. Dependence of S11 on Pi slot length (A).

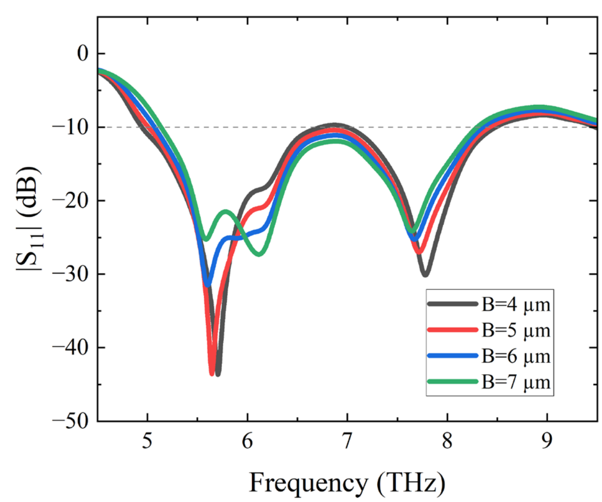

Fig. 13. Dependence of S11 on different width of pi slot (B).

Fig. 13 depicts the dependence of S11 versus frequency plot on different values of width of pi slot (B). As seen from the figure, the case of B = 5 µm (red curve) is better because it achieves a deeper and more effective resonance compared to the other values. B = 4 µm shows resonance but not as deep, while B = 6 µm and 7 µm shift resonance with weaker dips. The 5 µm case balances depth, bandwidth, and frequency positioning most effectively.

The dependence of S11 versus frequency plot on Legs length of pi slot (L) is shown in Fig. 14. As seen, L = 10 µm achieves a very deep resonance dip (close to –50 dB); the dip is relatively broad compared to L = 8 µm and 9 µm, meaning it covers a wider frequency range effectively. L = 11 µm also shows good bandwidth, but its resonance shifts lower in frequency. L = 11 µm is equally strong in matching but better suited if your design targets lower frequencies. When evaluating bandwidth and impedance matching (resonance depth) together, the best-performing case is L = 10 µm (blue curve).

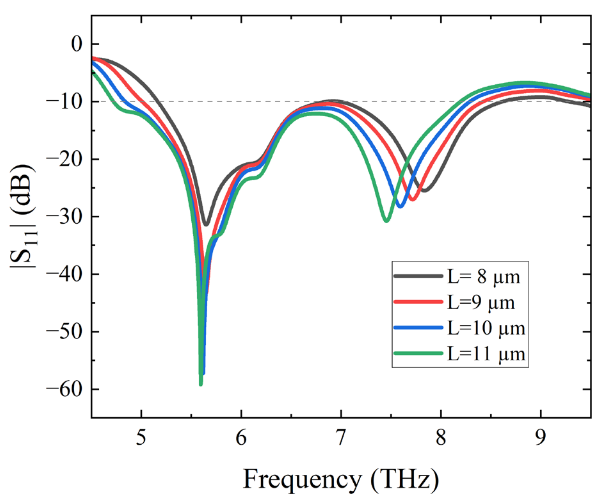

Fig. 14. Dependence of S11 on Legs length of pi slot (L).

Fig. 15 presents the simulated radiation efficiency of the proposed pi-shaped slotted elliptical patch antenna. The antenna possesses an efficiency of 77.43% at 5.645 THz, while exhibits ~70–85% efficiency within the operating range of 5.01 THz to 8.42 THz, confirming low loss and effective radiation. High radiation efficiency across the operating bands suggests the antenna is well-suited for THz applications requiring high power delivery, such as imaging, sensing, or high-data-rate communication.

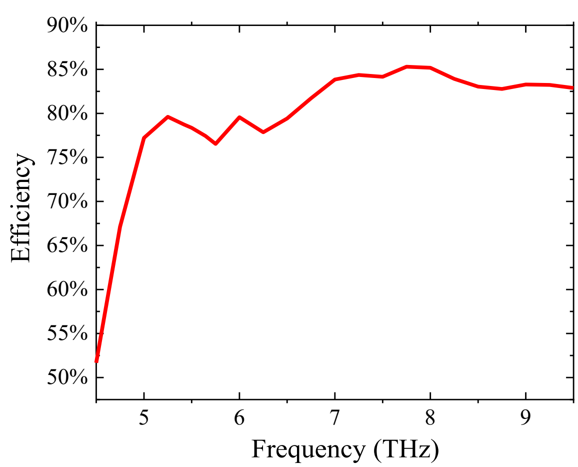

Fig. 15. Simulated radiation efficiency of the proposed antenna.

Fig. 16 presents the simulated VSWR (Voltage Standing Wave Ratio) of the proposed THz antenna over the frequency range 4.5 THz to 9.5 THz. A VSWR < 2 over a wide operating frequency band (5.01 to 8.42 THz) confirms the antenna achieves excellent impedance matching with efficient power transfer and minimal reflection losses, validating the antenna's suitability for broadband THz applications.

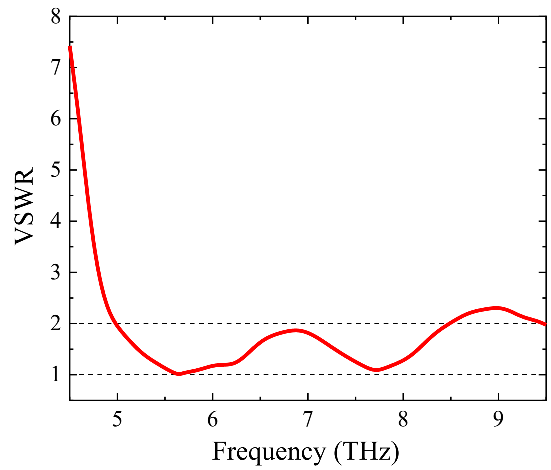

Fig. 16. VSWR of the proposed antenna.

Gain pattern of the pi-shaped slotted elliptical patch antenna at 5.645 THz is depicted in Fig. 17(a), while its directivity pattern is presented in Fig. 17(b). At 5.645 THz, the antenna exhibits a gain of 7.906 dB and a directivity of 9.017 dBi. Fig. 17(c) shows the gain and directivity performance of the proposed THz antenna over the range 4.5 to 9.5 THz. Gain peaks at ~5.6 THz, fluctuates 4.32 to 6.05 dB, and remains above 6 dB across most of the spectrum, supporting strong radiation. The antenna demonstrates consistently high directivity across the operating THz range, fluctuating between 6.0 dBi and 9.5 dBi, indicating strong directional radiation characteristics throughout the operating band. These results confirm its suitability in focused THz applications such as point-to-point communication, imaging, and sensing.

Gain fluctuations across the specified frequency band may stem from several interrelated physical and design factors like resonant mode behavior, slot geometry effects, Impedance mismatch, and surface current distribution. The present UWB antennas are designed to function across multiple resonant modes, thereby enabling enhanced performance over a broad frequency spectrum. Each mode may radiate differently, leading to peaks and dips in gain at various frequencies. The slot introduces multiple resonances. While this helps bandwidth, it can also cause uneven gain due to varying coupling strength at differ-

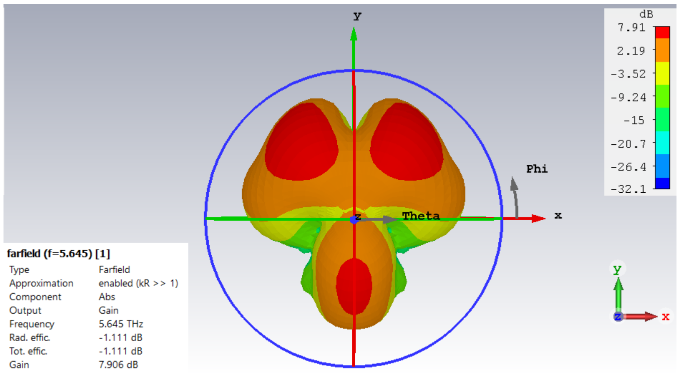

(a)

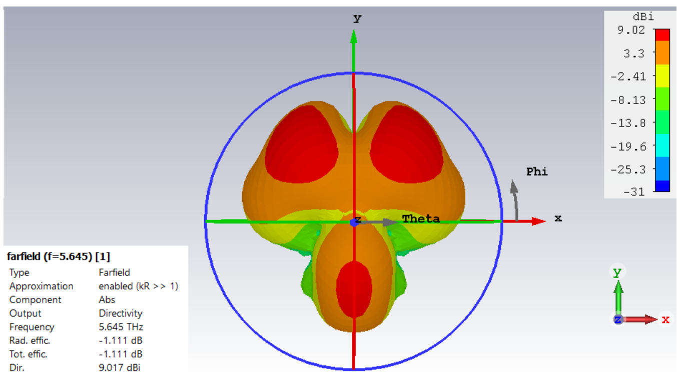

(b)

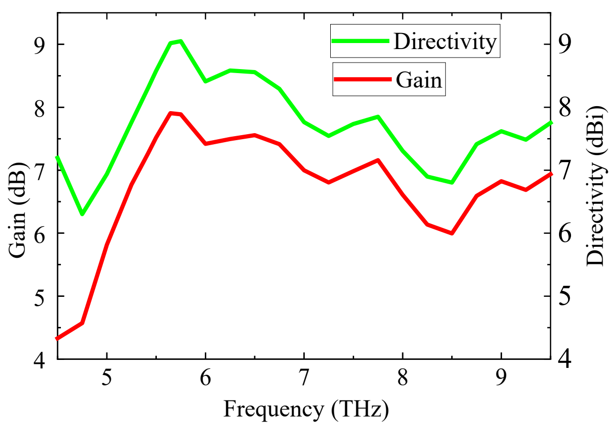

(c)

Fig. 17. (a) 3D farfield gain pattern, (b) 3D farfield directivity pattern, (c) Gain and directivity versus frequency for the proposed THz antenna over the operating frequency range.

ent frequencies. Even with good return loss, perfect impedance matching across the entire UWB band is difficult. Minor mismatches at certain frequencies can reduce radiation efficiency, causing gain dips. The current paths on the patch and ground plane change with frequency. At higher frequencies, these paths may become less efficient or radiate in undesired directions.

Fig. 18 presents the polar plot of the far-field electric field (E-field) and magnetic field (H-field) at a frequency of 5.645 THz for φ = 0º and 90º. At φ = (0°, 90°), the main lobes of the E-field and H-field patterns are focused at (0°, 29°), with respective magnitudes of (15.1 dB V/m, 20.8 dB V/m) and (−36.4 dBA/m, −30.7 dBA/m). The 3 dB angular beamwidths are (47.7°, 21.3°), and the side lobe level is −2 dB. The narrow beamwidth and low side lobe level imply a highly directional antenna, ideal for THz applications requiring spatial precision such as targeted sensing, imaging, or line-of-sight communication where spatial resolution and minimal interference are critical.

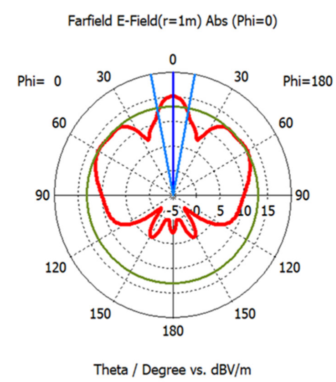

(a)

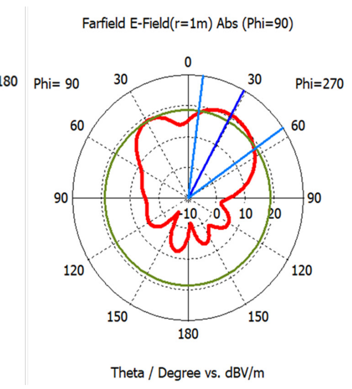

(b)

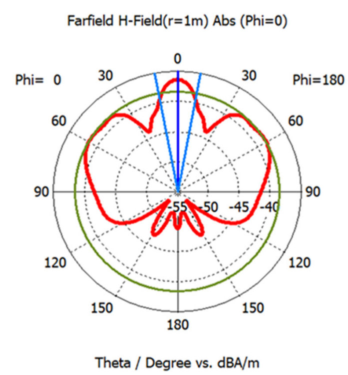

(c)

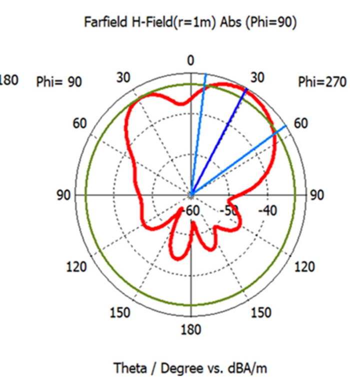

(d)

Fig. 18. 2D Farfield E-Field pattern at 5.645 THz for (a) Ø=0°, (b) Ø=90° and H-field pattern for (c) Ø=0°, (d) Ø=90°.

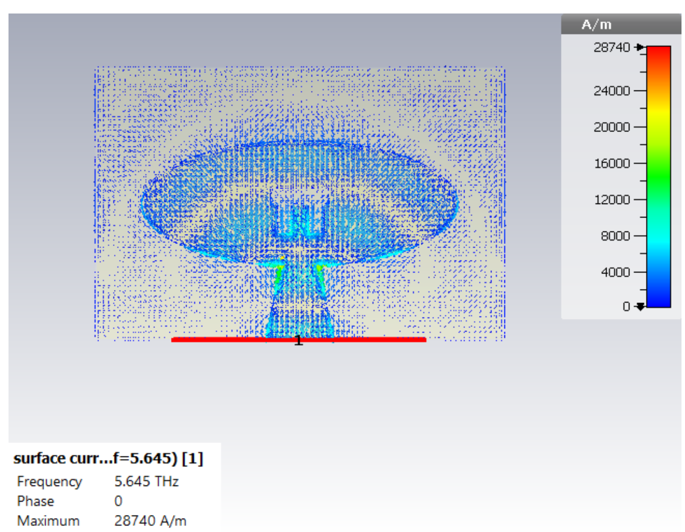

Fig. 19. Surface current at 5.645 THz.

Fig. 19 shows the simulation result of the surface current distribution of the proposed antenna at 5.645 THz. The maximum surface current density of 28,740 A/m occurs at the lower part of the feedline, the lower edges of the patch, and the slot, attributed to field enhancement and boundary conditions.

Table II shows a summary of the performance metrics of the proposed THz antenna. The low VSWR and high return loss confirm that the antenna is well-tuned to its operating frequency. The wide bandwidth and compact size make it suitable for on-chip THz communication, spectroscopy, or imaging systems. This antenna demonstrates excellent impedance matching, high gain, directivity, and efficiency at terahertz frequencies. Input impedance is very close to the standard 50 Ω, which ensures its compatibility with THz transmission lines and measurement equipment. It balances compact size, broad bandwidth, and high efficiency, which is rare at such high frequencies. The present compact THz antenna achieves a notable gain of 7.906 dB, underscoring its effectiveness for directional transmission and reception in point-to-point THz communication systems. High directivity (9.017 dBi) indicates focused radiation, which is ideal for targeted sensing or communication. Max Surface Current of 28,740 A/m indicates strong resonance and active current regions.

Table II
Performance of the Proposed THz Antenna

Size	120×80 (9600 μm²)
Return loss	-43.57 dB (at 5.645 THz)
Bandwidth	3.41 THz
VSWR	1.01 (at 5.645 THz)
Radiation efficiency	77.43% (at 5.645 THz)
Gain	7.906 dB (at 5.645 THz)
Directivity	9.017 dBi (at 5.645 THz)
Impedance	50.704 Ω (at 5.645 THz)
Surface current	28740 A/m (at 5.645 THz)

IV. Comparative analysis

Table III presents a comparative analysis of the proposed antenna's strengths and compatibility with previous designs. The proposed pi-slotted elliptical patch antenna achieves a maximum bandwidth of 3100 GHz within a compact footprint of 120 × 80 μm² (9600 μm²), and demonstrates excellent radiation characteristics including VSWR of 1.01, reflection coefficient of −43.57 dB, gain of 7.906 dB, and efficiency of 77.43%.

The present design has the smallest footprint (9,600 μm²), ideal for integration in THz chips or compact modules. [7] offers excellent performance but at 1,000,000 μm², which is impractical for miniaturized systems. [7] leads with -64.16 dB, indicating super impedance matching. *This Work* and [22] both show -43.57 dB, which is still excellent and highly efficient for THz operation. "This Work" achieves the widest bandwidth: 0.5–4.82 THz (≈3100 GHz), supporting ultra-broadband THz applications. [22] follows with 2.72–4.52 THz (≈1250 GHz), still impressive but narrower. "This Work" reach 7.906 dB, the highest among all entries, ensuring strong signal transmission.

Ref. [7] tops with 98% efficiency, but again, its size is a limiting factor. "This Work" maintains a solid 77.43% efficiency, balancing compactness with respectable efficiency. Elliptical patch designs ([22], "This Work") outperform others in gain and bandwidth, likely due to smoother current distribution and broader resonant modes. Rectangular and hybrid shapes [8], [9], [19], show moderate performance, often limited by narrower bandwidth and lower gain.

Proposed antenna design stands out as the most balanced and optimized THz solution, offering: Ultra-compact size, Exceptional bandwidth, High gain, and Strong efficiency. It is particularly well-suited for next-generation THz systems requiring miniaturization, broadband capability, and high-performance radiation. In THz systems, miniaturization, broadband capability, and high radiation efficiency are critical. "This Work" achieves an optimal balance of these factors, making it a strong candidate for: On-chip THz communication, High-resolution imaging, and Spectroscopy and sensing applications.

Table III
Comparison with Existing THz Antennas

Ref. No.	Antenna Size (μm2) (λ_g×λ_g)	Patch Shape/ Substrate	S11 (dB)	Bandwidth (GHz)	Gain (dB)	Efficiency (%)
[7]	1000 × 1000 (12.33λ_g×12.33λ_g)	Square/ Polyimide	-64.16	26.7 (2.15–2.2 and 2.56–2.6 THz)	6.793	98
[8]	208 × 180 (1.216λ_g×1.052λ_g)	Rectangular/ Silicon	−21.67	50 (0.696 THz)	4.01	64.12
[9]	100 × 100 (4.81λ_g× 4.81λ_g)	Rectangular & Circular/ Si and Teflon	−57.54	199.6 (5.5 THz)	2.76	–
[10]	24 × 24 (0.30λ_g× 0.30λ_g)	Square loop / Polyimide	−28	38 (2.3 THz)	5	60
[18]	300 × 300 (0.852λ_g×0.852λ_g)	Circular ring / Polyimide	−24.5	415 (0.523–0.9395 THz)	5.87	80
[19]	500 × 500 (2.68λ_g× 2.68λ_g)	Rectangular/ FR4	−16.86	92 (0.761 -0.853 THz)	6.14	–
[22]	140 × 100 (1.43λ_g× 1.02λ_g)	Elliptical/ Rogers	−27.08	1250 (2.12-3.37 THz)	7.769	89
This Work	120×80 (2.83λ_g× 1.89λ_g)	Elliptical/ Rogers	-43.57	3100 (5.01-8.42 THz)	7.906	77.43

V. Conclusions

In the THz frequency domain, the development of microstrip patch antennas capable of supporting high data rates and wide bandwidth poses a significant engineering challenge. This paper proposes a compact UWB elliptical patch antenna featuring a pi-shaped slot and a 50 Ω tapered feedline to address the demand for high data rate THz transmission. An elliptical patch antenna has been designed with a pi-shaped slot for the first time in the THz spectral region, enabling simultaneous size miniaturization, wideband or multi-band performance, improved impedance matching, and enhanced gain. Optimizing the dimensions and geometry of the patch, slot, and feedline was crucial for achieving wide bandwidth and low return loss. The antenna size is compact 120×80×6 μm3. The simulation result obtained from CST simulator has shown the proposed antenna exhibited broad impedance bandwidth of 3.41THz (from 5.01 to 8.42 THz), high gain of 7.906 dB, high directivity of 9.017 dBi acceptable radiation efficiency of 77.83%, and low return loss of -43.57 dB and low VSWR 1.0, surface current of 28740 A/m at 5.645 THz. The proposed antenna supports ultra-high data rates owing to its wide bandwidth of 3.41 THz. Additionally, it achieves a gain of 7.906 dB and an efficiency of 77.83%. With its simple feeder structure, low manufacturing cost, wide bandwidth, and high gain, the proposed antenna presents a suitable candidate for THz high-speed communication applications. In future work, Machine learning algorithms can be applied to optimize antenna geometries, predict performance, and accelerate prototyping. The antenna's performance can be improved by applying different performance enhancement methods and with the use of advanced materials and metamaterials.

Future work will focus on developing suitable measurement setups to experimentally validate the radiation characteristics and further strengthen the reliability of the proposed design. Simulation will be performed for the same design with the TLM mesh using the CST. Future works will also aim to develop a theoretical model to the design process of the Pi slotted THz antenna. The skin effect and surface roughness will also be accounted in the simulations.

References

[1] I. F. Akyildiz, J. M. Jornet, and C. Han, "Terahertz band: Next frontier for wireless communications," *Physical Communication*, vol.12, pp. 16-32, 2014, DOI: 10.1016/j.phycom.2014.01.006.

[2] A. N. Bharadwaj, A. M. Kashyap, G. B. N, R. Jayachandran and R. Kishore, "A Survey on Terahertz Devices-A cutting edge Technology," in Proc. *2023 Int. Conf. on Recent Trends in Electronics and Communication (ICRTEC)*, Mysore, India, pp. 1-6, DOI: 10.1109/ICRTEC56977.2023.10111851.

[3] S. Elaage, M. El Ghzaoui, N. Mrani, R. El Alami, A. El Alami, M. O. Jamil, and H. Qjidaa, "Modeling and analysis of short distance terahertz communication channel," in *Lecture Notes in Networks and Systems (LNNS)*, vol. 669, pp 289–297, 2023, DOI: 10.1007/978-3-031-29860-8_30.

[4] I. Akyildiz, J. Jornet, and C. Han, "TeraNets: Ultra-broadband communication networks in the terahertz band," *IEEE Wireless Commun.*, vol. 21, no. 4, pp. 130–135, Aug. 2014, DOI: 10.1109/MWC.2014.6882305.

[5] Z. Jin, Y. Rong, J. Yu, and F. Wu, "Design of a compound reconfigurable terahertz antenna based on graphene," *Plasmonics*, vol. 19, pp. 621–629, 2024. DOI: 10.1007/s11468-023-02011-8.

[6] R. Pant, and L. Malviya, "THz antennas design, developments, challenges, and applications: A review," *International Journal of Communication Systems*, Vol. 36, Issue 8, e5474, 2023, DOI: 10.1002/dac.5474.

[7] S. Mrunalini, and A. Manoharan, "Dual-band re-configurable graphene-based patch antenna in terahertz band for wireless network-on-chip applications," *IET Microwaves, Antennas & Propagation*, vol. 11, pp.2104-08, 2017, DOI: 10.1049/iet-map.2017.0415.

[8] S. Ullah, C. Ruan, T. U. Haq, and X. Zhang, "High performance THz patch antenna using photonic band gap and defected ground structure," *Journal of Electromagnetic Waves and Applications*, vol. 33, pp. 1943-54, 2019, DOI: 10.1080/09205071.2019.1654929.

[9] M. A. Khan, T. A. Shaem, and M. A. Alim, "Analysis of graphene based miniaturized terahertz patch antennas for single band and dual band operation," *Optik*. Vol. 194, pp.163012, 2019, DOI: 10.1016/j.ijleo.2019.163012.

[10] K. Vijayalakshmi, C. K. Selvi, and B. Sapna, "Novel tri-band series fed microstrip antenna array for THz MIMO communications," *Optical and Quantum Electronics*, vol. 53, pp. 395, 2021, DOI: 10.1007/s11082-021-03065-w.

[11] B. Moulfi, S. Ferouani, D. Ziani-Kerarti, and W. Moulessehoul, "Wide Band Nano Circular Graphene Printed Antenna for Terahertz Transmission with DGs," *Telecommunications and Radio Engineering,* vol. 81, pp. 37 2022, DOI: 10.1615/TelecomRadEng.2022042936.

[12] M. A. K. Khan, T. A. Shaem, and M. A. Alim, "Graphene patch antennas with different substrate shapes and materials," *Optik*, vol. 202, pp. 163700 2020, DOI: 10.1016/j.ijleo.2019.163700.

[13] A. Abohmra, F. Jilani, H. Abbas, M. A. Imran and Q. H. Abbasi, "Terahertz Antenna based on Graphene for Wearable Applications," in *2019 IEEE MTT-S International Wireless Symposium (IWS)*, Guangzhou, China, pp. 1-3, DOI: 10.1109/IEEE-IWS.2019.8803929.

[14] M. M. Fakharian, "A graphene-based multi-functional terahertz antenna," *Optik*, vol. 251, pp. 168431, 2022, DOI: 10.1016/ j.ijleo.2021.168431.

[15] N. S. Badr, and G. Moradi, "Graphene-Based microstripfed hexagonal shape dual band antenna," *Optik*, vol. 202, pp. 163608, 2020, DOI: 10.1016/j.ijleo.2019.163608.

[16] G. Nissiyah, and M. Ganesh, "Analysis of single band and dual band graphene based patch antenna for terahertz region," *Physica E: low-dimensionl systems and nanostructures*, vol. 94, pp. 126131, 2017, DOI: 10.1016/j.physe.2017.08.001.

[17] P.-L. Sun, "420-GHz terahertz SIW slot antenna with quartz superstrates in silicon technology," *Optoelectron. Lett.,* vol. 16, pp. 25–28, 2020, DOI: 10.1007/s11801-020-9063-8.

[18] W. A. Khan, and A. B. Muhammad, "Design and analysis of wideband THz micro size patch antenna for 6G application," in *Proc. 6th IEEE Int. Conf. on Millimeter-Wave and Terahertz Technologies (MMWaTT)*, Tehran, Iran, pp.1-4, 2022, DOI: 10.1109/MMWaTT58022.2022.10172086.

[19] K. K. Naik, "Asymmetric CPW-fed patch antenna with slits at terahertz applications for 6G wireless communications," *Wireless Networks*, vol. 30, pp. 2343-51, 2024, DOI: 10.1007/s11276-024-03695-4.

[20] D. M. Pozar, *Microwave Engineering*, Wiley, Hoboken, NJ, USA, 2011, pp. 115-135, ISBN: 978-0470631553.

[21] R. Garg, P. Bhartia, I. Bahl, and A. Ittipiboon, *Microstrip Antenna Design Handbook*, Artech House, Norwood, MA, USA, 2001, pp. 15-42, ISBN: 978-0890065136.

[22] R. Masum, M. Islam, S. Roy, M. F. Ahmed, M. M. Islam, M. R. Hossain, and R. Sarkar, "A Slotted Elliptical Patch Antenna for Six Generation Communication System in Terahertz Band," *Cureus J Eng* 2, es44388-024-02717-3, January 25, 2025, DOI: 10.7759/s44388-024-02717-3.

Design and Implementation of Polyester-Based Textile Antenna for Smart Clothing

Md. Samiul Islam and Abu Zafor Md. Touhidul Islam

***Abstract*—In the present study, a newly designed polyester substrate-based textile microstrip patch antenna operating in the 3.5 GHz band is proposed for smart clothing in broadband wireless applications. The motivation behind this work stems from the lack of comprehensive studies that address all critical aspects—including off-body performance, fabrication, testing, on-body evaluation, bending analysis, and SAR assessment—while specifically focusing on polyester textile antenna designs for the 3.5 GHz band in next-generation wearable systems. The antenna of small dimension 30×20×0.8 mm³ is designed and simulated in CST, followed by prototype fabrication and subsequent measurements to validate the simulation results. Slotting and partial grounding techniques are employed in the design for improving the radiation performance of the antenna. The effectiveness of the antenna has been assessed under the off-body and on-body conditions. Bending analysis under various bending conditions is performed to assess the antenna's flexibility and suitability for wearable applications. Experimental results obtained from the fabricated antenna in free space and on-body scenarios show agreement with simulation data. Moreover, the specific absorption rate (SAR) analysis confirming that the antenna complies with IEEE safety standards. The proposed antenna achieves a wide bandwidth of 1.17 GHz (operating range of 3.11-4.27 GHz), a higher radiation efficiency of 94.52%, and a moderate peak gain of 2.59 dB. It covers 5G NR (n77, n78), C-Band (Radar/WiMAX), CBRS, and Extended C-Bands used for wearable broadband applications. Hence, the proposed antenna is robust and well-suited for smart clothing applications in wireless broadband applications as it combines good radiation characteristics and stable performance under bending, while maintaining safe SAR levels and a compact textile-compatible design.**

***Index Terms*—Polyester substrate, smart clothing, textile antenna, wearable, wireless broadband.**

Original Research Paper
DOI: 10.53314/ELS2630039I

Manuscript received on November 7th, 2025. Received in revised form on March 15th and April 16th, 2026. Accepted for publication on April 27th, 2026.

Md. Samiul Islam is with the Antenna Design Lab, Department of Electrical and Electronic Engineering, University of Rajshahi, Rajshahi 6205, Bangladesh (e-mail: samiulislam.ru64@gmail.com, ORCiD: 0009-0004-8345-3204).

Abu Zafor Md. Touhidul Islam is with the Antenna Design Lab, Department of Electrical and Electronic Engineering, University of Rajshahi, Rajshahi 6205, Bangladesh (e-mail: touhid.eee@ru.ac.bd, ORCiD 0009-0002-0375-4660).

I. Introduction

A rapid increase in research on body-centric wireless communication and wearable devices has been observed in recent years, attributed to their diverse applications in personal communication systems. Wearable electronics are utilized across various fields, including sports, defense, space missions, mobile medical monitoring, and general healthcare. [1]-[3]. Smart clothing refers to clothing enhanced with technology to sense and react to the wearer's body or environment. It integrates electronic components like sensors, conductive fabrics, and microcontrollers, permitting it to monitor biometrics, adjust to conditions, and even communicate with other devices. Smart textile antennas are increasingly preferred for their low cost, high flexibility, simple manufacturing procedures, lightweight, and comfort for wearable on-body applications [4]. Various antenna types including microstrip, dipole, monopole, loop, slot, and planar inverted-F (PIFA) designs are well-suited for smart textile integration. Textile antennas typically utilize materials such as polyester, cotton, denim, and plastics as dielectric substrates, combined with conductive radiating layers, to achieve the flexibility and wearability needed for garment integration [5], [6].

However, key challenges in designing textile antennas for smart clothing include maintaining antenna performance and reliability while ensuring flexibility, comfort and washability. To mitigate these challenges, researchers are exploring various approaches such as optimizing material selection and antenna geometry for various body movements, utilizing advanced fabrication techniques, addressing specific absorption rate (SAR) concerns, and so on [7]. A denim-based textile antenna introduced in [8] supports tri-band operation resonates at 2.13, 4.75, and 11.495 GHz, making it suitable for wireless systems used in emergency and surveillance contexts. A textile antenna with breathable and flexible properties was introduced in [9], operating at 2.45 GHz and incorporating a 3D spacer substrate to facilitate airflow. To enhance bandwidth, an E-shaped slot design was proposed in [10]. Despite these advancements, developing a wideband textile antenna that maintains durability and reliable data transmission under varying human body postures remains a critical challenge. Authors in [11] suggested Multiple-input multiple-output antenna as a viable approach to overcoming such limitations. In [12], a textile antenna tailored for integration into smart garments was designed, fabricated, and experimentally validated to match the simulated performance at 2.45 GHz. Bending and on-body performance analysis have also been performed.

Zhou et al. [13] introduced a circular-shaped textile antenna for wireless body area network (WBAN) services featuring dual-band (2.45 GHz and 5.8 GHz) and dual-polarization characteristics. Its performance is assessed under off-body, on-body and bending conditions. A frequency-reconfigurable textile antenna was designed and fabricated in [14] for wearable applications. In the design, denim was used as substrate, while a single PIN diode was employed to shift between the bands. Kivata et al. in [15] proposed a compact wearable textile antenna of size 30 × 30 mm². The antenna was designed to resonate at 3.4 GHz, and employs denim, jeans, and FR-4 substrate materials for applications in wireless broadband.

Although the stated antennas showed promising results for wearable applications, in most cases, they had larger sizes, narrow bandwidths, expensive substrates, and so on. Therefore, continuous advances in research are now focused on wideband, low-cost, and miniaturized antennas for wearable applications. Moreover, there's a noticeable gap in studies focusing on textile antenna designs specifically for the 3.5 GHz band, particularly for broadband wireless communication. Existing research primarily concentrates on other 5G frequencies like (2.4 - 2.484 GHz), WiMAX (2-11 GHz), and other WLAN bands. The 3.5 GHz band is relevant for various applications including telemedicine, m-health (mobile health), and e-health, making it a crucial area for further investigation. While very few studies exist on textile antenna design at 3.5 GHz [15]-[18], a comprehensive study covering all aspects such as off-body analysis, fabrication, testing, on-body analysis, bending analysis, and SAR analysis is currently lacking.

This study presents a novel polyester-based small textile patch antenna at 3.5 GHz suitable for smart clothing in wireless broadband applications. Polyester was selected as the substrate material for the antenna due to its advantageous combination of properties, including a low dielectric constant, high mechanical flexibility, lightweight and thin profile, resistance to moisture, cost-effectiveness, and widespread availability. The low dielectric constant helps to reduce surface wave losses and contributes to broader bandwidth and better radiation efficiency, especially in microstrip patch antennas. Polyester is soft, bendable, and resilient, making it ideal for integration into clothing without compromising comfort or durability. It is lightweight, inexpensive and can be manufactured in thin layers, making it a practical choice for low-profile wearable antenna designs. Compared to natural fibers like cotton, polyester absorbs less moisture, which helps to maintain stable electromagnetic properties even in humid environments. Furthermore, polyester demonstrates superior durability against washing, mechanical deformation, and environmental exposure, making it suitable for long-term wearable antenna applications.

This research is focused on designing a compact polyester-based antenna at 3.5 GHz and improving its efficiency, bandwidth, and reliability to make them viable alternatives to conventional substrates, and to make them promising for wearable and smart clothing applications. The optimized antenna dimensions are 30×20×0.8 mm³, which is notably small compared to many textile antennas, making it more practical for integration into wearable devices. The antenna resonates at 3.5 GHz and achieves a wide operating range of 3.11–4.27 GHz, covering several key communication bands 3.3–3.8 GHz (5G NR (n77, n78) band), 3.1–3.7 GHz (C-Band Radar / WiMAX band), 3.5 GHz (Citizens Broadband Radio Service (CBRS) band), and 4.0–4.2 GHz (Extended C-Band) that are highly relevant for modern wearable applications in smart clothing, sports, and healthcare. Novel implementation of slotting and partial grounding helps to improve bandwidth and efficiency. In addition, the bending analysis is performed, and the antenna's performance is tested under off-body and on-body conditions, ensuring reliability in real-world wearable scenarios. The simulation and numerical performance analysis were carried out using CST Studio software. The antenna prototype was fabricated, and the performance parameters (return loss and VSWR) were measured to validate the simulation results.

The rest of the paper is arranged as follows. The antenna design approach is discussed in Section II. Antenna Fabrication and Testing procedures are presented in Section III. Section IV presents the results and discussion, including simulation and experimental results under off-body and on-body conditions, as well as bending and SAR analyses. A comparison of the proposed antenna's performance with previously reported designs is given in Section V. Finally, key findings of the research are listed in Section VI.

II. Antenna Design Approach

Initially, the proposed antenna's design, simulation, parametric investigation, and numerical analysis were carried out in CST under the off-body (free space) condition. The prototype is then fabricated and the performance metrics are measured in the laboratory using the vector network analyzer (VNA). After that numerical analysis under the on-body condition, bending analysis and SAR analysis were performed in CST.

Fig. 1 describes the construction of the projected antenna designed to resonate at 3.5GHz. A 0.8 mm thick polyester textile material with a dielectric constant and a loss tangent of 1.9 and 0.0045, respectively, was used as the substrate. The patch, feed line, and ground plane were made from conductive copper tape with a thickness of 0.035 mm. The design employs a microstrip feed line to deliver power to the radiating patch element of the antenna. Initially, using the following set of basic equations, the antenna size was estimated for 3.5 GHz resonance frequency. After that, the antenna design was optimized to a net size of 30 × 20 × 0.8 mm³. A set of rectangular slots on the patch plane and a partial grounding structure were added to improve impedance matching and effectiveness of the antenna.

Width of the patch is $$W_p = \frac{c_0}{2f_r\sqrt{\frac{2}{\epsilon_r+1}}} \quad (1)$$

where c_0= light speed in free space, f_r= resonance frequency, ϵ_r= substrate dielectric constant.

Length is $$L = 0.412h\frac{(\epsilon_{reff}+0.3)\left(\frac{W_p}{h}+0.264\right)}{(\epsilon_{reff}-0.258)\left(\frac{W_p}{h}+0.8\right)} \quad (2)$$

where $$\epsilon_{reff} = \frac{\epsilon_r+1}{2} + \frac{\epsilon_r-1}{2}\left[1 + 12\frac{h}{W}\right]^{-\frac{1}{2}} \quad (3)$$

ϵ_{reff} is effective dielectric constant, h is substrate thickness.

Effective length is $$L_{eff} = \frac{c_0}{2f_r\sqrt{\epsilon_{reff}}} \quad (4)$$

Patch length is $$L_p = L_{eff} - 2\Delta L \quad (5)$$

The optimized parameters of the projected antenna are shown in Table I. The patch is placed on the top surface of the textile substrate. The optimized size of the substrate and patch are 30 mm × 20 mm and 12.65 mm × 14.64 mm, respectively. The antenna comprises a right-angle triangular slot (p = q = 3 mm, r = 4.24 mm) and rectangular slots (Li1= =12.75 mm, Li2=8.75 mm, W1= 2 mm). A microstrip feedline with dimension of 15 mm × 2.58 mm was used to excite the patch. Fig. 1(a) shows the designed antenna's front view while Fig. 1(b) illustrates the rear view.

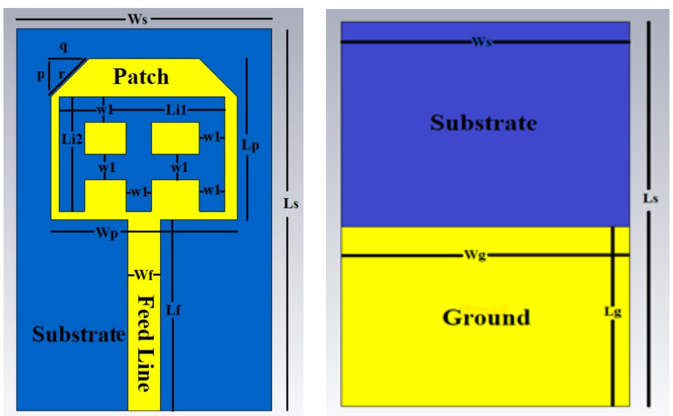

(a) (b)

Fig. 1. (a) front view, (b) rear view of the proposed antenna.

TABLE I
OPTIMIZED OF DESIGN PARAMETERS OF THE PROPOSED ANTENNA

Parameters	Values (mm)
Substrate Width, Ws	20
Substrate Length, Ls	30
Feed Line Length, Lf	15
Feed Line Width, Wf	2.58
Patch Length, Lp	12.65
Patch Width, Wp	14.64
Ground Width, Wg	20
Ground Length, Lg	14
Substrate Height, h	0.8
Li1	12.5
Li2	8.75
W1	2.0
p	3.0
q	3.0
r	4.24

Incorporation of slotting and partial grounding plays a significant role in performance improvement of the antenna. Slotting enhances antenna performance by reshaping current distribution, introducing multiple resonances, improving impedance matching, and boosting radiation efficiency. These mechanisms collectively contribute to wider bandwidth, better efficiency, and more compact designs. On the other hand, partial grounding in antenna design improves performance by optimizing impedance matching, broadening bandwidth, enhancing radiation efficiency, and enabling more compact and versatile structures. It modifies the electromagnetic interaction between the radiator and the ground plane, leading to better control of current distribution and radiation characteristics.

III. ANTENNA FABRICATION AND TESTING

Simulations rely on idealized or estimated values (e.g., dielectric constant, loss tangent) are powerful for initial design, but fabricating and measuring a physical antenna prototype prototypes is essential for validating real-world performance. The proposed antenna was fabricated in the laboratory, and its reflection coefficient (S11) and voltage standing wave ratio (VSWR) are measured under the off-body condition in free space and on different parts of the human body using the vector network analyzer (model: LiteVNA 64). Due to the measuring limitations of the VNA and the absence of an anechoic chamber in the laboratory, the gain, efficiency and radiation pattern of the antenna were not measured. The structure of the fabricated antenna is presented in Fig. 2, whereas Fig. 3 depicts the experimental setup.

(a) (b)

Fig. 2. (a) Front and (b) back view of the fabricated antenna.

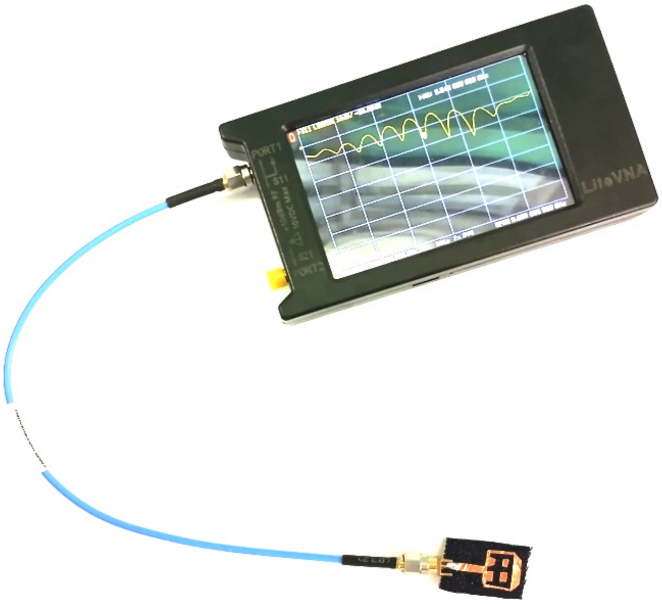

Fig. 3. Setup for measurement.

IV. Results and discussion

A. Off-body Performance Results

1) Reflection Coefficient (S11) and VSWR

A comparison between the simulated and measured reflection coefficient (S11 parameter) and voltage standing wave ration (VSWR) of the proposed antenna is depicted in Fig. 4. The simulation results show that the antenna resonates at ~3.50 GHz. The numerical and experimental resonant peak frequencies of 3.5 GHz and 3.54 GHz are close to each other. The measured resonance peak frequency is ~3.52 GHz, slightly shifted the right from 3.50 GHz. The difference between the two is ~20 MHz, which is less than 1% of the center frequency indicating a very close match and there is strong agreement between the simulation and experimental results. The numerical and measured S11 values are -60.73 dB and -45.42 dB, respectively, indicating the proposed antenna is well matched to the system. Bandwidth is typically defined as the frequency range over which the reflection coefficient (S_{11}) is below −10 dB, meaning less than 10% of the power is reflected. The simulated bandwidth is 1.17 GHz centered around 3.5 GHz, roughly spanning from 3.11 GHz to 4.27 GHz, which covers several key communication bands such as 3.3–3.8 GHz (5G NR (n77, n78) band), 3.1–3.7 GHz (C-Band Radar / WiMAX band), 3.5 GHz (Citizens Broadband Radio Service (CBRS) band), and 4.0–4.2 GHz (Extended C-Band), which are highly relevant for modern wearable broadband applications in smart clothing, sports, and healthcare. The measured bandwidth is slightly broader, extending approximately from 3.35 GHz to 3.65 GHz.

Simulated VSWR minimum value of 0.98 occurred around 3.51 GHz, while measured VSWR minimum value of 1.16 obtained around 3.53 GHz, indicating good impedance matching and the antenna system is highly efficient with minimal signal loss. The close match between simulated and measured VSWR minima and resonance points suggesting accurate simulation modeling, good fabrication and measurement practices, and reliable performance of the device at its intended operating frequency.

Deviations between simulation and measurement results may arise from practical limitations in fabrication, inherent variability in material properties, and differences between idealized simulation boundaries and real-world measurement environments. Minor deviations in slot size, substrate thickness, feed alignment, or soldering can shift resonance, alter impedance, and introduce parasitic effects. Imperfect edges or roughness can interrupt current flow, leading to performance variations. Simulations adopt ideal materials values, but real substrates vary with manufacturing, humidity, and temperature. Small shifts in dielectric constant affect resonance, gain and bandwidth. Simulations assume ideal free-space and matched boundaries, while real tests are affected by fittings, cables, and connectors. Finite ground planes and nearby objects may alter radiation and impedance. Reflections from lab walls, instruments, or people can further distort results compared to simulations.

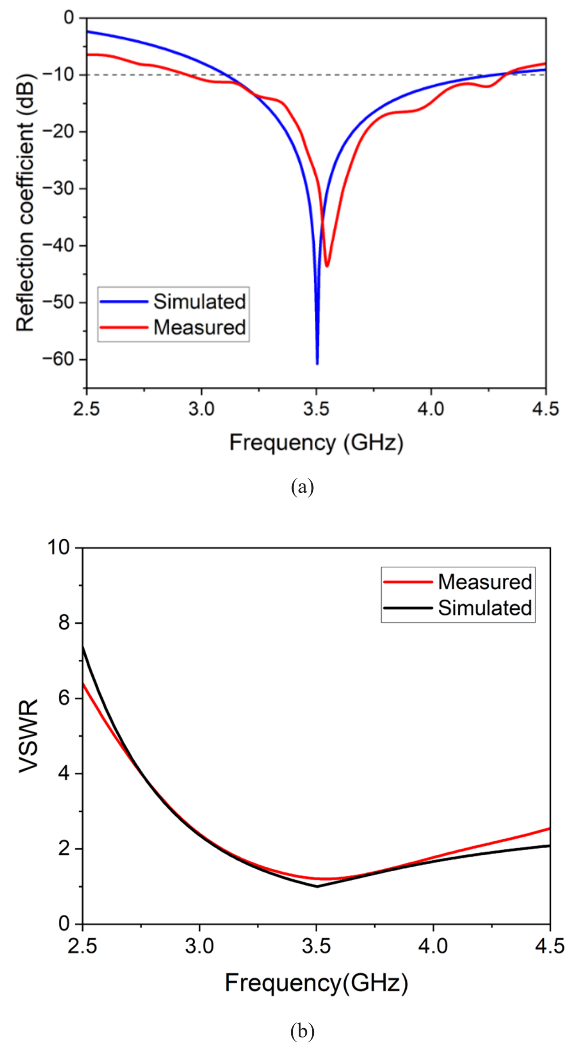

Fig. 4. Simulated and measured (a) S11, (b) VSWR.

2) Gain and Directivity

The three-dimensional (3D) far-field gain and directivity patterns of the proposed antenna at the resonant frequency of 3.5 GHz are depicted in Fig. 5. The color scale represents the magnitude of radiation intensity or gains in different directions. Red/Orange regions represent high radiation intensity or high gain in that direction (main lobes). Blue regions present low radiation intensity or lower gain (nulls or side lobes). The gradient visually maps how energy is distributed spatially around the antenna.

The proposed antenna exhibits a peak gain of 2.59 dBi and a peak directivity of 2.84 dBi. Directivity represents the ideal radiation pattern assuming no losses. Gain reflects the actual radiated power, incorporating losses from dielectric, conductor, and impedance mismatch. The small difference between the peak values (2.84 vs. 2.59 dBi) indicates high radiation efficiency, approximately 91.2%. The small gap between gain and directivity across figures confirms minimal resistive and dielectric losses.

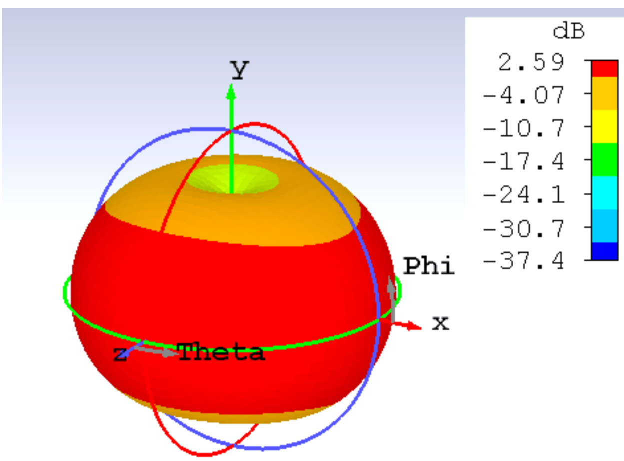

(a)

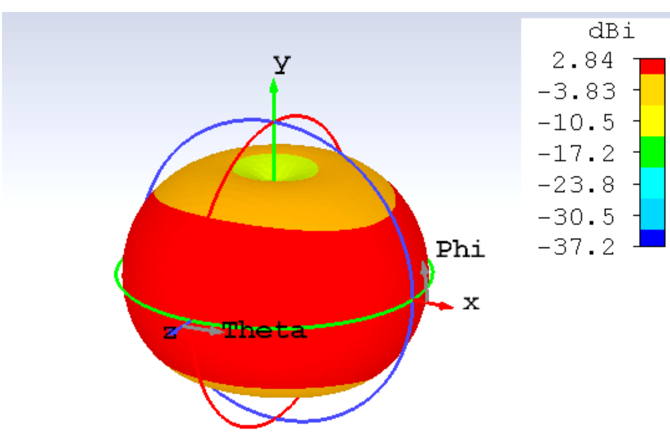

(b)

Fig. 5. 3D farfield gain (a) and directivity (b) at 3.5 GHz.

A 2.59 dBi antenna gain can be adequate for short-range communication or when the antenna is placed in close proximity to the body for on-body communication applications, but its suitability depends on the specific requirements of the system and the environment in which it operates. A directivity of 2.84 dBi can be sufficient for wearable communication applications. It can provide adequate signal strength for short-range, on-body communication.

3) Efficiency

Fig. 6 illustrates the frequency-dependent variation of the radiation efficiency and total efficiency of the designed antenna. At 3.5 GHz, the antenna exhibits a radiation efficiency is 94.54% and total efficiency of 94.52%. The antenna exhibits stable radiation efficiency in the range of 84.52% to 95.84% over the operating frequency range. Accordingly, the proposed antenna demonstrates satisfactory efficiency at its resonant frequency. A radiation efficiency of 94.54% is generally considered very good and more than sufficient for wearable communication applications. A high radiation efficiency means that a large portion of the power fed into the antenna is radiated outwards as an electromagnetic wave, minimizing losses within the antenna itself.

Fig. 5 provides a snapshot of how the antenna radiates energy at 3.5 GHz, showing strong lobes and minimal nulls indicating good directivity and gain. Fig. 6 confirms that this performance is not isolated: the antenna maintains high radiation efficiency across a broad frequency range, peaking near 3.3 GHz, which aligns well with the 3.5 GHz performance in Fig. 5. The efficiency gap between radiation and total efficiency in Fig. 6 mirrors the gain–directivity gap in Fig. 5, reinforcing the interpretation of ~91% efficiency. The antenna is well-optimized around 3.3–3.5 GHz, with high radiation efficiency and strong directional performance.

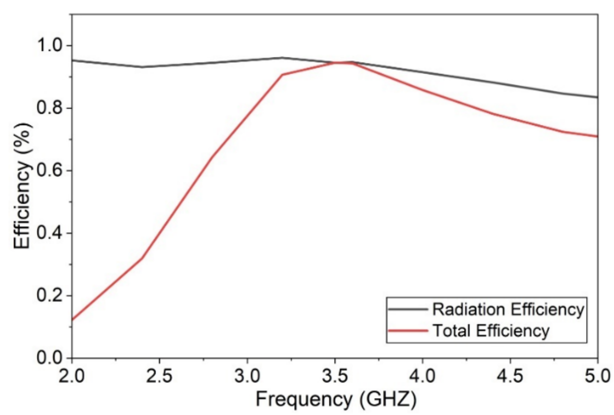

Fig. 6. Efficiency of the proposed antenna.

4) Radiation Pattern

Body-centric environments involve dynamic movements and orientations. Evaluation of E-field patterns at different φ (phi) planes is essential for assessing the angular stability and robustness of wearable antennas. Different φ planes interact differently with the human body's geometry and dielectric properties. Stable E-field patterns across φ planes imply the antenna can maintain performance under body movement, bending, or rotation. Fig. 7 illustrates the simulated electric field (E-field) pattern of the proposed antenna.

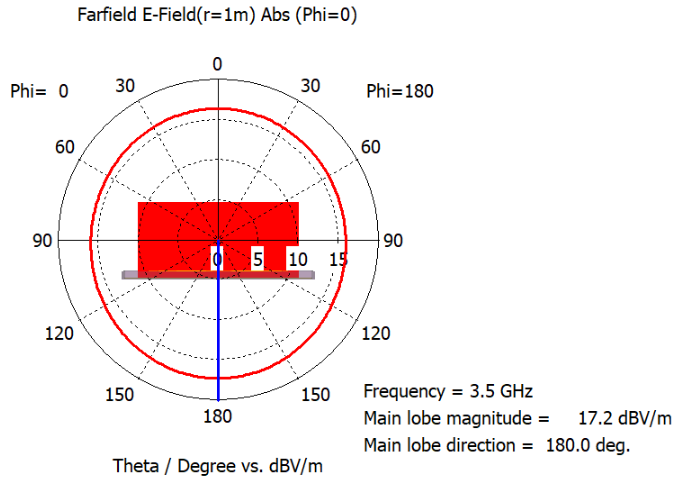

(a)

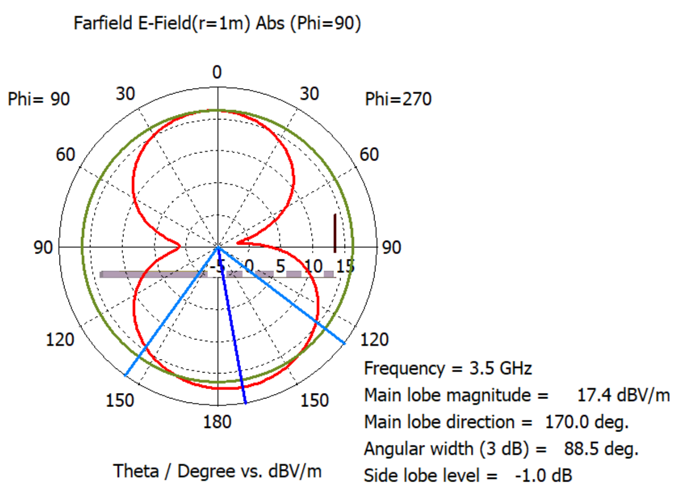

(b)

Fig. 7. Farfield E-field pattern at 3.5 GHz for (a) phi=0, (b) phi=90 degrees.

At the resonant frequency of 3.5 GHz and for φ = 0°, the main lobe magnitude is 17.2 dB V/m, with the main lobe directed at 180°. For φ = 90°, the main lobe magnitude increases slightly to 17.4 dB V/m, maintaining the same direction of 180°. The 3 dB angular beamwidth, and the side-lobe level are 88.5° and -1.0 dB, respectively.

Fig. 5 illustrates the 3D far-field radiation characteristics of the proposed antenna at 3.5 GHz, where the gain and directivity plots exhibit a predominantly spherical radiation envelope, indicating that the antenna radiates energy in multiple directions with relatively uniform intensity. The color-coded surface, mapped in spherical coordinates (Phi, Theta), reveals a quasi-omnidirectional pattern, where the radiated power is distributed broadly across the azimuthal plane with moderate variation in elevation. This pattern is particularly evident in the gain plot, where the absence of sharp nulls and the smooth gradient suggest consistent radiation coverage, making the antenna suitable for applications requiring broad spatial coverage for wireless broadband applications.

5) Surface Current Distribution

Fig. 8 shows the surface current distribution of the proposed textile antenna at 3.5 GHz. The results show that the antenna maintains a clear resonance dip around 3.5 GHz across all bending angles, and S11 lies below –10 dB within the intended operating band, which indicating good impedance matching and stable performance under severe deformation. As the antenna bending angle increases, the resonance peak shifts toward lower frequencies in most cases. These results are consistent with previous studies on bending conditions [19], [20]. The left shift of resonance under bending conditions occurs because with increasing bending angles the antenna's effective electrical length and dielectric loading increase, and lowering the resonant frequency. The antenna's wide bandwidth (1.17 GHz) offers the advantage of even with bending-induced detuning, the antenna covers the target frequency range without performance loss.

Current originates from the microstrip feed line feed and is predominantly distributed across the antenna structure, indicating that the entire antenna actively contributes to resonance at this frequency. The peak surface current density, measured at 85.29 A/m, predominantly accumulates around the lower segment of the feed line and the bottom edges of the patch, as depicted in Fig. 8.

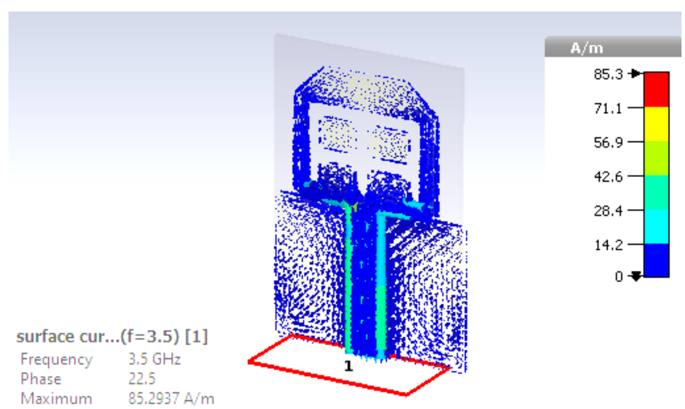

Fig. 8 Surface current distribution at 3.5 GHz.

B. Bending Analysis

Wearable antennas incorporated into garments are not limited to flat configurations; they also undergo mechanical deformations such as bending, stretching, and flexing during regular use [18]. Ten distinct bending situations (from 0° (flat) to 170° (extreme bend)) are chosen for the performance analysis of the proposed antenna. Fig. 9 shows the bended antenna images at four typical bending angles (0°, 30°, 60°, 90°), whereas Fig. 10 presents the S11 versus frequency graphs for all bending angles. As seen, the antenna maintains a clear resonance dip around 3.5 GHz across all bending angles, and S11 lies below –10 dB within the intended operating band, which indicating good impedance matching and stable performance under severe deformation. As the antenna bending angle increases, the resonance peak shifts toward lower frequencies in most cases. These results are consistent with previous studies on bending conditions [19], [20]. The left shift of resonance under bending conditions occurs because with increasing bending angles the antenna's effective electrical length and dielectric loading increase, and lowering the resonant frequency. The antenna's wide bandwidth (1.17 GHz) offers the advantage of even with bending-induced detuning, the antenna covers the target frequency range without performance loss.

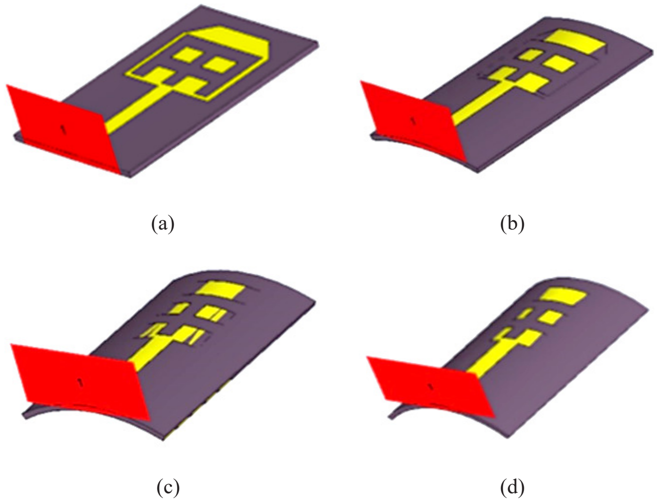

Fig. 9. Typical bent antenna image at 0^0 angle (a), 30^0 angle (b), 60^0 angle (c), and 90^0 angle (d).

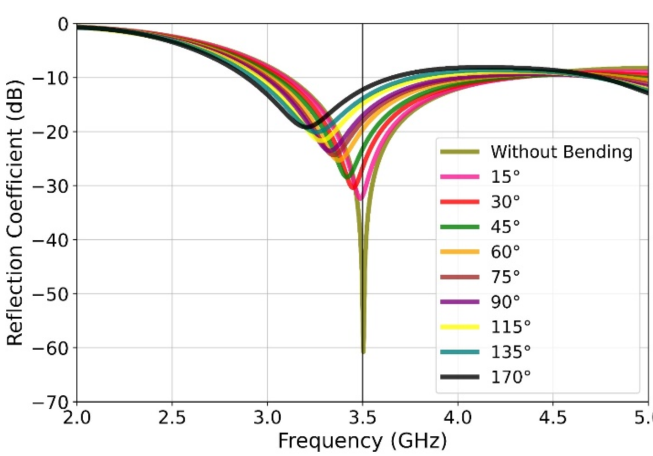

Fig. 10. S11 of the proposed antenna under various bending conditions.

Antenna performance metrics for each bending angle are summarized in Table II. It is observed that as the bending angle increases, radiation efficiency and gain decreases. When an antenna is bent, it typically broadens its radiation pattern in the bending plane, reducing the maximum radiation intensity in the desired direction, which lowers the overall gain [21]. Antenna efficiency decreases with increased bending because the deformation alters the antenna's physical structure, resulting in impedance mismatch, surface wave losses, and frequency shifting. These effects lead to a redistribution of electrical currents and a reduction in the power radiated compared to the power accepted [22]. The table also shows that antenna bandwidth decreases as bending increases. Bending the antenna changes its effective length and the electrical distance between the radiating patch and ground plane, thereby narrowing the frequency range for efficient operation [23].

TABLE II
BENDING ANALYSIS OF THE PROPOSED ANTENNA

Bending angle (degree)	Resonance frequency (GHz)	S11 at resonance (dB)	Bandwidth (GHz)	Radiation Efficiency (%)	Gain (dB)
0	3.50	-60.73	1.17	94.53	2.59
15	3.33	-32.39	1.21	93.36	2.59
30	3.44	-30.40	1.20	92.40	2.48
45	3.42	-28.43	1.19	91.65	2.56
60	3.38	-25.31	1.08	90.94	2.52
75	3.35	-24.32	1.05	90.33	2.49
90	3.33	-23.55	1.01	89.82	2.48
115	3.29	-21.68	0.89	89.05	2.41
135	3.26	-20.09	0.84	88.76	2.36
170	3.20	-19.17	0.76	87.01	2.26

C. Phantom Modeling and On-Body Results

1) 3D Phantom Modeling and Distance Optimization

The close integration of wearable antennas with the human body necessitates careful consideration of antenna–tissue interactions and their influence on key performance metrics. A human body phantom model was used with dimensions of $70 \times 60 \times 8$ mm^3. The phantom consisted of three layers: skin, fat, and muscle tissues with thicknesses of 2 mm, 3 mm, and 10 mm, respectively. Table III shows the electrical characteristics of the three tissue layers at a frequency of 3.5 GHz. The CST Studio Suite was used to create a body phantom model, as shown in Fig. 11(a). The electrical properties of skin, fat, and muscle tissues within the antenna's operating range were derived from the data reported in [24], [25] and are listed in Table III.

TABLE III
ELECTRICAL CHARACTERISTICS OF TISSUE LAYERS

Name of Tissue	Frequency (GHz)	Permi-ttivity (ϵ_r)	Conduc-tivity σ (s/m)	Loss Tangent	Mass density (kg/m^3)
Skin (dry)	3.5	37.005	2.0249	0.28103	1109
Fat	3.5	5.1739	0.15553	0.15439	911
Muscle	3.5	51.444	2.5575	0.25533	1090

To determine the optimum distance, five different separation levels between the antenna and the human body phantom model were evaluated. As shown in Fig. 11(b), when the designed antenna was positioned very near the human body, the S11 values decrease, and the resonance peak shifts toward higher frequencies. This shift may be caused by fringing effects, which alter the effective width of the antenna structure when it comes near the human body. At a separation of 10 mm, the resonant peak was observed at 3.5 GHz. Based on these findings and considering the practical application of positioning the antenna over clothing such as a jacket or suit, rather than directly on the skin a 10 mm gap is identified as the optimal separation distance for this study.

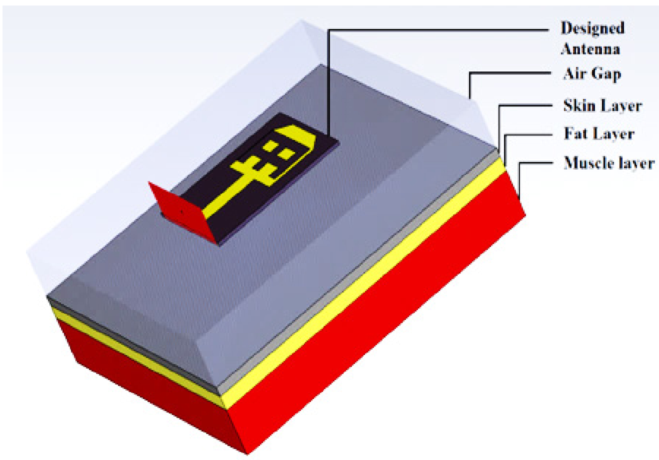

(a)

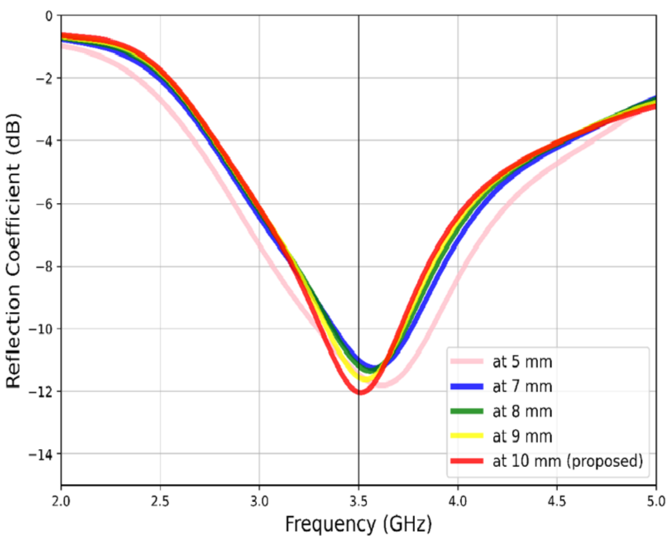

(b)

Fig. 11. On-body performance analysis of the antenna. (a) Three-layer tissue-equivalent phantom model. (b) Simulated S11 response.

2) On-body Simulation and Testing Results

Fig. 11(b) illustrates the reflection coefficient (S11) of the proposed antenna when placed on the human body phantom model with a 10 mm separation. The corresponding on-body performance metrics are presented in Table IV. At the resonant frequency of 3.5 GHz, the S11 value is -12.02 dB, which is lower than that observed under the off-body condition. Nonetheless, it remains well below the -10 dB threshold, indicating satisfactory impedance matching. The increased return loss can be attributed to reactive loading from the body and modifications to the antenna's input impedance caused by fringing effects. Under these on-body conditions, the antenna also sustains a wide bandwidth of 400 MHz. The VSWR at 3.5 GHz is measured at 1.66, further confirming adequate impedance matching.

At 3.5 GHz, the antenna achieves a gain of 2.14 dB, which is slightly lower than the 2.59 dB observed under off-body conditions. This reduction is likely due to electromagnetic energy absorption within the tissue layers of the phantom. A corresponding decrease in efficiency is also observed in the on-body case, consistent with these absorption effects. At 3.5 GHz, the radiation efficiency is measured at 34.06%, while the total efficiency is 36.34%.

TABLE IV
Performance Metrics of Proposed Antenna in On-Body Scenarios

Substrate Material	S11 (dB)	VSWR	Efficiency (%)		Bandwidth (MHz)	Gain (dB)
			Total	Radiation		
Polyester	-12.02	1.66	36.34	34.06	399.2	2.13

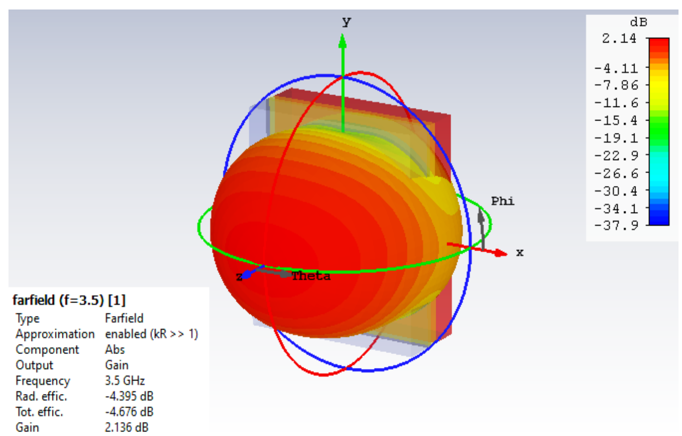

Fig. 12. Radiation pattern of the proposed antenna on phantom at 3.5 GHz.

The simulated 3D radiation pattern of the proposed antenna at 3.5 GHz over the human body phantom model is shown in Fig. 12. This result indicates that the antenna radiates moderately well at 3.5 GHz with a maximum gain of 2.136 dB and a radiation efficiency of -4.395 dB (~36%). The 3D plot shows the spatial distribution of the radiated power, which is mostly uniform but stronger in specific directions (as shown by the red/orange areas). The pattern is nearly spherical and omnidirectional, with the antenna radiating almost equally in many directions, with only slight preference in one direction (indicated by the small red lobe in the pattern). This pattern is suitable for Wi-Fi access points, IoT (Internet of Things) devices, and 5G / LTE small cells devices. Due to the low gain and near-spherical pattern, this antenna is also ideal for small form-factor wearable or embedded devices where consistent coverage in all directions is more important than long-range.

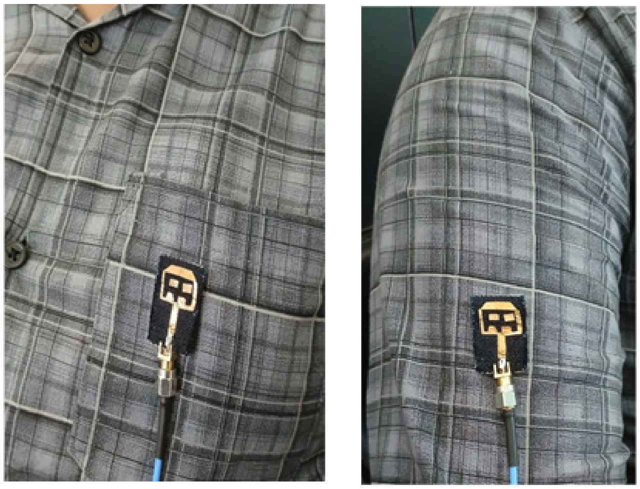

(a) (b)

Fig. 13. Placement of the proposed antenna to the (a) chest and (b) arm regions of the human body.

Fig. 13 illustrates the placement of the proposed antenna on the chest and arm regions of the human body for on-body measurements. The reflection coefficient responses obtained experimentally from various body locations are presented in Fig. 14. In free space, the fabricated antenna exhibited a resonant frequency of 3.54 GHz (Fig. 4). Upon placement on the arm, a downward shift in the resonance frequency to 3.4 GHz was observed, while the center frequency remained stable at 3.5 GHz when positioned on the chest. These results confirm that the proposed textile antenna effectively covers the entire frequency band required for broadband wireless applications.

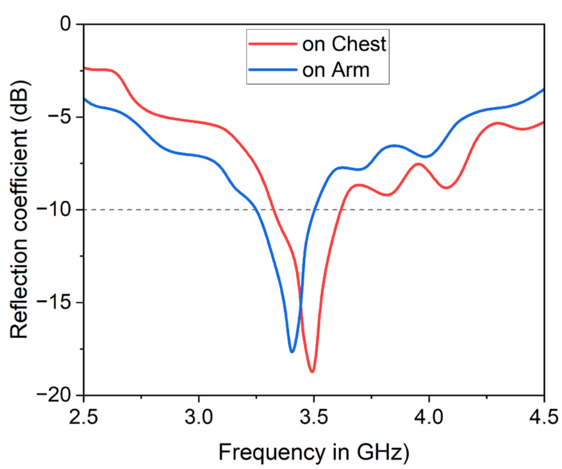

Fig. 14. Measure S11 on chest and arm regions of the human body.

D. SAR Analysis

The Specific Absorption Rate (SAR) quantifies the amount of electromagnetic (EM) energy absorbed per unit mass of human tissue. For wearable applications, it is essential to ensure that radiation from the designed antenna directed toward the human body remains within safe limits. According to regulatory standards, the maximum permissible SAR limit is 1.6 W/kg averaged over 1 gm of tissue, as defined by the U.S. Federal Communications Commission (FCC), and 2 W/kg averaged over 10 gm of tissue, as specified by the International Commission on Non-Ionizing Radiation Protection (ICNIRP).

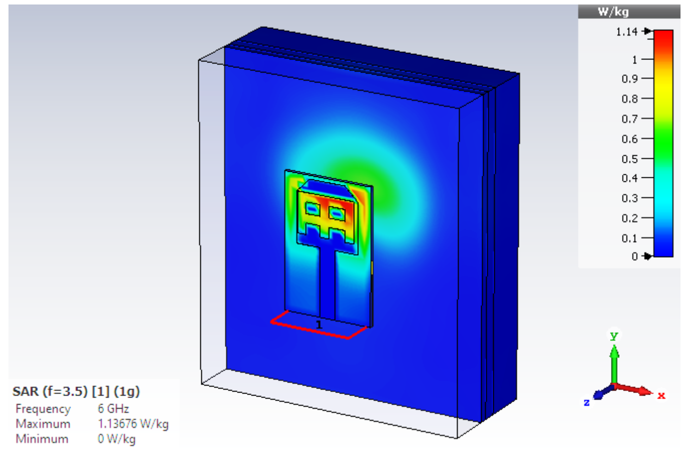

(a)

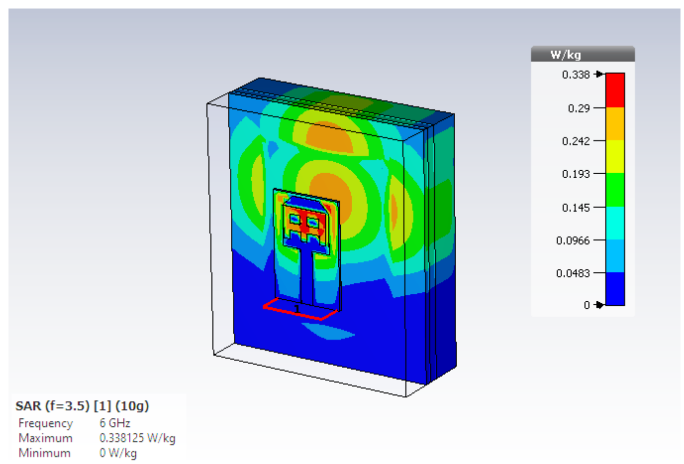

(b)

Fig. 15. SAR analysis over 1 gm (a) and 10 gm (b) of tissue for the body phantom model at 3.5 GHz.

In this work, SAR values were evaluated using a three-layer flat body phantom model, considering both 1 g and 10 g of tissue. An input power of 500 mW was applied in CST simulations to assess SAR performance at the operating frequency of 3.5 GHz. The resulting SAR values, shown in Fig. 15, are 1.137 W/kg for 1 g and 0.338 W/kg for 10 g of tissue. Both values are well below the safety thresholds established by the FCC, confirming the antenna's compliance with human exposure standards.

Although the typical power levels lie within 10-100mW in wearable devices, in the present SAR study a higher input power (500 mW) is used to simulate worst-case exposure conditions. It helps to ensure that even under extreme usage, the antenna remains within safety limits. It also ensures that even if the antenna operates above its intended power due to malfunction or environmental factors, it won't exceed SAR safety thresholds [26], [27].

V. Comparative Studies

A comparison of various performance metrics of the proposed antenna with other existing antennas published in earlier studies is provided in Table V. The present work with antenna size 30×20×0.8 mm³ achieves a compact footprint, smaller than most references, making it more suitable for integration into textiles. Polyester substrate is used in this work, which is flexible, durable, comfort and textile-compatible, unlike Paper or Kapton substrates used in some references. This work offers the largest bandwidth 1.17 GHz (covers 3.11 – 4.27 GHz), which is wider than reported values (≤0.6 GHz) in references [15], [28]-[31], ensuring multi-band operation. The antenna provides nearly 2.7 times wider bandwidth than average indicating robust against detuning from bending/stretching. This work achieves gain of 2.59 dB, which is nearly 1.8 dB higher than the average of references (~0.8 dB), ensuring stronger radiation performance and indicating stronger link margin for wearable communication. With 94.52% efficiency, this work is among the highest reported, only slightly below the reference [31] (99.5%), but significantly better than most others.

The radiation efficiency is nearly 11% higher than average indicating reliable radiation in textile environments. This work shows SAR values of 1.134 W/kg (1g) and 0.338 W/kg (10g), which are within IEEE/FCC safety limits (<1.6 W/kg for 1g) for body-worn devices, and comparable to other wearable designs. It balances safety with performance, indicating suitable for body-worn applications. This Work achieves the best balance of bandwidth, efficiency, and robustness, making it ideal for smart clothing applications where flexibility, safety, and reliable performance are essential.

Hence the present polyester flexible patch antenna is more robust than the references because it combines wider bandwidth, higher efficiency, moderate gain, and stable performance under bending, while maintaining safe SAR levels and a compact textile-compatible design. This robustness directly translates into superior suitability for smart clothing applications, where antennas must remain reliable under bending, stretching, and daily wear conditions.

TABLE V
Performance Comparison of the Proposed Antenna with the Previous Work at 3.5 GHz Band

Design Parameter	Reference No.						
	[15]	[16]	[28]	[29]	[30]	[31]	This Work
Antenna Size (mm³)	30× 30× 1.6	40× 40× 0.44	70× 70× 2.1	40× 77× 0.6	60× 60× 1.17	27.4× 15.6× 0.125	30× 20× 0.8
Substrate/ Permittivity	Jeans/ Denim/ 1.7/ 1.67	Photo Paper/ 3.2	Felt/ 1.634	Denim/ 1.78	Denim/ 1.78	Kapton HN/ 3.4	Polyester/ 1.9
Operating Range (GHz)	3.15 – 3.95	3.33– 3.75	3.46– 3.76	~3.4 – 4.0	2.2 –4.0	3.26– 3.80	3.11 – 4.27
Bandwidth (GHz)	0.540	—	0.3	0.6	0.19	0.545	1.17
Gain (dB)	—	1.4	0.3	3	−2.81	2.07	2.59
Efficiency (%)	—	70	—	~80	—	99.5	94.52
SAR (W/Kg)	—	—	0.57 (1g)	1.03 (1g)/ 0.92 (10g)	0.11 (1g)/ 0.33 (10g)	—	1.134 (1g) 0.338 (10g)

VI. Conclusion

In this work, a compact polyester substrate-based textile microstrip patch antenna operating in the 3.5 GHz band has been successfully designed, fabricated, and validated for next-generation wearable broadband applications. By addressing all critical aspects—including off-body performance, fabrication, testing, on-body evaluation, bending analysis, and SAR assessment—the study provides a comprehensive framework that has been largely absent in prior research. The proposed antenna demonstrates wide bandwidth, high radiation efficiency, and stable performance under bending conditions, while maintaining compliance with IEEE SAR safety standards. Covering multiple bands such as 5G NR (n77, n78), C-Band, CBRS, and extended C-Bands, the antenna proves to be robust, cost-effective, and well-suited for integration into smart clothing. Overall, this work establishes polyester textile antennas as a promising solution for wearable wireless systems, combining practicality, safety, and reliable performance in real-world scenarios.

In experimental work, a single antenna sample was fabricated and experimentally tested. The presented results are based on one measurement, which provides an initial validation of the design concept. While these findings demonstrate the feasibility and performance of the proposed antenna, a statistical analysis across multiple fabricated samples and repeated measurements has not yet been conducted. Future studies will focus on fabricating additional prototypes and performing repeated measurements to assess reproducibility, quantify measurement uncertainty, and establish statistical reliability in the reported performance. Additionally, the antenna's gain, efficiency, and radiation pattern will be measured in an anechoic chamber to provide further experimental validation. Long-term durability tests—such as repeated bending and washing cycles under sustained mechanical stress—will also be conducted to reinforce the claims of suitability for smart clothing applications.

References

[1] S. K. Koul, R. Bharadwaj, "Introduction to Body Centric Wireless Communication," *Wearable Antennas and Body Centric Communication*," Lecture Notes in Electrical Engineering, vol 787, Springer, Singapore, 2021, DOI: 10.1007/978-981-16-3973-9_1.

[2] A. Alemaryeen and S. Noghanian, "On-Body Low-Profile Textile Antenna with Artificial Magnetic Conductor," *IEEE Transactions on Antennas and*

Propagation, vol. 67, no. 6, pp. 3649-3656, June 2019, DOI: 10.1109/TAP.2019.2902632.

[3] R. K. Singh, A. Michel, P. Nepa, A. Salvatore, M. Terraroli and P. Perego, "Compact and Wearable Yagi-Like Textile Antennas for Near-Field UHF-RFID Readers," *IEEE Transactions on Antennas and Propagation*, vol. 69, no. 3, pp. 1324-1333, March 2021, DOI: 10.1109/TAP.2020.3030944.

[4] N.I. Zaidi, N.H.A. Rahman, M.F. Yahya, M.S.A. Nordin, S. Subahir, Y. Yamada, A. Majumdar, "Analysis on Bending Performance of the Electro-Textile Antennas with Bandwidth Enhancement for Wearable Tracking Application," *IEEE Access*, vol. 10, pp. 31800-31820, 2022, DOI: 10.1109/ACCESS.2022.3160825.

[5] F.F. Hashim, W.N.L.B. Mahadi, T.B.A. Latef, M. Bin Othman, "Key Factors in the Implementation of Wearable Antennas for WBNs and ISM Applications: A Review WBNs and ISM Applications: A Review," *Electronics*, vol. 11, no. 15, pp. 2470, August 2022, DOI: 10.3390/electronics11152470.

[6] E. Çelenk and N.T. Tokan, "All-Textile On-Body Antenna for Military Applications," *IEEE Antennas and Wireless Propagation Letters*, vol. 21, no. 5, pp. 1065-1069, May 2022, DOI: 10.1109/LAWP.2022.3159301.

[7] C.G. Bartone, L. Moore, M. Kohli, "An e-textile antenna for body area network," *Proceedings of the 2016 IEEE International Symposium on Antennas and Propagation (APSURSI)*, Fajardo, PR, USA, 26 June 2016–1 July 2016; pp. 999–1000, DOI: 10.1109/APS.2016.7696208.

[8] S. Khan, V. K. Singh, B. Naresh, "Textile antenna using jeans substrate for wireless communication application," *Int. J. Eng. Tech. Sci. Res.,* 2015, 2, 176–181, [Online] Available: www.ijestr.com

[9] A.W. Memon, I.L. Depaula, B. Malengier, S. Vasile, P. Van Torre, L. Van Langenhove, "Breathable Textile Rectangular Ring Microstrip Patch Antenna at 2.45 GHz for Wearable Applications," *Sensors*, vol. 21, no. 5, pp. 1635, 2021, DOI: 10.3390/s21051635.

[10] G. Mollah, K. Shikder and F. Arifin, "Design and Evaluation of a SWB Decagonal Patch Textile Antenna for WBAN Applications," *IEEE Region 10 Symposium (TENSYMP)*, Dhaka, Bangladesh, 2020, pp. 1420-1423, DOI: 10.1109/TENSYMP50017.2020.9230812.

[11] D.-G.Kang, J. Tak, J. Choi, "MIMO Antenna with High Isolation for WBAN Applications," *Int. J. Antennas Propag.*, vol. 2015, Article ID: 370763, pp. 1-7, 2015, DOI: 10.1155/2015/370763.

[12] K. Ali, S. Ali, H. R. Chowdhury, A. Ahmed, "Design and performance analysis of a textile antenna suitable for smart clothing," *IEEE Region 10 Humanitarian Technology Conference (R10-HTC)*, Dhaka, Bangladesh, 2017, pp. 367-370, DOI: 10.1109/R10-HTC.2017.8288976.

[13] L. Zhou, S. Fang and X. Jia, "Dual-band and dual-polarised circular patch textile antenna for on-/off-body WBAN applications," *IET Microwaves*, Antennas & Propagation Volume 14, Issue 7, February 2020, DOI: 10.1049/iet-map.2019.1073.

F.A Tahir, A. Javed, "A compact dual-band frequency reconfigurable textile antenna for wearable applications," *Microw Opt Technol Lett.*, vol. 57, no. 10, pp. 2251–2257, 2015; DOI:10.1002/mop.29311.

[14] V. Kavitha, K. Malaisamy, T.S. Murugesh and M. S. Kumar, "Design and development of jeans textile antenna for wireless broadband applications," *Journal of Industrial Textile*, Vol. 53, pp. 1–13, December 6, 2023, DOI: 10.1177/15280837231215374.

[15] A.K. Singh, S. K. Mahto, R. Sinha, M. Alibakhshikenari, A. J. A. Al-Gburi, A. Ahmad, L. Kouhalvandi, B.S. Virdee, and M. Dalarsson, "Low-Loss Paper-Substrate Triple-Band-Frequency Reconfigurable Microstrip Antenna for Sub-7 GHz Applications," *Sensors*, 23, 8996, November 2023, DOI:10.3390/s23218996.

[16] M. M. Hasan, and A.Z.M.T. Islam, "A Wideband Compact Flexible Patch Antenna Design on Polydimethylsiloxane (PDMS) for Wearable Technology," *Cureus J Eng*, Vol. 2, es44388-025-04462-7, April 2025, DOI:10.7759/s44388-025-04462-7.

[17] D. Ferreira, P. Pires, R. Rodrigues, and R. F. S. Caldeirinha, "Wearable textile antennas: examining the effect of bending on their performance," *IEEE Antennas and Propagation Magazine*, vol. 59, no. 3, pp. 54–59, 2017, DOI: 10.1109/MAP.2017.2686093.

[18] A. Mersani, L. Osman, and J. M. Ribero, "Effect of bending on the characteristics of a Coplanar Textile Antenna," *Proc. of 18th Mediterranean Microwave Symposium MMS*, pp. 255-257, 2018, DOI: 10.1109/MMS.2018.8612049.

[19] S. M. Salleh, M. F. Ain, Z. Ahmad, I.S.Z. Abadin, and C.M.N.C. Isa, "Development of Stretchable and bendable polymer wearable antenna for 5G Applications," *Express Polymer Letters*, Vol. 16, No. 12, pp. 1267-1279, Nov. 12, 2022, DOI: 10.3144/expresspolymlett.2022.92.

[20] Y. Mukai, V.T. Bharambe, J.J. Adams, and M. Suh, "Effect of bending and padding on the electromagnetic performance of a laser-cut fabric patch antenna," *Textile Research Journal*, 2019;89(14):2789-2801, DOI: 10.1177/004051751880120.

[21] P. Salonen, M. Keskilammi and Y. Rahmat-Samii, "Textile antennas: Effect of antenna bending on radiation pattern and efficiency," *IEEE Antennas and Propagation Society International Symposium*, San Diego, CA, USA, 2008, pp. 1-4, DOI: 10.1109/APS.2008.4619343.

[22] N. A. Elias, N. A. Samsuri, M. K. A. Rahim, C. Panagamuwa, and W. Whittow, "Bending and crumpling deformation study of the resonant characteristic and SAR for a 2.4 GHz textile antenna," *J. Teknol.*, vol. 177, no. 10, 2015, DOI: 10.11113/jt.v77.6278.

[23] P. A. Hasgall, F. Di Gennaro, C. Baumgartner, E. Neufeld, B. Lloyd, M. C. Gosselin, D. Payne, A. Klingenböck, and N. Kuster, *IT'IS Database for thermal and electromagnetic parameters of biological tissues*, Version 4.1, Feb. 22, 2022, DOI: 10.13099/VIP21000-05-0.

[24] D. Andreuccetti, R.Fossi and C.Petrucci, "An Internet resource for the calculation of the dielectric properties of body tissues in the frequency range 10 Hz - 100 GHz," *IFAC-CNR*, Florence (Italy), 1997. Based on data published by C.Gabriel et al. in 1996. [Online]. Available: http://niremf.ifac.cnr.it/tissprop/.

[25] J. C. Wang, E. G. Lim, M. Leach, Z. Wang and K. L. Man, "Review of SAR Measurement Methods in Relation to Wearable Devices," *Engineering Letters*, vol. 24, no. 3, 2016, DOI: 10.1063/5.0206045.

[26] P. Zradziński, J. Karpowicz, K. Gryz, "The Parametrization of Electromagnetic Emissions and Hazards from a Wearable Device for Wireless Information Transfer with a 2.45 GHz ISM Band Antenna," *Appl. Sci.*, vol. 15, no. 12, 2025, 6602, DOI: 10.3390/app15126602.

[27] S. Bhattacharjee and M. Mitra, "Triple Band Compact Textile Antenna Structure for Wearable Applications," *Progress In Electromagnetics Research C*, Vol. 144, 1-8, 2024, DOI:10.2528/PIERC24031306.

[28] M. A. Abdelghany, M. I. Ahmed, A. A. Ibrahim, A. Desai and M. F. Ahmed, "Textile Antenna with Dual Bands and SAR Measurements for Wearable Communication," *Electronics*, 13 (12), 2251, 2024, DOI: 10.3390/electronics13122251.

[29] H. Li, J. Du, X. -X. Yang and S. Gao, "Low-Profile All-Textile Multiband Microstrip Circular Patch Antenna for WBAN Applications," *IEEE Antennas and Wireless Propagation Letters*, vol. 21, no. 4, pp. 779-783, April 2022, DOI: 10.1109/LAWP.2022.3146435.

[30] Z. Hossain, A. K. M., N. B. Hassim, S. M. K. Azam, M. S. Islam, and M. K. Hasan, "A planar antenna on flexible substrate for future 5G energy harvesting in Malaysia," *International Journal of Advanced Computer Science and Applications (IJACSA)*, Vol. 11, No. 10, 2020, DOI: 10.14569/IJACSA.2020.0111020.

In Memoriam: Prof. Milić Stojić (1940–2026)

Branko Dokić

In Memoriam
DOI: 10.53314/ELS2630050D

ON the last day of February 2026, Prof. Milić Stojić, a long-standing member of the Editorial Board of the *Electronics* journal, passed away. During the first few years following the establishment of the journal in 1997, he encouraged many authors of the best papers presented at the regional conferences to publish their work in the journal. He served as Guest Editor for Vol. 2, No. 1. He also recommended distinguished international scientists to contribute invited papers, which significantly helped the journal gain recognition relatively quickly, at first throughout the region of the former Yugoslavia and subsequently around the world.

On the occasion of Prof. Milić Stojić's 70th birthday, we dedicated Vol. 15, No. 1 of the journal to him. In that issue, we published his biography, which we provide here in a slightly modified form.

Milić Stojić, Full Professor in Electrical Engineering, University of Belgrade, was born in February 27, 1940 in Užice. He completed his elementary and grammar school in Užice. In the academic 1958/59 year he enrolled the Faculty of Electrical Engineering, University of Belgrade, where he graduated in January 1963. In 1962 he spent two months in London at *Telephone and Cables Company* under the IASTE (International Association of the Exchange of Students in Technical Experience). In October 1963, he enrolled the postgraduate studies at the Electrical Engineering Faculty, where he obtained his M.Sc. degree by defending his M.Sc. thesis entitled *An Approach to Solving the Sensitivity Problem in Control Systems*.

From the University of Belgrade, he obtained his Ph.D. degree in 1967 with the thesis entitled *Analysis and Design of Nonlinear Control Systems Utilizing the Algebraic Criteria of Asymptotic Stability* defended also at the Faculty of Electrical Engineering. The main results of the Ph.D. thesis were published in 1969 in two long papers in the renowned scientific journal *Avtomatica and Telemekhanika*, edited by the Soviet Academy of Science and later published in the USA. as a cover-to-cover English translation in *Automation and Remote Control*. An abridged version of the thesis was also published in Russian as a monograph, edited by the *Publications of Electrical Engineering Faculty* in Belgrade.

After graduation, from February to October 1963, he was with the Institute for Nuclear Science in Vinča, Belgrade. Since October 1963, he is with the Faculty of Electrical Engineering, University of Belgrade, where he has been promoted to the academic positions Teaching Assistant, Assistant Professor, Associate Professor, and Full Professor in 1963, 1969, 1975, and 1980, respectively. He taught courses in automatic control at the undergraduate and postgraduate studies at the electrical engineering faculties of universities in Belgrade, Niš, Banja Luka, and East Sarajevo (Republic of Srpska), at the Faculty of Technical Science in Novi Sad and at the faculties of Mechanical Engineering in Belgrade and Kragujevac. For thirty eight academic years he taught exceptional courses at the High Military Academy in Žarkovo (Belgrade). In 1980, 1984, and 1988, he spent several months at the Physics Department, University of Birmingham (UK), within a joint research program. He delivered numerous invited lectures at the conferences, universities, and scientific institutes in former Yugoslavia and abroad: at the Manchester University (UK), Moscow Aviation Institute, and Institute of Control Science (Moscow). He also delivered lectures at the *Autumn School in Computational Intelligence and Information Technologies* held at the Faculty of Electronics in Niš.

At the Faculty of Electrical Engineering, in three two-year election periods he was the head of the Department of Automation and in two four-year election period he was the head of the Division of Electronics, Telecommunication, and Automation. In one four-year election period, he was the head of the Council of Donor Services at the Republic Assembly of Science. Over ten years he was the head of the Council of Experts in Electrical Engineering at the University of Belgrade. In one four-year election period, he was the member of Administrative Committee of the Institute for

Nuclear Science "Vinča".

As a head of the Program Committee, he organized over 20 conferences of the Yugoslav Society of ETAN (Electronics, Telecommunication, Automation and Nuclear Science), at different centers all over former Yugoslavia. At the beginning of civil war in Yugoslavia in 1991, the ETAN ended his existence. Then, Prof. Stojić founded the new Society of ETRAN (Electronics, Telecommunication, Computers, Automation and Nuclear Science) as a successor of the previous Society of ETAN. In two four-year election periods, from 1992 to 2001, he was the president of ETRAN. Later, he will also become an honorary member of the ETRAN Presidency. He was a full member of the Serbian Scientific Society and up to 2002 he was the secretary of its Technical Department. Prof. Stojić was also the full member of the Engineering Academy of Serbia.

Prof. Stojić was an Associate Editor of *Automatica*, the Journal of IFAC (International Federation of Automatic Control) and the Editor-in-Chief of *Publications of Electrical Engineering Faculty*, Series: *Electronics, Telecommunication, and Automation*, the journal of Electrical Engineering Faculty in Belgrade. At the same time, as he was the secretary of the Serbian Scientific Society, he was the Editor-in-Chief of its journal *Scientific Review: Science and Engineering*. He was also a member of the Editorial Boards of *Facta Universitatis*, Series: *Electronics and Energetics*, journal of University of Niš, *Tehnika, Vojnotehnički Glasnik*, and a Guest Editor of *Electronics*, journal of the Electrical Engineering Faculty in Banja Luka (Republic of Srpska).

For his outstanding merits in the fields of science, education, and results achieved in education of professionals and scientists, he was awarded with the Gold Wreath Labor Medal, Charter of Medallion of University of Niš, and Great Charter and Medallion of ETRAN.

There are many awards that Prof. Stojić received for his outstanding scientific and professional contributions in his papers published in scientific journals or presented at international and domestic conferences. For these activities he also received a number of prizes: October Reward of the City of Belgrade for mathematics and technical science, Award of the International Conference of IFIP (International Federation of Information Processing), together with Prof. Stanoje Bingulac, for the best paper presented at the conference, three awards "Prof. Dušan Mitrović"for the best papers presented at the ETRAN conferences. Together with Prof. Slobodan Vukosavić, he received the Award "Prof. Branko Raković"for the best papers published in international scientific journals.

Prof. Stojić was very active in cooperation with other faculties, institutes, and professional organizations (Electronic Faculty of Niš, JUREMA in Zagreb, High Military School in Belgrade, Institute of Nuclear Science in Belgrade, ETRAN, TELSIKS, INDEL, INFOTEX, etc.) from which he obtained a number of charters, medallions, and letters of thanks.

The main scientific contributions of Prof. Stojić cover the topics of the stability theory, sensitivity analysis of dynamic systems, system simulation, and microcomputer-based real-time control of electrical drives and industrial processes. He published two textbooks; he was author/co-author of two monograph in Serbian, co-author of one monograph in English, and author of one monograph in Russian. He published 194 scientific papers, among them 26 in renowned international journals: *IEEE Transactions on Automatic Control*, *Avtomatika i Telemekhanika*, edited by the Academy of Science USSR, *International Journal on Circuit Theory and Applications*, *Automatica*, *International Journal of IFAC*, *International Journal on System Science*, *IEEE Transactions on Industrial Electronics*, *IEEE Transactions on Power Electronics*, *IEEE Transactions on Education*, and *Facta Universitatis*, Series: *Electronics and Energetics*. Other papers have been published in domestic journals (40), in the proceedings of conferences in Yugoslavia (94), and in the proceedings of international conferences (34). Several hundred times he has been cited in the papers, books, M.SC and Ph.D thesis of Yugoslav authors.

He was the author of the books *Continuous Control Systems* (ten editions) and *Digital Control Systems* (five editions), which are used as standard textbooks of automatic control at the universities of Yugoslavia. Although the textbooks are written in Serbian, they were reviewed in the Russian Reporting Journal *New Books in Abroad*, issued by the Soviet Academy of Science, by Prof. Yakov Zalmanovich Tsypkin. In the review, Prof. Tsypkin wrote: "This book is distinguished by clear and laconic expressivity".

Prof. Stojić gave numerous technical solutions within projects carried out by the Faculty of Electrical Engineering for needs of the industry, scientific institutes, and Yugoslav Army. In three five-year fiscal periods he headed the strategic project *Electronic Systems of Measuring and Control* supported by the Ministry of Science and Technology of Serbia. He designed the Laboratory of Automatic Control at the Faculty of Electrical Engineering. Together with Prof. Dejan Živković, he designed the Laboratory of Control Systems in the Air Force at the High Military School in Žarkovo (Belgrade). For the project of electronic simulator of guided missile, he was awarded the Yugoslav Decoration for Military Merits, and for the project of microprocessor-based positioning servomechanism with induction motor he obtained, together with Prof. Slobodan Vukosavić, Tesla's Award for the prominent scientific and professional merit.

He supervised over 20 M.Sc. and 16 Ph.D. theses (12 of them at the Faculty of Electrical Engineering in Belgrade and one each at the electrical engineering faculties in Niš and Zagreb, Technical Faculty in Čačak, and Faculty of Mechanical Engineering in Kragujevac).

Finally, we would like to express our sincere gratitude to Prof. Milić Stojić for his invaluable contribution to the advancement and recognition of the *Electronics* journal. Building upon the foundations that we established together with him, the journal has achieved its current level of visibility and standing. For this reason, his legacy will be remembered for many years to come.

Preparation of Papers for Electronics (September 2011)

First A. Author, Second B. Author, and Third C. Author

***Abstract*—These instructions give you guidelines for preparing papers for ELECTRONICS journal. Use this document as a template if you are using Microsoft *Word* 6.0 or later. Otherwise, use this document as an instruction set. The electronic file of your paper will be formatted further. Define all symbols used in the abstract. Do not cite references in the abstract. Do not delete the blank line immediately above the abstract; it sets the footnote at the bottom of this column.**

***Index Terms*—About four key words or phrases in alphabetical order, separated by commas.**

Paper Classification
DOI: 10.7251/ELSxxxxxxxx

I. Introduction

THIS document is a template for Microsoft *Word* versions 6.0 or later.

When you open the file, select “Page Layout” from the “View” menu in the menu bar (View | Page Layout), which allows you to see the footnotes. Then, type over sections of file or cut and paste from another document and use markup styles. The pull-down style menu is at the left of the Formatting Toolbar at the top of your *Word* window (for example, the style at this point in the document is “Text”). Highlight a section that you want to designate with a certain style, then select the appropriate name on the style menu. The style will adjust your fonts and line spacing. **Do not change the font sizes or line spacing to squeeze more text into a limited number of pages.** Use italics for emphasis; do not underline. The length of the manuscript is limited to the maximum of 15 pages.

To insert images in *Word,* position the cursor at the insertion point and either use Insert | Picture | From File or copy the image to the Windows clipboard and then Edit | Paste Special | Picture (with “float over text” unchecked).

We will do the final formatting of your paper.

II. Procedure for Paper Submission

A. Review Stage

The manuscripts are to be submitted using the Electronics Journal online submission system – accessible from Journal’s homepage. Prepare it in two-column format as shown in this template. Place all figures and tables at the end of the paper (after the references) on separate page(s). Figures and tables must have the same caption names as referenced in the text. Only PDF format of the manuscript is allowed at the review stage. Please, check if all fonts are embedded and subset and that the quality of diagrams, illustrations, and graphics is satisfactory. Failing to provide above listed requirements is a valid reason for rejection.

B. Final Stage

When you submit your final version (after your paper has been accepted), prepare it in two-column format, including figures and tables in accordance with this template. Pack all of your files (manuscript source file in *Word*, figures, and manuscript PDF form) within one archive file (you may use any of the available file compression tools: *WinZip*, *WinRAR*, *7-Zip*, etc.). Do not forget to provide the manuscript converted in PDF format that will be used as a reference for final formatting of your paper. Figures should be named as referenced in the manuscript (e.g. *fig1.eps*, *fig2.tif*, etc.)

C. Figures and Tables

Format and save your graphic images using a suitable graphics processing program and adjusts the resolution settings. We accept images in the following formats: PS, EPS, TIFF, GIF, and PNG. Additionally, it is allowed to use images generated by using one of the following software tools: Microsoft Word, Microsoft PowerPoint, or Microsoft Excel. The resolution of a RGB color file should be 400 dpi. Please note that JPG and other lossy-compressed image formats are not allowed. Use available software tools to convert these images to appropriate format.

Image quality is very important to how yours graphics will reproduce. Even though we can accept graphics in many formats, we cannot improve your graphics if they are poor quality when we receive them. If your graphic looks low in

Manuscript received 15 September 2011 (write the date when you have first sent the manuscript for review). Received in revised form 20 October 2011 (write the date when you have sent the manuscript in its revised form if revisions required for your paper after review).

(Place here any sponsor and financial support acknowledgments).

F. A. Author is with the Faculty of Electrical Engineering, University of Banja Luka, Banja Luka, Bosnia and Herzegovina (corresponding author to provide phone: +387-51-222-333; fax: +387-51-111-222; e-mail: author@etfbl.net).

S. B. Author was with Faculty of Technical Sciences, University of Novi Sad, Novi Sad, Serbia. He is now with the Institute “Mihailo Pupin”, Belgrade, Serbia (e-mail: author@pupin.rs).

T. C. Author is with the School of Electrical Engineering, University of Belgrade, Belgrade, Serbia, on leave from the Faculty of Electronic Engineering, University of Niš, Niš, Serbia (e-mail: author@elfak.ni.ac.rs).

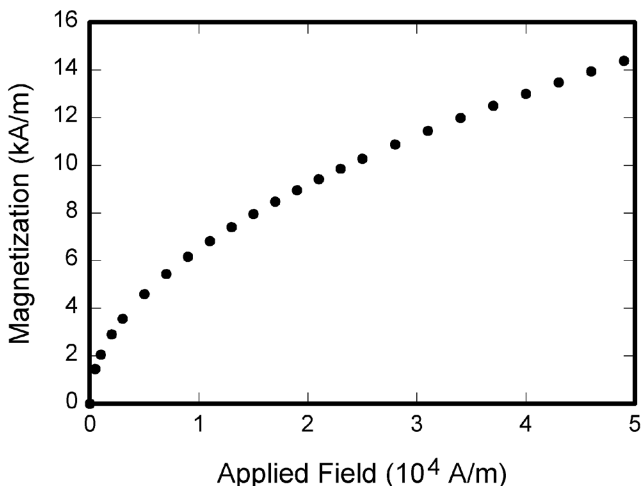

Fig. 1. Magnetization as a function of applied field. Note that "Fig." is abbreviated. There is a period after the figure number, followed by two spaces. It is good practice to explain the significance of the figure in the caption.

quality on your printer or monitor, please keep in mind that cannot improve the quality after submission.

If you are importing your graphics into this Word template, please use the following steps:

Under the option EDIT select PASTE SPECIAL. A dialog box will open, select paste picture, then click OK. Your figure should now be in the Word Document.

If you are preparing images in TIFF, EPS, or PS format, note the following. High-contrast line figures and tables should be prepared with 600 dpi resolution and saved with no compression, 1 bit per pixel (monochrome).

Photographs and grayscale figures should be prepared with 300 dpi resolution and saved with no compression, 8 bits per pixel (grayscale).

Most charts graphs and tables are one column wide (3 1/2 inches or 21 picas) or two-column width (7 1/16 inches, 43 picas wide). We recommend that you avoid sizing figures less than one column wide, as extreme enlargements may distort your images and result in poor reproduction. Therefore, it is better if the image is slightly larger, as a minor reduction in size should not have an adverse affect the quality of the image.

III. Math

If you are using *Word,* use either the Microsoft Equation Editor or the *MathType* add-on (http://www.mathtype.com) for equations in your paper (Insert | Object | Create New | Microsoft Equation *or* MathType Equation). "Float over text" should *not* be selected.

IV. Units

Use either SI (MKS) or CGS as primary units. (SI units are strongly encouraged.) English units may be used as secondary units (in parentheses). **This applies to papers in data storage.** For example, write "15 Gb/cm^2 (100 Gb/in^2)." An exception

TABLE I
Units for Magnetic Properties

Symbol	Quantity	Conversion from Gaussian and CGS EMU to SI [a]
Φ	magnetic flux	1 Mx $\rightarrow 10^{-8}$ Wb $= 10^{-8}$ V·s
B	magnetic flux density, magnetic induction	1 G $\rightarrow 10^{-4}$ T $= 10^{-4}$ Wb/m^2
H	magnetic field strength	1 Oe $\rightarrow 10^3/(4\pi)$ A/m
m	magnetic moment	1 erg/G = 1 emu $\rightarrow 10^{-3}$ A·m^2 $= 10^{-3}$ J/T
M	magnetization	1 erg/(G·cm^3) = 1 emu/cm^3 $\rightarrow 10^3$ A/m
$4\pi M$	magnetization	1 G $\rightarrow 10^3/(4\pi)$ A/m
σ	specific magnetization	1 erg/(G·g) = 1 emu/g $\rightarrow$ 1 A·m^2/kg
j	magnetic dipole moment	1 erg/G = 1 emu $\rightarrow 4\pi \times 10^{-10}$ Wb·m
J	magnetic polarization	1 erg/(G·cm^3) = 1 emu/cm^3 $\rightarrow 4\pi \times 10^{-4}$ T
χ, κ	susceptibility	$1 \rightarrow 4\pi$
χ_ρ	mass susceptibility	1 cm^3/g $\rightarrow 4\pi \times 10^{-3}$ m^3/kg
μ	permeability	$1 \rightarrow 4\pi \times 10^{-7}$ H/m $= 4\pi \times 10^{-7}$ Wb/(A·m)
μ_r	relative permeability	$\mu \rightarrow \mu_r$
w, W	energy density	1 erg/cm^3 $\rightarrow 10^{-1}$ J/m^3
N, D	demagnetizing factor	$1 \rightarrow 1/(4\pi)$

Vertical lines are optional in tables. Statements that serve as captions for the entire table do not need footnote letters.

[a]Gaussian units are the same as cgs emu for magnetostatics; Mx = maxwell, G = gauss, Oe = oersted; Wb = weber, V = volt, s = second, T = tesla, m = meter, A = ampere, J = joule, kg = kilogram, H = henry.

is when English units are used as identifiers in trade, such as "3½-in disk drive." Avoid combining SI and CGS units, such as current in amperes and magnetic field in oersteds. This often leads to confusion because equations do not balance dimensionally. If you must use mixed units, clearly state the units for each quantity in an equation.

The SI unit for magnetic field strength H is A/m. However, if you wish to use units of T, either refer to magnetic flux density B or magnetic field strength symbolized as $\mu_0 H$. Use the center dot to separate compound units, e.g., "A·m^2."

V. Helpful Hints

A. Figures and Tables

Because we will do the final formatting of your paper, you do not need to position figures and tables at the top and bottom of each column. In fact, all figures, figure captions, and tables can be at the end of the paper. Large figures and tables may span both columns. Place figure captions below the figures; place table titles above the tables. If your figure has two parts, include the labels "(a)" and "(b)" as part of the artwork. Please verify that the figures and tables you mention in the text actually exist. **Please do not include captions as part of the figures. Do not put captions in "text boxes" linked to the figures. Do not put borders around the outside of your figures.** Use the abbreviation "Fig." even at the beginning of a sentence. Do not abbreviate "Table." Tables are numbered with Roman numerals.

Color printing of figures is not available Do not use color unless it is necessary for the proper interpretation of your figures.

Figure axis labels are often a source of confusion. Use words rather than symbols. As an example, write the quantity "Magnetization," or "Magnetization *M*," not just "*M*." Put units in parentheses. Do not label axes only with units. As in Fig. 1, for example, write "Magnetization (A/m)" or "Magnetization ($A \cdot m^{-1}$)," not just "A/m." Do not label axes with a ratio of quantities and units. For example, write "Temperature (K)," not "Temperature/K."

Multipliers can be especially confusing. Write "Magnetization (kA/m)" or "Magnetization (10^3 A/m)." Do not write "Magnetization (A/m) x 1000" because the reader would not know whether the top axis label in Fig. 1 meant 16000 A/m or 0.016 A/m. Figure labels should be legible, approximately 8 to 12 point type.

B. References

Number citations consecutively in square brackets [1]. The sentence punctuation follows the brackets [2]. Multiple references [2], [3] are each numbered with separate brackets [1]–[3]. When citing a section in a book, please give the relevant page numbers [2]. In sentences, refer simply to the reference number, as in [3]. Do not use "Ref. [3]" or "reference [3]" except at the beginning of a sentence: "Reference [3] shows ... ." Please do not use automatic endnotes in *Word*, rather, type the reference list at the end of the paper using the "References" style.

Number footnotes separately in superscripts (Insert | Footnote).[1] Place the actual footnote at the bottom of the column in which it is cited; do not put footnotes in the reference list (endnotes). Use letters for table footnotes (see Table I).

Please note that the references at the end of this document are in the preferred referencing style. Give all authors' names; do not use "*et al*." unless there are six authors or more. Use a space after authors' initials. Papers that have not been published should be cited as "unpublished" [4]. Papers that have been accepted for publication, but not yet specified for an issue should be cited as "to be published" [5]. Papers that have been submitted for publication should be cited as "submitted for publication" [6]. Please give affiliations and addresses for private communications [7].

Capitalize only the first word in a paper title, except for proper nouns and element symbols. For papers published in translation journals, please give the English citation first, followed by the original foreign-language citation [8]. All references **must be** written in Roman alphabet.

C. Abbreviations and Acronyms

Define abbreviations and acronyms the first time they are used in the text, even after they have already been defined in the abstract. Abbreviations such as IEEE, SI, ac, and dc do not have to be defined. Abbreviations that incorporate periods should not have spaces: write "C.N.R.S.," not "C. N. R. S." Do not use abbreviations in the title unless they are unavoidable (for example, "IEEE" in the title of this article).

[1] It is recommended that footnotes be avoided (except for the unnumbered footnote with the receipt date and authors' affiliations on the first page). Instead, try to integrate the footnote information into the text.

D. Equations

Number equations consecutively with equation numbers in parentheses flush with the right margin, as in (1). First use the equation editor to create the equation. Then select the "Equation" markup style. Press the tab key and write the equation number in parentheses. To make your equations more compact, you may use the solidus (/), the exp function, or appropriate exponents. Use parentheses to avoid ambiguities in denominators. Punctuate equations when they are part of a sentence, as in

$$\int_0^{r_2} F(r,\varphi)\, dr\, d\varphi = [\sigma r_2 / (2\mu_0)] \cdot \int_0^{\infty} \exp(-\lambda |z_j - z_i|)\, \lambda^{-1} J_1(\lambda r_2)\, J_0(\lambda r_i)\, d\lambda . \quad (1)$$

Be sure that the symbols in your equation have been defined before the equation appears or immediately following. Italicize symbols (*T* might refer to temperature, but T is the unit tesla). Refer to "(1)," not "Eq. (1)" or "equation (1)," except at the beginning of a sentence: "Equation (1) is ... ."

E. Other Recommendations

Use one space after periods and colons. Hyphenate complex modifiers: "zero-field-cooled magnetization." Avoid dangling participles, such as, "Using (1), the potential was calculated." [It is not clear who or what used (1).] Write instead, "The potential was calculated by using (1)," or "Using (1), we calculated the potential."

Use a zero before decimal points: "0.25," not ".25." Use "cm^3," not "cc." Indicate sample dimensions as "0.1 cm x 0.2 cm," not "0.1 x 0.2 cm^2." The abbreviation for "seconds" is "s," not "sec." Do not mix complete spellings and abbreviations of units: use "Wb/m^2" or "webers per square meter," not "webers/m^2." When expressing a range of values, write "7 to 9" or "7-9," not "7~9."

A parenthetical statement at the end of a sentence is punctuated outside of the closing parenthesis (like this). (A parenthetical sentence is punctuated within the parentheses.) In American English, periods and commas are within quotation marks, like "this period." Other punctuation is "outside"! Avoid contractions; for example, write "do not" instead of "don't." The serial comma is preferred: "A, B, and C" instead of "A, B and C."

If you wish, you may write in the first person singular or plural and use the active voice ("I observed that ..." or "We observed that ..." instead of "It was observed that ..."). Remember to check spelling. If your native language is not English, please get a native English-speaking colleague to carefully proofread your paper.

VI. Some Common Mistakes

The word "data" is plural, not singular. The subscript for the permeability of vacuum μ_0 is zero, not a lowercase letter "o." The term for residual magnetization is "remanence"; the adjective is "remanent"; do not write "remnance" or "remnant." Use the word "micrometer" instead of "micron." A graph within a graph is an "inset," not an "insert." The word "alternatively" is preferred to the word "alternately" (unless you really mean something that alternates). Use the word "whereas" instead of "while" (unless you are referring to simultaneous events). Do not use the word "essentially" to mean "approximately" or "effectively." Do not use the word "issue" as a euphemism for "problem." When compositions are not specified, separate chemical symbols by en-dashes; for example, "NiMn" indicates the intermetallic compound $Ni_{0.5}Mn_{0.5}$ whereas "Ni–Mn" indicates an alloy of some composition Ni_xMn_{1-x}.

Be aware of the different meanings of the homophones "affect" (usually a verb) and "effect" (usually a noun), "complement" and "compliment," "discreet" and "discrete," "principal" (e.g., "principal investigator") and "principle" (e.g., "principle of measurement"). Do not confuse "imply" and "infer."

Prefixes such as "non," "sub," "micro," "multi," and "ultra" are not independent words; they should be joined to the words they modify, usually without a hyphen. There is no period after the "et" in the Latin abbreviation "*et al.*" (it is also italicized). The abbreviation "i.e.," means "that is," and the abbreviation "e.g.," means "for example" (these abbreviations are not italicized).

An excellent style manual and source of information for science writers is [9].

VII. Editorial Policy

Each manuscript submitted is subjected to the following review procedure:

- It is reviewed by the editor for general suitability for this publication
- If it is judged suitable, two reviewers are selected and a single-blinded review process takes place
- Based on the recommendations of the reviewers, the editor then decides whether the particular paper should be accepted as is, revised or rejected.

Do not submit a paper you have submitted or published elsewhere. Do not publish "preliminary" data or results. The submitting author is responsible for obtaining agreement of all coauthors and any consent required from sponsors before submitting a paper. It is the obligation of the authors to cite relevant prior work.

Every paper submitted to "Electronics" journal are single-blind reviewed. For conference-related papers, the decision to accept or reject a paper is made by the conference editors and publications committee; the recommendations of the referees are advisory only. Undecipherable English is a valid reason for rejection.

VIII. Publication Principles

The contents of "Electronics" are peer-reviewed and archival. The "Electronics" publishes scholarly articles of archival value as well as tutorial expositions and critical reviews of classical subjects and topics of current interest.

Authors should consider the following points:

1) Technical papers submitted for publication must advance the state of knowledge and must cite relevant prior work.
2) The length of a submitted paper should be commensurate with the importance, or appropriate to the complexity, of the work. For example, an obvious extension of previously published work might not be appropriate for publication or might be adequately treated in just a few pages.
3) Authors must convince both peer reviewers and the editors of the scientific and technical merit of a paper; the standards of proof are higher when extraordinary or unexpected results are reported.
4) Because replication is required for scientific progress, papers submitted for publication must provide sufficient information to allow readers to perform similar experiments or calculations and use the reported results. Although not everything need be disclosed, a paper must contain new, useable, and fully described information. For example, a specimen's chemical composition need not be reported if the main purpose of a paper is to introduce a new measurement technique. Authors should expect to be challenged by reviewers if the results are not supported by adequate data and critical details.
5) Papers that describe ongoing work or announce the latest technical achievement, which are suitable for presentation at a professional conference, may not be appropriate for publication in "Electronics".

IX. Conclusion

A conclusion section is not required. Although a conclusion may review the main points of the paper, do not replicate the abstract as the conclusion. A conclusion might elaborate on the importance of the work or suggest applications and extensions.

Appendix

Appendixes, if needed, appear before the acknowledgment.

Acknowledgment

The preferred spelling of the word "acknowledgment" in American English is without an "e" after the "g." Use the singular heading even if you have many acknowledgments. Avoid expressions such as "One of us (S.B.A.) would like to thank ... ." Instead, write "F. A. Author thanks ... ." **Sponsor and financial support acknowledgments are placed in the unnumbered footnote on the first page, not here.**

References

[1] G. O. Young, "Synthetic structure of industrial plastics (Book style with paper title and editor)," in *Plastics*, 2nd ed. vol. 3, J. Peters, Ed. New York: McGraw-Hill, 1964, pp. 15–64.

[2] W.-K. Chen, *Linear Networks and Systems* (Book style). Belmont, CA: Wadsworth, 1993, pp. 123–135.

[3] H. Poor, *An Introduction to Signal Detection and Estimation*. New York: Springer-Verlag, 1985, ch. 4.

[4] B. Smith, "An approach to graphs of linear forms (Unpublished work style)," unpublished.

[5] E. H. Miller, "A note on reflector arrays (Periodical style—Accepted for publication)," *IEEE Trans. Antennas Propagat.*, to be published.

[6] J. Wang, "Fundamentals of erbium-doped fiber amplifiers arrays (Periodical style—Submitted for publication)," *IEEE J. Quantum Electron.*, submitted for publication.

[7] C. J. Kaufman, Rocky Mountain Research Lab., Boulder, CO, private communication, May 1995.

[8] Y. Yorozu, M. Hirano, K. Oka, and Y. Tagawa, "Electron spectroscopy studies on magneto-optical media and plastic substrate interfaces (Translation Journals style)," *IEEE Transl. J. Magn.Jpn.*, vol. 2, Aug. 1987, pp. 740–741 [*Dig. 9th Annu. Conf. Magnetics* Japan, 1982, p. 301].

[9] M. Young, *The Techincal Writers Handbook.* Mill Valley, CA: University Science, 1989.

[10] J. U. Duncombe, "Infrared navigation—Part I: An assessment of feasibility (Periodical style)," *IEEE Trans. Electron Devices*, vol. ED-11, pp. 34–39, Jan. 1959.

[11] S. Chen, B. Mulgrew, and P. M. Grant, "A clustering technique for digital communications channel equalization using radial basis function networks," *IEEE Trans. Neural Networks*, vol. 4, pp. 570–578, Jul. 1993.

[12] R. W. Lucky, "Automatic equalization for digital communication," *Bell Syst. Tech. J.*, vol. 44, no. 4, pp. 547–588, Apr. 1965.

[13] S. P. Bingulac, "On the compatibility of adaptive controllers (Published Conference Proceedings style)," in *Proc. 4th Annu. Allerton Conf. Circuits and Systems Theory*, New York, 1994, pp. 8–16.

[14] G. R. Faulhaber, "Design of service systems with priority reservation," in *Conf. Rec. 1995 IEEE Int. Conf. Communications,* pp. 3–8.

[15] W. D. Doyle, "Magnetization reversal in films with biaxial anisotropy," in *1987 Proc. INTERMAG Conf.*, pp. 2.2-1–2.2-6.

[16] G. W. Juette and L. E. Zeffanella, "Radio noise currents n short sections on bundle conductors (Presented Conference Paper style)," presented at the IEEE Summer power Meeting, Dallas, TX, Jun. 22–27, 1990, Paper 90 SM 690-0 PWRS.

[17] J. G. Kreifeldt, "An analysis of surface-detected EMG as an amplitude-modulated noise," presented at the 1989 Int. Conf. Medicine and Biological Engineering, Chicago, IL.

[18] J. Williams, "Narrow-band analyzer (Thesis or Dissertation style)," Ph.D. dissertation, Dept. Elect. Eng., Harvard Univ., Cambridge, MA, 1993.

[19] N. Kawasaki, "Parametric study of thermal and chemical nonequilibrium nozzle flow," M.S. thesis, Dept. Electron. Eng., Osaka Univ., Osaka, Japan, 1993.

[20] J. P. Wilkinson, "Nonlinear resonant circuit devices (Patent style)," U.S. Patent 3 624 12, July 16, 1990.

[21] IEEE Criteria for Class IE Electric Systems (Standards style)*,* IEEE Standard 308, 1969.

[22] Letter Symbols for Quantities, ANSI Standard Y10.5-1968.

[23] R. E. Haskell and C. T. Case, "Transient signal propagation in lossless isotropic plasmas (Report style)," USAF Cambridge Res. Lab., Cambridge, MA Rep. ARCRL-66-234 (II), 1994, vol. 2.

[24] E. E. Reber, R. L. Michell, and C. J. Carter, "Oxygen absorption in the Earth's atmosphere," Aerospace Corp., Los Angeles, CA, Tech. Rep. TR-0200 (420-46)-3, Nov. 1988.

[25] (Handbook style) *Transmission Systems for Communications,* 3rd ed., Western Electric Co., Winston-Salem, NC, 1985, pp. 44–60.

[26] *Motorola Semiconductor Data Manual,* Motorola Semiconductor Products Inc., Phoenix, AZ, 1989.

[27] (Basic Book/Monograph Online Sources) J. K. Author. (year, month, day). *Title* (edition) [Type of medium]. Volume (issue). Available: http://www.(URL)

[28] J. Jones. (1991, May 10). Networks (2nd ed.) [Online]. Available: http://www.atm.com

[29] (Journal Online Sources style) K. Author. (year, month). Title. *Journal* [Type of medium]. Volume(issue), paging if given. Available: http://www.(URL)

[30] R. J. Vidmar. (1992, August). On the use of atmospheric plasmas as electromagnetic reflectors. *IEEE Trans. Plasma Sci.* [Online]. *21(3).* pp. 876–880. Available: http://www.halcyon.com/pub/journals/21ps03-vidmar

Information for Authors

Editorial objectives

In the journal ”Electronics”, the scientific papers from different fields of electronics and electrical engineering in the broadest sense are published. Main topics are electronics, automatics, telecommunications, computer techniques, power engineering, nuclear and medical electronics, analysis and synthesis of electronic circuits and systems, new technologies and materials in electronics etc. The main emphasis of papers should be on methods and new techniques, or the application of existing techniques in a novel way.

The reviewing process

Each manuscript submitted is subjected to the following review procedures:

- It is reviewed by the editor for general suitability for this publication;
- If it is judged suitable, two reviewers are selected and a double-blind review process takes place;
- Based on the recommendations of the reviewers, the editor then decides whether the particular paper should be accepted as it is, revised or rejected.

Submissions Process

The manuscripts are to be submitted using the Electronics Journal online submission system – accessible from Journal’s homepage.

Manuscripts have to be prepared in accordance with the instructions given in the template for paper preparation that can be found on the journal’s web page (www.els-journal.etf.unibl.org).

Authors should note that proofs are not supplied prior to publication and ensure that the paper submitted is complete and in its final form.

Copyright

Articles submitted to the journal should be original contributions and should not be under consideration for any other publication at the same time. Authors submitting articles for publication warrant that the work is not an infringement of any existing copyright and will indemnify the publisher against any breach of such warranty. For ease of dissemination and to ensure proper policing of use, papers and contributions become the legal copyright of the publisher unless otherwise agreed.